

**Doctoral Dissertation**  
submitted to the  
Combined Faculties for the Natural Sciences and for Mathematics  
of the Ruperto - Carola University of Heidelberg, Germany  
for the degree of  
Doctor of Natural Sciences

Dipl-Physics:  
Born in:

Put forward by

Francesco Borgosano  
Messina, Italy

Oral examination: October 31, 2012



Studies of the influence of  
thermodynamical parameters on the  
production rate of hyperpolarised  $^{129}\text{Xe}$   
and the degree of hyperpolarisation

Referees:

Prof. Dr. Peter Bachert  
Prof. Dr. Dirk Dubbers



Untersuchung des Einflusses thermodynamischer Parameter auf die Produktions rate von hyperpolarisiertem  $^{129}\text{Xe}$  und den Grad der Hyperpolarisation

Hyperpolarisiertes Xenon ( $^{129}\text{Xe}$ ) findet Anwendung in vielen Bereichen der MR - Bildgebung (MRI) und NMR - Spektroskopie.  $^{129}\text{Xe}$ , ein Edelgas mit Spin 1/2 kann auf hohe Kernspin - Polarisation gebracht werden, welche durch optisches Spin - Austausch - Pumpen (SEOP) mit Rubidium erreicht wird. Unter Verwendung eines Polarisators für kontinuierlichen Gasfluss wurde untersucht, wie makroskopische Parameter wie die Rb - Temperatur (60 - 200° C), der Druck des Puffergases (2 - 7 atm) und die Flussrate der Gasmischung (6 - 30 l/h) den gemessenen Grad der Hyperpolarisation von  $^{129}\text{Xe}$  beeinflussen. Die Messungen wurden mithilfe eines 1.5 - T - Ganzkörper - MR - Tomographen durchgeführt. Die erzielten Ergebnisse stimmen mit theoretischen Vorhersagen überein und zeigen einen exponentiellen Abfall der Polarisation mit steigender Rb - Temperatur. Weiterhin wurde eine Abhängigkeit der Polarisation von der Flussrate der Gasmischung beobachtet. Außerdem konnte die direkte Beziehung zwischen der absorbierten Laserleistung der Rb - Atome und der Xe - Hyperpolarisation, der Laser - Heating - Effekt, und die Abhängigkeit der chemischen Verschiebung von der Temperatur gemessen werden. Dieses Wissen ist Grundvoraussetzung für die Optimierung des Systems, um Messungen zur Diffusion von  $^{129}\text{Xe}$  - Gas und zur chemischen Verschiebung der Resonanzfrequenz von  $^{129}\text{Xe}$  in vivo zu ermöglichen.

Studies of the influence of thermodynamical parameters on the production rate of hyperpolarised  $^{129}\text{Xe}$  and the degree of hyperpolarisation

Hyperpolarised Xenon ( $^{129}\text{Xe}$ ) has found a steadily increasing range of applications in MR imaging (MRI) and NMR spectroscopy.  $^{129}\text{Xe}$ , a noble gas with spin 1/2 has the advantage of a large nuclear spin polarisation obtained by spin exchange optical pumping (SEOP) with rubidium (Rb). Using a continuous flow polariser, we studied how macroscopic parameters like the Rb temperature (60 - 200° C), buffer gas pressure (2 - 7 atm), and gas mixture flow rate (6 - 30 l/h), affect the measured degree of hyperpolarisation of  $^{129}\text{Xe}$  gas. Measurements have been performed using a 1.5 - T whole - body MR tomograph. Our results are in agreement with theoretical predictions and show that upon increasing the Rb temperature the degree of polarisation decreases exponentially. We observed an almost linear dependence of the degree of polarisation on the gas mixture flow rate. Furthermore, the direct relation between the absorbed laser - power by the Rb atoms and the hyperpolarisation, the laser - heating effect, and the dependence of the  $^{129}\text{Xe}$  chemical shift on temperature could be measured. This knowledge is a prerequisite for system optimisation aimed at performing measurements on  $^{129}\text{Xe}$  gas diffusion and the chemical shift of  $^{129}\text{Xe}$  resonances in vivo.



*This thesis is dedicated to...*

*...my parents who have given me the opportunity of an education from the best institutions and support throughout my life.*

*...my wife without whom I would be nothing. She always comforts and consoles, never complains or interferes, and endures all.*



# Contents

|  |           |
|--|-----------|
| Contents   | v         |
| Nomenclature   | viii      |
| List of Figures  | ix        |
| <b>1 Introduction</b>  | <b>1</b>  |
| <b>2 Theoretical background</b>                                | <b>5</b>  |
| 2.1 Nuclear Magnetic Resonance . . . . .                       | 5         |
| 2.1.1 The nuclear spin . . . . .                               | 5         |
| 2.1.2 Macroscopic magnetisation . . . . .                      | 11        |
| 2.1.3 Bloch equations . . . . .                                | 13        |
| 2.1.4 NMR Signal . . . . .                                     | 17        |
| 2.1.5 Chemical shift . . . . .                                 | 19        |
| 2.1.6 $T_1$ Relaxation . . . . .                               | 21        |
| 2.1.7 $T_2$ Relaxation and spin-echoes . . . . .               | 23        |
| 2.2 Physical properties of Xenon (Xe) . . . . .                | 25        |
| 2.2.1 $^{129}\text{Xe}$ chemical shift . . . . .               | 27        |
| 2.3 Physical properties of Rubidium (Rb) . . . . .             | 28        |
| 2.4 Optical pumping of noble gas nuclei . . . . .              | 29        |
| 2.4.1 Spin exchange optical pumping . . . . .                  | 31        |
| 2.4.2 Evolution of Rb - atom ground state . . . . .            | 32        |
| 2.4.3 Electronic spin polarisation of Rb . . . . .             | 35        |
| 2.4.4 Nuclear spin polarisation of $^{129}\text{Xe}$ . . . . . | 36        |
| <b>3 Materials and methods</b>                                 | <b>41</b> |
| 3.1 Hyperpolarisation equipment . . . . .                      | 42        |
| 3.1.1 Gas supply system . . . . .                              | 42        |
| 3.1.2 Laser system . . . . .                                   | 42        |
| 3.1.3 Rb - Xe polariser . . . . .                              | 44        |

## CONTENTS

---

|          |   |            |
|----------|---|------------|
| 3.2      | MR equipment . . . . .  | 47         |
| 3.3      | Maintenance and setup of the OPC . . . . .                      | 48         |
| 3.3.1    | Filling procedure . . . . .                                     | 48         |
| 3.3.2    | Cleaning and refilling procedures . . . . .                     | 48         |
| 3.3.3    | Setup procedure . . . . .                                       | 49         |
| 3.4      | Data analysis . . . . .   | 49         |
| 3.4.1    | Evaluation of $^{129}\text{Xe}$ hyperpolarisation . . . . .     | 50         |
| <b>4</b> | <b>Results</b>  | <b>53</b>  |
| 4.1      | Polarisation of the pumping laser beam . . . . .                | 53         |
| 4.2      | Laser absorption by Rb vapor . . . . .                          | 54         |
| 4.2.1    | Temperature dependence . . . . .                                | 56         |
| 4.2.2    | Pressure broadening of the $D_1$ - absorption line . . . . .    | 57         |
| 4.3      | Thermal polarisation of $^{129}\text{Xe}$ . . . . .             | 59         |
| 4.4      | Hyperpolarisation of $^{129}\text{Xe}$ . . . . .                | 59         |
| 4.4.1    | Influence of Rb temperature . . . . .                           | 60         |
| 4.4.2    | Influence of pressure . . . . .                                 | 62         |
| 4.4.3    | Influence of gas flow . . . . .                                 | 62         |
| 4.4.4    | Maximum enhancement of $^{129}\text{Xe}$ polarisation . . . . . | 62         |
| 4.5      | Laser - Heating effect . . . . .                                | 64         |
| 4.6      | Relaxation in PU tubes . . . . .                                | 66         |
| 4.7      | Dependence of xenon gas chemical shift on temperature . . . . . | 66         |
| <b>5</b> | <b>Discussion</b>   | <b>69</b>  |
| <b>6</b> | <b>Newly developed HPD</b>                                      | <b>75</b>  |
| 6.1      | New HPD concepts . . . . .                                      | 75         |
| 6.2      | New OPC design . . . . .  | 78         |
| 6.3      | Accumulation of hyperpolarised $^{129}\text{Xe}$ . . . . .      | 80         |
| 6.3.1    | Frozen xenon relaxation mechanism . . . . .                     | 81         |
| 6.3.2    | Xenon accumulation . . . . .                                    | 81         |
| 6.4      | NMR of dissolved $^{129}\text{Xe}$ . . . . .                    | 83         |
| <b>7</b> | <b>Conclusions</b>  | <b>87</b>  |
| <b>A</b> | <b>Matlab programs</b>  | <b>89</b>  |
| A.1      | Reading and evaluating raw data . . . . .                       | 89         |
| A.1.1    | Main program . . . . .  | 89         |
| A.1.2    | Functions . . . . .   | 93         |
| A.2      | IR - spectrometer data . . . . .                                | 100        |
|          | <b>Bibliography</b>   | <b>103</b> |

# Nomenclature

$\vec{B}_0$  External static magnetic field

$\vec{B}_1$  External RF magnetic field

a.u. Atomic units

CCD Charge coupled device

DICOM Digital imaging and communications in medicine

EMF Electromagnetic field

FID Free induction decay

FOV Field of view

FWHM Full width at half maximum

HPD Hyperpolarisation device

LDA Laser Diode Array

LHE Laser heating effect

OPC Optical pumping cell

PID Proportional integral derivative

ppm Parts per million

PU Polyurethane

PVDF Polyvinylidene fluoride

RF Radio frequency

TE Echo time

## **CONTENTS**

---

TR Repetition time

MRI Magnetic Resonance Imaging

NMR Nuclear Magnetic Resonance

SEOP Spin Exchange Optical Pumping

SNR Signal - to - Noise Ratio

# List of Figures

|      |  |    |
|------|--|----|
| 2.1  | Magnetic energy levels . . . . .   | 10 |
| 2.2  | Spin precession . . . . .  | 11 |
| 2.3  | Total magnetisation precession . . . . .   | 14 |
| 2.4  | Linear oscillating magnetic field decomposition . . . . .  | 15 |
| 2.5  | Magnetic field vectors in the rotating frame . . . . .   | 17 |
| 2.6  | Transverse relaxation process . . . . .  | 18 |
| 2.7  | Chemical shift . . . . .   | 20 |
| 2.8  | $T_1$ relaxation . . . . .   | 22 |
| 2.9  | Ernst angle versus $TR/T_1$ . . . . .  | 23 |
| 2.10 | Measurement of $T_1$ relaxation - inversion recovery method . . . . .                              | 24 |
| 2.11 | Hahn sequence . . . . .  | 24 |
| 2.12 | Measurement of $T_2$ relaxation through the use of the spin - echo method. . . . .                 | 25 |
| 2.13 | Phase diagram of Xenon . . . . .   | 26 |
| 2.14 | $^{129}\text{Xe}$ chemical shift range . . . . .   | 27 |
| 2.15 | Temperature dependence of Rb number density . . . . .  | 29 |
| 2.16 | Energy level schemes of two Rb isotopes . . . . .  | 30 |
| 2.17 | Spin exchange optical pumping scheme . . . . .   | 31 |
| 2.18 | Elements involved in the optical pumping experiment . . . . .                                      | 33 |
| 2.19 | Dependence of mean $^{129}\text{Xe}$ polarisation as a function of temperature. . . . .            | 38 |
| 2.20 | Dependence of mean $^{129}\text{Xe}$ polarisation as a function of xenon partial pressure. . . . . | 38 |
| 3.1  | Schematic drawing of the Xe - polariser . . . . .  | 41 |
| 3.2  | View of the optical unit. . . . .  | 43 |
| 3.3  | Front view of Rb - Xe polariser. . . . .   | 45 |
| 3.4  | Optical Pumping cell. . . . .  | 46 |
| 4.1  | Experimental setup for measuring circular polarisation . . . . .                                   | 53 |
| 4.2  | Results of pumping laser circular polarisation measurements . . . . .                              | 55 |
| 4.3  | Laser absorption reference spectrum . . . . .  | 55 |

## LIST OF FIGURES

---

|      |   |    |
|------|---|----|
| 4.4  | Temperature dependence of laser absorption by Rb . . . . .  | 56 |
| 4.5  | Pressure dependence of laser absorption by Rb . . . . .   | 57 |
| 4.6  | Pressure dependence of laser absorption detail . . . . .  | 58 |
| 4.7  | Rb D <sub>1</sub> absorption line broadening versus pressure. . . . .                                   | 58 |
| 4.8  | Hyperpolarisation of <sup>129</sup> Xe as a function of temperature, pressure<br>and gas flow . . . . . | 60 |
| 4.9  | Dependence on temperature of hyperpolarised <sup>129</sup> Xe production . . . . .                      | 61 |
| 4.10 | Dependence on pressure of hyperpolarised <sup>129</sup> Xe production . . . . .                         | 63 |
| 4.11 | Dependence on flow rate of hyperpolarised <sup>129</sup> Xe production . . . . .                        | 64 |
| 4.12 | Laser heating effect . . . . .  | 65 |
| 4.13 | Optical pumping time dependence of laser absorption by Rb vapor . . . . .                               | 66 |
| 4.14 | Signal versus PU connection tube length. . . . .  | 67 |
| 4.15 | Temperature dependence of xenon gas chemical shift . . . . .  | 68 |
| 5.1  | External cavities used in LDA bandwidth narrowing . . . . .   | 70 |
| 6.1  | Theoretical laser absorption cross section for different buffer gas<br>pressure . . . . .               | 76 |
| 6.2  | New HPD concepts . . . . .  | 79 |
| 6.3  | New OPC design. . . . .   | 80 |
| 6.4  | <sup>129</sup> Xe spin relaxation . . . . .   | 82 |
| 6.5  | Cold trap design . . . . .  | 82 |
| 6.6  | Membrane pump setup . . . . .   | 85 |

# Chapter 1

## Introduction

Nuclear magnetic resonance (NMR) is a physical phenomenon related to the intrinsic quantum property, the spin, of certain atomic nuclei. Since its discovery, applications of NMR have widened from physics and chemistry, to biology and medicine, to technology and industry. The importance of the discovery was recognized by the large number of Noble prizes awarded for the development of NMR techniques. Moreover, it is remarkable that NMR techniques have become successful established methods for the nondestructive investigation of matter and living tissues.

Otto Stern was awarded in 1935 the Nobel prize in physics "for his contribution to the development of the molecular ray method and his discovery of the magnetic moment of the proton". Indeed in 1922 Otto Stern with Walter Gerlach performed an experiment [Gerlach and Stern, 1922] on the deflection of particles that can be used to demonstrate that electrons and atoms have intrinsically magnetic properties. In the following years, Isidor Rabi developed a new method for recording magnetic resonance of atomic nuclei [Rabi et al., 1938]; he was awarded the Nobel prize in physics in 1944. The first successful demonstrations of NMR in bulk matter were published in 1946, by two independent groups: Bloch, Hansen and Packard [Bloch et al., 1946] working at Stanford University and Purcell, Torrey and Pound working at Harvard University [Purcell et al., 1946]. The two leaders, Felix Bloch and Edward Purcell were jointly awarded the 1952 Nobel prize for physics. Five years after these experiments it had been noted by several workers that the NMR frequency of a given nucleus depends on the chemical environment [Arnold and Packard, 1951; Dickinson, 1950; Knight, 1949; Proctor and Yu, 1950]. Richard Ernst in 1966 exploited pulsed Fourier transform NMR [Ernst and Anderson, 1966]. He received the Nobel prize in chemistry in 1991, "for his contributions to the development of the methodology of high resolution NMR spectroscopy". Recently, Kurt Wüthrich was awarded Nobel prize in chemistry "for his development of nuclear magnetic resonance spectroscopy for determining

## 1. INTRODUCTION

---

the three - dimensional structure of biological macromolecules in solution". Beginning in the 1970s, NMR also found applications in medicine. In particular, a well - known application of NMR is magnetic resonance imaging (MRI), which is a non - invasive tool to visualize internal structures of the human body. For their discoveries concerning MRI, Paul C. Lauterbur [[Lauterbur, 1973](#)] and Peter Mansfield [[Mansfield and Grannell, 1973](#)] were jointly awarded 2003 Nobel prize in medicine or physiology.

The principle behind NMR is that all nuclei with non - zero spin, have non - zero magnetic moment related to spin via the gyromagnetic ratio. Magnetic nuclei in an external magnetic field absorb and re - emit electromagnetic energy, this transferred energy is at a specific resonance frequency which depends on the strength of the external magnetic field and the magnetic moment of the nuclei (Zeeman effect). The signal that matches this transfer is measured and processed in order to yield an NMR signal for the nucleus concerned. However, the main drawback of NMR is the limited sensitivity, indeed it is rather poor compared with other techniques. This is a result of the small population difference between the nuclear Zeeman energy levels even in the highest magnetic fields currently available in the laboratory. Therefore, since the discovery of NMR, methods to improve the signal to noise ratio (SNR) have been the subject of active research.

In the last decades, optical pumping methods able to increase the NMR sensitivity of noble gas nuclei by several orders of magnitude have been particularly successful. Since the nuclear spin polarisation created through these methods is far from the equilibrium Boltzmann polarisation, these gases are referred to as "hyperpolarised" gases. Due to the large nuclear spin polarisation, created via optical pumping methods, noble gas nuclei found a growing numbers of applications as MR contrast agent. The hyperpolarised gases mainly used for NMR applications are  $^{129}\text{Xe}$  and  $^3\text{He}$ , both are spin - 1/2 nuclei. Throughout this dissertation I will focus on  $^{129}\text{Xe}$ , because it is the noble gas used in our experimental work.

In recent years, hyperpolarised  $^{129}\text{Xe}$  has been used in a wide range of different fields. In biological sciences it can be used to measure the xenon exchange process between red blood cells and the blood plasma [[Bifone et al., 1996](#)] as well as the degree of oxygenation in human blood [[Albert et al., 2000](#); [Wolber et al., 2000](#)]. Hyperpolarised  $^{129}\text{Xe}$  has been applied to study of protein solution [[Bowers et al., 1999](#); [Landon et al., 2001](#)] and utilised for functionalised xenon biosensors [[Lowery et al., 2006](#); [Schroeder, 2011](#); [Schroeder et al., 2006](#)]. In medical sciences, hyperpolarised  $^{129}\text{Xe}$  have found applications in anatomical and functional MRI of the lung [[Dregely et al., 2011](#); [Kaushik et al., 2011](#)] and the brain [[Swanson et al., 1997](#); [Zhou et al., 2011](#)]. Moreover  $^{129}\text{Xe}$  has been used for spectroscopic images of living organs [[Duhamel et al., 2001](#); [Wakai et al., 2004](#)].

The method which has become standard to produce hyperpolarised gases,

---

the same used in this work, is called spin exchange optical pumping (SEOP) [Driehuys et al., 1996; Happer, 1972]. The mechanism of creating high nuclear spin polarisations can be described as a chain of transfer processes, it makes use of optical pumping of alkali metals (rubidium in our system) by circularly polarised light (tuned on Rb D<sub>1</sub> absorption line), followed by polarisation transfer (spin exchange) to the nuclear spin system of noble gas nuclei during collisions. The current standard degree of polarisation achievable for <sup>129</sup>Xe polarisers, based on SEOP with Rb, is ≈20% with a volume production close to 1 l/h. For small volume productions, a much higher degree of polarisation ≈70% has been reported [Ruth et al., 1999]. In 2002, a new polariser using high power laser for optical pumping [Zook et al., 2002], showed high capacity production of xenon with polarisation degree ≈65%.

While most of the quantum - mechanical processes involved in SEOP have already been understood quite well, the production of hyperpolarised gases depends on many other macroscopic quantities such as laser power, temperature, buffer gas pressure, and the flow rate in the pumping cell. The thermodynamical processes taking place in a pumping cell during the SEOP have not yet been understood in detail. In this work, I describe a series of experimental measurements, we performed, aimed to understand how the macroscopic thermodynamical parameters can affect the measured hyperpolarisation degree of <sup>129</sup>Xe - gas. This knowledge is a prerequisite for system optimisation aimed to perform measurements on <sup>129</sup>Xe gas diffusion (pore diffusion imaging) and the chemical shift of <sup>129</sup>Xe resonances in vivo.

In the following the outline of the remaining chapters in this dissertation is summarised. Chapter 2 is an introduction to the basic theory of NMR and MRI. It also deals with the physical properties of rubidium and <sup>129</sup>Xe, required to understand the SEOP process. The theory of spin exchange optical pumping is then discussed in detail. Chapter 3 provides a description of the design and materials which make up our <sup>129</sup>Xe polariser and an overview of the methods for data analysis and evaluation of results. In chapter 4 the experimental results of this work are presented, which are further discussed in chapter 5. In chapter 6, novel ideas concerning new developments of our hyperpolarisation system are described. The last section, chapter 7, is a brief summary of key findings and gives an outlook of our research in the field of <sup>129</sup>Xe hyperpolarisation.



# Chapter 2

## Theoretical background

This chapter outlines the basic theory of NMR, followed by a description of the physical properties of xenon gas and rubidium, necessary for understanding of the spin exchange optical pumping theory introduced in the last section of the chapter.

### 2.1 Nuclear Magnetic Resonance

In the following section the basic principles of NMR are described. NMR is the study of the magnetic properties (and energies) of nuclei. The physics of NMR is based on an intrinsic property of atomic nuclei, the nuclear spin. Strictly speaking, the nuclear spin is a purely quantum - mechanical quantity. However, classical physics can be used to create a familiar frame of reference in which the existence of a spin angular momentum can be visualized. Nevertheless, quantum mechanics is the only theory which can quantitatively describe the NMR phenomenon. But, for spin - 1/2, the vector of the magnetisation density in 3D Euklidean space ( $\mathbb{R}^3$ ) is an appropriate concept to describe the dynamics of a huge ensemble of nuclear spins. A detailed quantum - mechanical description of NMR can be found in textbooks like [[Abragam, 1961](#)] and [[Levitt, 2008](#)].

#### 2.1.1 The nuclear spin

The concept of nuclear spin was forced upon to scientists by the experimental evidence from Otto Stern and Walter Gerlach in 1922 [[Gerlach and Stern, 1922](#)]. The Stern - Gerlach experiment involves sending a beam of silver atoms, which, in the ground state, possess a total angular momentum of 1/2, through an inhomogeneous magnetic field and observing their deflection. The splitting of the beam of atoms is a direct consequence and a striking experimental proof that

## 2. THEORETICAL BACKGROUND

---

atomic particles possess an intrinsic angular momentum.

As the name suggests, spin was originally conceived as the rotation of a particle around some axis. This picture is correct so far as spins obey the same mathematical laws as the expectation value of quantized angular momenta do. However, spin is not produced by a rotation of the particle, but is an intrinsic property. Therefore, spin is a form of angular momentum, which has no analogue in classical mechanics, that can be explained by the quantum theory of angular momentum.

### Classical description

Motion (linear or rotational) always has a corresponding momentum (linear or angular) and it only changes when external forces are applied.

Now consider an object rotating with constant velocity  $\vec{v}$  about a fixed point at a distance  $\vec{r}$ ; this motion is described with an angular momentum  $\vec{L}$ :

$$\vec{L} = \vec{r} \times \vec{p} \quad (2.1)$$

where  $\vec{p} = m\vec{v}$  is the linear momentum. As above cited, angular momentum can only be changed when an external force is applied. In particular, defining a rotational force  $\vec{T}$  as the cross product of force and the distance over which the force has to be delivered, we can write:

$$\vec{T} = \vec{r} \times \vec{F} = \vec{r} \times \left( \frac{d\vec{p}}{dt} \right) = \left( \frac{d\vec{L}}{dt} \right) \quad (2.2)$$

Now suppose that the rotating object carries an electrical charge, so that a current loop is created. According to classical physics this current generates a magnetic field, which is characterised by the magnetic dipole moment  $\vec{\mu}$ . In general, the magnitude of the magnetic moment  $|\vec{\mu}|$  is given by:

$$|\vec{\mu}| = [\textit{current}] \times [\textit{area}] \quad (2.3)$$

For an object of mass  $m$ , charge  $e$ , rotating on a circle at constant rotational velocity  $\vec{v}$  about a fixed point at distance  $\vec{r}$  the magnetic dipole moment is:

$$\vec{\mu} = \left( \frac{e}{2} \right) \vec{r} \times \vec{v} \quad (2.4)$$

Using  $\vec{L} = -m\vec{v} \times \vec{r}$ , a fundamental relation between magnetic moment and angular moment is obtained:

$$\vec{\mu} = \left( \frac{e}{2m} \right) \cdot \vec{L} = \gamma \vec{L} \quad (2.5)$$

## 2.1. Nuclear Magnetic Resonance

---

where  $\gamma$  is the classical gyromagnetic ratio. This relation is valid for any periodic orbital moment, including microscopic motion of elementary particles. When the rotating object is placed in an external magnetic field  $\vec{B}_0$ , the loop will feel a torque given by:

$$\vec{T} = \vec{\mu} \times \vec{B}_0 \quad (2.6)$$

Combining Equation (2.2), (2.5) and (2.6) gives:

$$\frac{d\vec{\mu}}{dt} = \gamma \vec{\mu} \times \vec{B}_0 \quad (2.7)$$

Since the amplitude of  $\vec{\mu}$  is constant, the differential Equation (2.7) expresses the fact that  $\vec{\mu}$  changes its orientation relative to  $\vec{B}_0$ , i.e.  $\vec{\mu}$  rotates about  $\vec{B}_0$ . Alternatively, a precession of  $\vec{\mu}$  about  $\vec{B}_0$  can be described by:

$$\frac{d\vec{\mu}}{dt} = \vec{\mu} \times \vec{\omega}_0 \quad (2.8)$$

Combining Equation (2.7) and (2.8) results in the famous Larmor Equation:

$$\begin{aligned} \vec{\omega}_0 &= \gamma \vec{B}_0 \\ \vec{\nu}_0 &= \frac{\vec{\omega}_0}{2\pi} = \left( \frac{\gamma}{2\pi} \right) \vec{B}_0 \end{aligned} \quad (2.9)$$

The Larmor frequency  $\vec{\nu}_0$  is thus directly proportional to the applied magnetic field  $\vec{B}_0$  and also to the gyromagnetic ratio  $\gamma$ , which is characteristic for the particle under investigation.

A magnetic moment in an external magnetic field also has an associated magnetic energy defined as:

$$E = -\vec{\mu} \cdot \vec{B}_0 = -\mu B_0 \cos \theta \quad (2.10)$$

where  $\theta$  is the angle between the magnetic moment  $\vec{\mu}$  and the external magnetic field  $\vec{B}_0$ . Equation (2.10) indicates that magnetic energy is minimised when  $\vec{\mu}$  is parallel with  $\vec{B}_0$  and maximised when  $\vec{\mu}$  is antiparallel with  $\vec{B}_0$ . According to classical description the magnetic moment may assume any orientation, with energy varying between  $+\mu B_0$  and  $-\mu B_0$ .

Therefore, classical mechanics cannot explain how the general resonance condition for spectroscopy,  $\Delta E = h\nu$ , relates to the magnetic energy associated with the magnetic moment. A quantum - mechanical treatment is necessary to explain NMR resonance and the interaction of electromagnetic waves and nuclear spins.

## 2. THEORETICAL BACKGROUND

---

### Quantum - mechanical description

In classical mechanics one can prove that the angular momentum defined to be  $\vec{r} \times \vec{p}$  is the generator of a rotation; in contrast, in quantum mechanics we define the angular momentum operator  $\hat{\vec{J}} = \hbar \hat{\vec{I}}$  so that the operator for an infinitesimal rotation takes form:

$$\mathcal{D}(\vec{n}, d\phi) = 1 - i \left( \frac{\hat{\vec{J}} \cdot \vec{n}}{\hbar} \right) d\phi \quad (2.11)$$

for a rotation about the direction charcaterised by a unit vector  $\vec{n}$  by an infinitesimal angle  $d\phi$ . This is important because spin angular momentum to which our general formalism also applies, has nothing to do with Euklidean space ( $\mathbb{R}^3$ ). The wave function of a free spin is defined in Hilbert space. Quantum mechanics theory proves that angular momentum commutation relations are:

$$\left[ \hat{I}_i, \hat{I}_j \right] = i \epsilon_{ijk} \hat{I}_k \quad (2.12)$$

Because of Equation (2.12), the rotation group in three dimensions is said non - Abelian, that is rotation about different axis fail to commute. The first important property we derive from the basic commutation relations is the existence of a new operator  $\hat{I}^2$  defined by

$$\hat{I}^2 = \hat{I}_x \hat{I}_x + \hat{I}_y \hat{I}_y + \hat{I}_z \hat{I}_z \quad (2.13)$$

that commutes with every one of  $\hat{I}_k$ :

$$\left[ \hat{I}^2, \hat{I}_k \right] = 0, \quad (k = x, y, z) \quad (2.14)$$

Because components of angular momentum do not commute each other, only one of them can be choosen to be the observable to be diagonalised simultaneously with  $\hat{I}^2$ . By convention  $\hat{I}_z$  is choosen for this purpose. Studying the simultaneous eigenkets and their eigenvalue spectrum of operators  $\hat{I}^2$  and  $\hat{I}_z$ , the following equations can be derived:

$$\hat{I}^2 |I, m\rangle = I(I + 1) |I, m\rangle \quad (2.15)$$

$$\hat{I}_z |I, m\rangle = m |I, m\rangle \quad (2.16)$$

with  $I$  either an integer or a half - integer and  $m$  given by:

$$m = \underbrace{I, I - 1, I - 2, \dots, -I}_{2I+1 \text{ states}} \quad (2.17)$$

The quantization of angular momentum manifested in Equations (2.15 and 2.16) is a direct consequence of the angular momentum commutation relations, which,

## 2.1. Nuclear Magnetic Resonance

---

in turn follow from the properties of rotations together with the definition of  $\widehat{I}$  as the generator of rotation.

In the Heisenberg representation the equations of motion of the angular momentum operator  $\widehat{hI}$  are:

$$\frac{\hbar d\widehat{I}}{i dt} = [\mathcal{H}, \widehat{I}] = [-\gamma\hbar\vec{B}_0 \cdot \widehat{I}, \widehat{I}] \quad (2.18)$$

where  $\mathcal{H} = -\gamma\hbar\vec{B}_0 \cdot \widehat{I}$  is the Hamiltonian describing the coupling of the spin with the applied magnetic field. For the z component:

$$\frac{\hbar d\widehat{I}_z}{i dt} = -\gamma\hbar B_{0x} [\widehat{I}_x, \widehat{I}_z] + -\gamma\hbar B_{0y} [\widehat{I}_y, \widehat{I}_z] = \frac{\gamma\hbar}{i} [\widehat{I} \times \vec{B}_0] \quad (2.19)$$

This equation has the same form as the classical Equation (2.7). This identity has the following consequence: the expectation value  $\langle \widehat{I}_z \rangle$  taken over the wave function of a free spin  $\widehat{I}$  also obeys the classical equation and can therefore be calculated classically.

$$\frac{d}{dt} \langle \widehat{\mu} \rangle = \gamma \langle \widehat{\mu} \rangle \times \vec{B}_0 \quad (2.20)$$

where  $\widehat{\mu} = \gamma\widehat{I}$ . Since the angular momentum is quantized, the magnetic moment will also be quantized. The component of the magnetic moment along the longitudinal z axis is given by:

$$\widehat{\mu}_z |I, m\rangle = \gamma m |I, m\rangle \quad (2.21)$$

In the absence of an external magnetic field, each of the  $2I + 1$  states with the same values of  $I$  but different values of  $m_I$  are degenerate, meaning that they have the same energy. In an external magnetic field  $\vec{B}_0$ , the particles acquire a magnetic energy given by:

$$\mathcal{H} = -\widehat{\mu} \cdot \vec{B}_0 \quad (2.22)$$

Considering an external static magnetic field applied along z direction,  $B_0 = (0, 0, B_0)$ , Equation (2.22) gives:

$$\mathcal{H}_z = -\gamma\widehat{I}_z \cdot B_0 \quad (2.23)$$

It follows that the Schrödinger equation of the free spin is:

$$\mathcal{H} |I, m\rangle = E_m |I, m\rangle \quad (2.24)$$

## 2. THEORETICAL BACKGROUND

---

The energy eigenvalues of a free spin in an external static magnetic field applied along z direction are:

$$E_m = \gamma \hbar m B_0 \quad (2.25)$$

Since  $m$  is a discrete quantum number [see Equation (2.17)], the energy levels are also quantised. For a particle of spin  $I = 1/2$ , there are only two energy levels ( $m = \pm 1/2$ ) and the energy difference  $\Delta E$  is given by (see Figure 2.1):

$$\Delta E_m = \gamma \hbar B_0 \quad (2.26)$$

The resonance phenomenon in NMR is achieved by applying an oscillating mag-

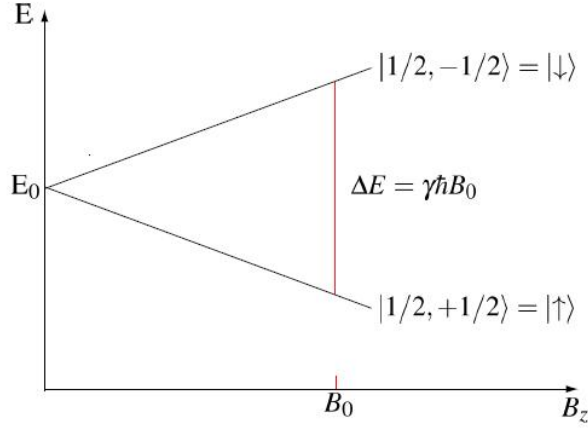


Figure 2.1: The nuclear spin energy for a spin  $1/2$  nucleus as a function of the external magnetic field strength  $B_0$ . By convention the lower energy level is referred to as  $\alpha$  or  $|\uparrow\rangle$  spin state, while the higher energy level is referred to as  $\beta$  or  $|\downarrow\rangle$  spin state. For all currently available magnets, the energy difference between the two spin states corresponds to electromagnetic radiation in the RF range.

netic field perpendicular to  $\vec{B}_0$  with a frequency  $\omega_0$ , such that the energy equals the magnetic energy given by equation (2.26), i.e the energy of the electromagnetic wave is given by:

$$\Delta E_m = \hbar \omega_0 \quad (2.27)$$

Combining Equations (2.26) and (2.27) yields the Larmor equation:

$$\omega_0 = \gamma B_0 \quad (2.28)$$

Even though the classical and the quantum - mechanical description of NMR lead to the same result, they play a different role in the understanding of the technique. Quantum mechanics is the only theory which can quantitatively describe the NMR phenomenon.

### 2.1.2 Macroscopic magnetisation

Figure (2.2) shows the precession (at the Larmor frequency) of a magnetic mo-

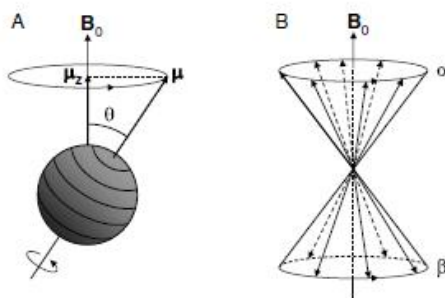


Figure 2.2: (A) Classical magnetic moment precession in an external magnetic field  $B_0$ . The spin magnetic moment  $\vec{\mu}$  precesses about  $B_0$ , in which the orientation  $\theta$  and the amplitude (along  $z$ )  $\mu_z$  are quantized. (B) For a single nuclear spin  $1/2$ , the spin state is described by a linear combination of  $\alpha$  ( $|\uparrow\rangle$ ) and  $\beta$  ( $|\downarrow\rangle$ ) states.

ment around an external magnetic field according to classical principles. Quantization of magnetic moment (and magnetic energy) can readily be incorporated in this picture. For elementary particles the angle  $\theta$  between  $\vec{\mu}$  and  $\vec{B}_0$  can no longer be arbitrary as in Section (2.1.1) but is given by:

$$\cos\theta = \frac{m}{\sqrt{I(I+1)}} \quad (2.29)$$

In the general case of a spin  $I$  nucleus, the magnetic moments will be distributed on  $2I+1$  cones at discrete angles  $\theta$  as defined by Equation (2.29). For a spin  $1/2$  nucleus the two spin states  $m = \pm 1/2$  are often referred to as the  $\alpha$  and  $\beta$  spin states, respectively.

So far, only the behavior of individual nuclear spins has been considered. However, to understand NMR physics the magnetic behaviour of assemblies of large numbers of atoms nuclei has to be described. The existence of spin paramagnetism, that is, the appearance in a sample containing a large number of elementary spin moments of a net macroscopic magnetisation when placed in a magnetic field  $\vec{B}_0$ , is due to the fact that different orientations of the spins with respect to the field, described by different values of the quantum number  $I_z = m$  of the spin quantized along the field, correspond to different magnetic energies  $E_m$ . According to the fundamental Boltzmann law of statistical mechanics, the

## 2. THEORETICAL BACKGROUND

---

populations  $P_m$  of the energy levels are given by:

$$P(E_m) = \frac{e^{-E_m/k_B T}}{\sum_{m=-I}^I e^{-E_m/k_B T}} \quad (2.30)$$

where  $k$  is the Boltzmann constant,  $k_B = 1.38 \cdot 10^{-23}$ . For a single free spin in a static external magnetic field applied along  $z$  direction the expectation value of nuclear spin is given by:

$$\langle \hat{\mu}_z \rangle = \gamma \langle \hat{I}_z \rangle = \gamma \hbar \sum_{m=-I}^I m P(E_m) \quad (2.31)$$

The total net magnetic moment (i.e. the magnetisation density  $\vec{M}/V$ ) of a macroscopic sample is the resultant of the sum over all individual magnetic moments  $\vec{\mu}$ . Due to the population difference there will be a net component of  $\vec{M}$  parallel with  $B_0$  along the  $+z$  axis. At thermal equilibrium the magnitude of the longitudinal magnetisation,  $M_0$  is:

$$M_0 = \sum_{i=1}^N \frac{\langle \mu_z \rangle_i}{V} \quad (2.32)$$

Using Equation (2.30) it follows:

$$M_0 = N \gamma \hbar \frac{\sum_{m=-I}^I m e^{-\gamma \hbar m B_0 / k_B T}}{\sum_{m=-I}^I e^{-\gamma \hbar m B_0 / k_B T}} \quad (2.33)$$

In nuclear magnetism, where the ratio  $\gamma \hbar m B_0 / k_B T$  is usually a very small number, it is permissible to make a linear expansion of the Boltzmann exponential, thus obtaining:

$$M_0 \simeq \frac{N \gamma^2 \hbar^2 B_0}{kT} \cdot \frac{\sum_{m=-I}^I m^2}{2I + 1} = \frac{N \gamma^2 \hbar^2 I(I + 1)}{3kT} \cdot B_0 = \chi_0 B_0 \quad (2.34)$$

where  $\chi_0$  is the static nuclear susceptibility. The proportionality of  $\chi_0$  to  $1/T$  is the well known Curie law. Since the final received signal is proportional to the population difference, NMR is a rather insensitive technique compared with other forms of spectroscopy, where the energy difference is much larger.

From Equation (2.34) several important features concerning the sensitivity of NMR experiments can be deduced. The quadratic dependence of  $M_0$  on the gyromagnetic ratio  $\gamma$  implies that nuclei resonating at high frequency, Equation (2.28), also generate relatively intense NMR signals. The linear dependence of  $M_0$  on the magnetic field strength  $B_0$  implies that higher magnetic fields improve the sensitivity. Finally, the inverse proportionality of  $M_0$  to the temperature  $T$  indicates that sensitivity can be enhanced at lower sample temperatures. Obviously, the latter option is unrealistic for in vivo applications.

## 2.1. Nuclear Magnetic Resonance

Table 2.1: NMR properties of commonly encountered nuclei in vivo NMR [de Graaf]

| Isotope           | Spin | Gyromagnetic ratio<br>( $10^7 \text{ rad T}^{-1} \text{ s}^{-1}$ ) | NMR frequency<br>at 2.35 T (MHz) | Natural<br>abundance (%) |
|-------------------|------|--|----------------------------------|--------------------------|
| $^1\text{H}$      | 1/2  | 26.752   | 100                              | 99.985                   |
| $^3\text{He}$     | 1/2  | -20.380  | 76.181                           | $1.4 \times 10^{-4}$     |
| $^{13}\text{C}$   | 1/2  | 6.728  | 25.145                           | 1.108                    |
| $^{17}\text{O}$   | 5/2  | -3.628   | 13.562                           | 0.037                    |
| $^{31}\text{P}$   | 1/2  | 10.841   | 40.481                           | 100                      |
| $^{129}\text{Xe}$ | 1/2  | -7.452   | 27.856                           | 26.44                    |

### 2.1.3 Bloch equations

In Section (2.1.1) it was shown that, when placed in a magnetic field  $\vec{B}$ , the expectation value of the quantum - mechanical operator  $\hat{\mu}$  experiences a torque which is proportional to the time derivative of the angular momentum, Equations (2.20). Utilizing the fact that the magnetisation is the sum over all magnetic moments the expression of motion for a single magnetic moment can be generalized for the total magnetisation, giving:

$$\frac{d}{dt} \langle \hat{\mu} \rangle = \gamma \langle \hat{\mu} \rangle \times \vec{B}_0 \quad (2.35)$$

$$\frac{d\vec{m}_i}{dt} = \vec{m}_i \times \gamma \vec{B}(t) \longrightarrow \vec{M} = \sum \vec{m}_i \longrightarrow \frac{d\vec{M}}{dt} = \vec{M} \times \gamma \vec{B}(t) \quad (2.36)$$

where  $\vec{B}(t)$  may include time - varying components in addition to the static magnetic field  $B_0$ . At thermal equilibrium, in the absence of additional (time - varying) magnetic fields, Equation (2.37) simply expresses the fact that the  $z$  component of the magnetisation  $\vec{M}$  is constant, i.e.:

$$\frac{dM_z(t)}{dt} = 0 \quad (2.37)$$

In order to observe nuclear magnetisation, the precessional motion needs to be detected. However, at thermal equilibrium the spins have no phase coherence in the transverse plane and the net longitudinal magnetisation is a static vector parallel to  $\vec{B}_0$ . Nuclear magnetisation can only be observed by rotating the net longitudinal magnetisation towards the transverse plane. From Equation (2.37) it follows that  $M_z$  can be perturbed by a second magnetic field perpendicular to  $M_z$  and since this field is rotating at the Larmor frequency in the RF range of the electromagnetic spectrum, it is often referred to as a RF magnetic field.

## 2. THEORETICAL BACKGROUND

---

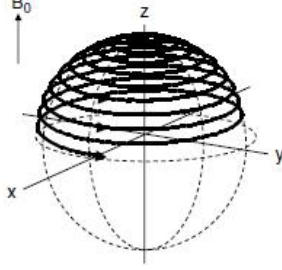


Figure 2.3: Excitation of magnetisation in the nonrotating, laboratory frame  $xyz$ . The longitudinal magnetisation  $\vec{M}_0$ , initially aligned with the  $z$  axis, will precess about the static magnetic field  $B_0$  and the irradiating RF field  $B_1$  in the transverse plane. This results in a rotation towards the transverse plane due to  $B_1$  and a simultaneous precession at the Larmor frequency about  $B_0$ . In this case  $B_1$  was calibrated to rotate  $\vec{M}_0$  by  $90^\circ$  away from the  $z$  axis to give complete excitation.

The magnetic component of a RF field that is linearly polarised along the  $x$  axis in the laboratory frame can be written as:

$$\vec{B}_{1x}(t) = 2B_{1max}\cos\omega t\vec{e}_x \quad (2.38)$$

where  $B_{1max}$  is the maximum amplitude of the applied field,  $\omega$  is the angular transmitter or carrier frequency of the RF field and  $\vec{e}_x$  represents a unit vector along the  $x$  axis. The linearly polarised field can be decomposed into two circularly polarised fields rotating in opposite direction about the  $z$  axis (Figure 2.4) according to:

$$\vec{B}_{1x}(t) = B_{1max}(\cos\omega t\vec{e}_x + \sin\omega t\vec{e}_y) + B_{1max}(\cos\omega t\vec{e}_x - \sin\omega t\vec{e}_y) \quad (2.39)$$

Only the field rotating in the same sense as the magnetic moment interacts significantly with the magnetic moment. Since under most conditions the counter rotating field can be ignored, the linearly polarised RF field of Equation (2.39) is then equivalent to a rotating magnetic field given by:

$$\vec{B}_{1x}(t) = B_{1max}(\cos\omega t[x] - \sin\omega t[y]) = \vec{B}_{1x}\cos\omega t + \vec{B}_{1y}\sin\omega t \quad (2.40)$$

where  $\vec{B}_{1x} = B_{1max}\vec{e}_x$  and  $\vec{B}_{1y} = B_{1max}\vec{e}_y$ . A similar expression can be derived for  $\vec{B}_{1y}(t)$ .

In the presence of two magnetic fields  $\vec{B}_0$  and  $\vec{B}_1$ , Equation (2.35) can be expanded to yield in the laboratory frame of reference in the absence of relaxation:

## 2.1. Nuclear Magnetic Resonance

---

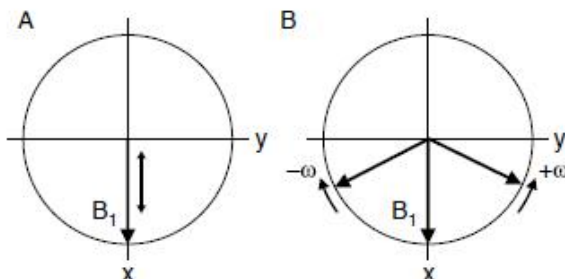


Figure 2.4: Decomposition of a linear oscillating magnetic field (A) into two rotating magnetic fields (B) with frequencies  $\omega$  and  $+\omega$ , respectively.

$$\frac{d\vec{M}_x(t)}{dt} = \gamma[\vec{M}_y(t)\vec{B}_0 - \vec{M}_z(t)\vec{B}_{1y}] \quad (2.41a)$$

$$\frac{d\vec{M}_y(t)}{dt} = \gamma[\vec{M}_z(t)\vec{B}_{1x} - \vec{M}_x(t)\vec{B}_0] \quad (2.41b)$$

$$\frac{d\vec{M}_z(t)}{dt} = \gamma[\vec{M}_x(t)\vec{B}_{1y} - \vec{M}_y(t)\vec{B}_{1x}] \quad (2.41c)$$

The term relaxation is widely used in the physical sciences to indicate the re-establishment of thermal equilibrium after some perturbation is applied. In the absence of a field all nuclear spin states are equally likely. When a magnetic field is applied, this situation no longer corresponds to equilibrium, and the system relaxes to the new equilibrium state, in which the spin polarisations are distributed anisotropically. If the magnetic field is suddenly switched off the nuclear spin magnetisation relaxes back to zero again, following an exponential decay. The components perpendicular (i.e.  $\vec{M}_x$  and  $\vec{M}_y$ ) and parallel (i.e.  $\vec{M}_z$ ) to  $\vec{B}_0$  relax with different time constants. The relaxation process was described by Bloch with three additional terms in the equation of motion for the magnetisation:

$$\frac{d\vec{M}_x(t)}{dt} = -\frac{\vec{M}_x(t)}{T_2} \quad (2.42a)$$

$$\frac{d\vec{M}_y(t)}{dt} = -\frac{\vec{M}_y(t)}{T_2} \quad (2.42b)$$

$$\frac{d\vec{M}_z(t)}{dt} = -\frac{\vec{M}_z(t) - M_0}{T_1} \quad (2.42c)$$

$T_1$  and  $T_2$  are relaxation time constants.  $T_1$  is the longitudinal relaxation time and reflects in principle a process in which energy from the spins is transferred

## 2. THEORETICAL BACKGROUND

---

to the surrounding lattice (which can be either solid or liquid), for this reason it is also referred to as spin - lattice relaxation time.  $T_2$  is the transverse relaxation time and reflects an entropy process, since spins exchange energy mutually (there is no net energy transfer) causing a decrease and loss of phase coherence (i.e. an increase in entropy).  $T_2$  is also referred to as spin - spin relaxation time.

Combining Equations (2.41) and (2.42) yields the Bloch equations in the laboratory frame:

$$\frac{d\vec{M}_x(t)}{dt} = \gamma[\vec{M}_y(t)\vec{B}_0 - \vec{M}_z(t)\vec{B}_{1y}] - \frac{\vec{M}_x(t)}{T_2} \quad (2.43a)$$

$$\frac{d\vec{M}_y(t)}{dt} = \gamma[\vec{M}_z(t)\vec{B}_{1x} - \vec{M}_x(t)\vec{B}_0] - \frac{\vec{M}_y(t)}{T_2} \quad (2.43b)$$

$$\frac{d\vec{M}_z(t)}{dt} = \gamma[\vec{M}_x(t)\vec{B}_{1y} - \vec{M}_y(t)\vec{B}_{1x}] - \frac{\vec{M}_z(t) - M_0}{T_1} \quad (2.43c)$$

Until this point the NMR experiment has been described in a Cartesian frame fixed with respect to the laboratory (i.e. the laboratory frame). It turns out to be more convenient to describe NMR in a rotating frame. Therefore, consider a new set of Cartesian axes ( $x'$ ,  $y'$  and  $z'$ ) where  $x'$  and  $y'$  rotate about the static magnetic field  $\vec{B}_0$  with frequency  $\omega$  and  $z' = z$ . The components of the magnetisation in the rotating frame are given by:

$$\vec{M}'_x = \vec{M}_x \cos \omega t + \vec{M}_y \sin \omega t \quad (2.44a)$$

$$\vec{M}'_y = \vec{M}_y \cos \omega t + \vec{M}_x \sin \omega t \quad (2.44b)$$

$$\vec{M}'_z = \vec{M}_z \quad (2.44c)$$

Therefore, using equations (2.44) and equations (2.43), the Bloch equations in the rotating frame can be written as:

$$\frac{d\vec{M}'_x(t)}{dt} = -(\omega_0 - \omega)\vec{M}'_y(t) - \gamma\vec{B}'_{1y}\vec{M}'_z(t)\frac{\vec{M}'_x(t)}{T_2} \quad (2.45a)$$

$$\frac{d\vec{M}'_y(t)}{dt} = (\omega_0 - \omega)\vec{M}'_x(t) + \gamma\vec{B}'_{1x}\vec{M}'_z(t)\frac{\vec{M}'_y(t)}{T_2} \quad (2.45b)$$

$$\frac{d\vec{M}'_z(t)}{dt} = \gamma\vec{B}'_{1y}\vec{M}'_x(t) - \gamma\vec{B}'_{1x}\vec{M}'_y(t)\frac{\vec{M}'_z(t) - M_0}{T_1} \quad (2.45c)$$

The conversion to a rotating frame of reference has consequences for the magnetic field vectors encountered in that frame. In a frame that rotates with a frequency equal to the frequency of  $\vec{B}_1$ ,  $\vec{B}_1$  appears static. Furthermore, the precessional motion of the magnetisation appears to be reduced to a value  $(\omega_0 - \omega)$ . Figure

## 2.1. Nuclear Magnetic Resonance

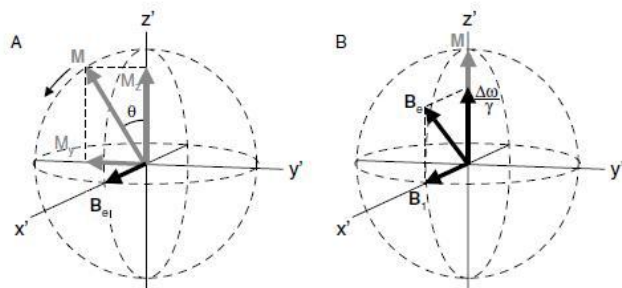


Figure 2.5: Magnetic field vectors encountered in the rotating frame of reference during excitation. (A) On-resonance ( $\vec{B}_1 = \vec{B}_e$ ). (B) Off-resonance.

(2.5) shows the generation of transverse magnetisation for  $\omega = \omega_0$ . Since the vectors are drawn in the rotating frame of reference, the magnetisation simply precesses about the applied  $\vec{B}_1$  field towards the transverse plane. Comparison with Figure (2.3), which shows the same situation in the laboratory frame illustrates the advantage of a rotating frame. It is convenient to define an effective magnetic field  $\vec{B}_e$ , which is the vector sum of  $[(\omega_0 - \omega)/\gamma]\vec{e}_z$  and  $\vec{B}_1$ , since the magnetisation precesses about the effective field. On - resonance (i.e. when the frequency of the applied RF pulse equals the Larmor frequency,  $\omega = \omega_0$ ), the magnetisation simply rotates about  $\vec{B}_1$ . Off - resonance (i.e.  $\omega \neq \omega_0$ ), the effective magnetic field  $\vec{B}_e$  is tilted from the transverse plane leading to a more complex rotation when compared with the on - resonance situation.

### 2.1.4 NMR Signal

As described before, following an on - resonance RF pulse, the magnetisation precesses about  $\vec{B}_0$  at the Larmor frequency and induces an electromagnetic field (EMF). Using an NMR spectrometer, it is possible to detect this small oscillating current by using a sensitive RF detector, called probe (consisting of coil, preamplifier, duplex). The oscillating electric current induced by the precessing nuclear transverse magnetisation is called the NMR signal or free - induction decay (FID).

The NMR spectrometer is basically a device capable of: (i) magnetising the nuclear spins by a large applied magnetic field; (ii) rotating the spin polarisations by RF pulses to produce transverse nuclear magnetisation; (iii) detecting the small oscillating electric currents induced by the precessing transverse spin magnetisation.

Because of  $T_2$  relaxation, the transverse magnetisation and consequently the EMF will decrease as a function of time. However, macroscopic and microscopic inhomogeneity in the main magnetic field  $\vec{B}_0$  will create a distribution of locally

## 2. THEORETICAL BACKGROUND

different magnetic fields across the sample, leading to a distribution of Larmor frequencies. This distribution leads to a more rapid loss of transverse magnetisation than caused by pure spin - spin relaxation, so  $T_2^* < T_2$ . For a sample with uniform proton density and  $T_2$  relaxation time, the acquired signal in the presence of magnetic field inhomogeneity is given by:

$$\vec{M}_\perp(t) = \vec{M}_\perp(0)e^{-t/T_2} \int_r e^{+i\gamma\Delta B_0(r)t} dr = \vec{M}_\perp(0)e^{-t/T_2^*} \quad (2.46)$$

where  $\Delta B_0$  is related to  $B_0$  inhomogeneity,  $B_0(r)$  is the magnetic field at position  $\vec{r}$  and  $\vec{M}_\perp$  is the complex transverse magnetisation ( $\vec{M}_\perp = M_x + iM_y$ ). Note that even though the  $T_2^*$  relaxation is often presented as a single - exponential decay, it is a multi - exponential decay depending on the local magnetic field inhomogeneity of individual spin packets.

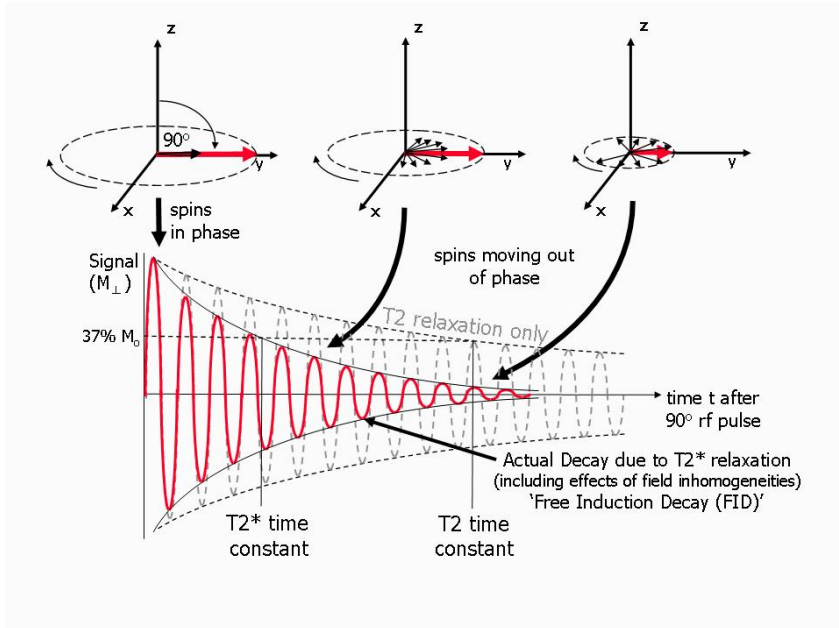


Figure 2.6: The amplitude of the net transverse magnetisation (and therefore the detected signal) decays as the spin packets move out of phase with one another (shown by the small black arrows). The resultant decaying signal is known as FID. The overall term for the observed loss of phase coherence (dephasing) is  $T_2^*$  relaxation, which combines the effect of  $T_2$  relaxation and additional de-phasing caused by local field variations (inhomogeneities)

NMR spectrometers separately detect the  $x$  and  $y$  components of the complex motion of the transverse magnetisation as function of time and commonly the

## 2.1. Nuclear Magnetic Resonance

---

projections on the  $x$  and  $y$  planes are shown, which are given by:

$$\vec{M}_x(t) = M_0 \cos[(\omega_0 - \omega)t + \phi] e^{-t/T_2^*} \quad (2.47)$$

$$\vec{M}_y(t) = M_0 \sin[(\omega_0 - \omega)t + \phi] e^{-t/T_2^*} \quad (2.48)$$

where  $\phi$  is the phase at  $t = 0$  and  $\vec{M}_x(t)$ ,  $\vec{M}_y(t)$  are referred to as the real and imaginary FIDs, respectively. Normally the time - domain data (i.e. the FID) is converted to frequency - domain data (i.e. the spectrum) by a Fourier transformation according to:

$$F(\omega) = \int_{-\infty}^{\infty} f(t) e^{-i\omega t} dt \quad \text{or} \quad F(\nu) = \int_{-\infty}^{\infty} f(t) e^{-i2\pi\nu t} dt \quad (2.49)$$

Fourier transformation of NMR the time - domain signal yields the real and imaginary frequency - domain signals (i.e. the spectrum) given by:

$$R(\omega) = A(\omega) \cos\phi - D(\omega) \sin\phi \quad (2.50)$$

$$I(\omega) = A(\omega) \sin\phi - D(\omega) \cos\phi \quad (2.51)$$

where

$$A(\omega) = \frac{M_0 T_2^*}{1 + (\omega_0 - \omega)^2 T_2^{*2}} \quad (2.52)$$

$$D(\omega) = \frac{M_0 (\omega_0 - \omega) T_2^{*2}}{1 + (\omega_0 - \omega)^2 T_2^{*2}} \quad (2.53)$$

$A(\omega)$  and  $D(\omega)$  describe the absorption and dispersion components of a Lorentzian lineshape. The width at half height,  $\Delta\nu_{1/2}$ , of the absorption component of a Lorentzian lineshape equals  $1/(\pi T_2^*)$ . The dispersive component is substantially broader, with a net integrated intensity of zero. Therefore, for the best separation (or resolution) of multiple lines in a NMR spectrum, absorption mode spectra are generally desired. Pure absorption mode spectra can be obtained by phasing the observed, mixed  $R(\omega)$  and  $I(\omega)$  spectra.

### 2.1.5 Chemical shift

So far most of the descriptions assumed a macroscopic sample containing only one type of nuclear spin, having a resonance frequency given by the Larmor equation (2.28). If the frequency of nuclear spins were solely determined by the resonance condition, NMR spectroscopy would be of minor importance in chemistry and medicine. However, the resonance frequency not only depends on the gyromagnetic ratio  $\gamma$  and the external magnetic field  $\vec{B}_0$ , but is also highly

## 2. THEORETICAL BACKGROUND

sensitive to the chemical environment of the nucleus under investigation. This is commonly referred to as the chemical shift.

The phenomenon of chemical shift is caused by shielding of nuclei from the external magnetic field by the electron cloud surrounding them. The precession of electrons from the electron cloud in an applied magnetic field is equivalent to an electric current, producing a field which opposes the applied field. Furthermore, the external field polarises the electronic shells, producing an additional magnetic field at the nucleus. Further contributions result from interactions of the electron shell with those of surrounding atoms (medium dependent). This effect can be

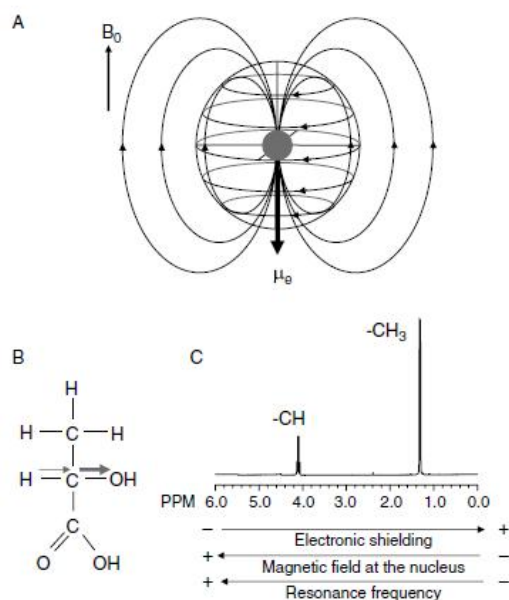


Figure 2.7: Origin of the chemical shift. (A) The electrons surrounding a nucleus shield the external magnetic field, thus reducing the magnetic field at the nucleus, leading to a different Larmor frequency (chemical shift). (B) Nuclei of the same element (or isotope) in different chemical environments have different chemical shift. Giving rise to multiline NMR spectra.

expressed by introducing an effective magnetic field  $\vec{B}_{eff}$  at the nucleus:

$$\vec{B}_{eff} = \vec{B}_0(1 - \sigma^j) \quad (2.54)$$

where  $\sigma^j$  is the chemical shift tensor (2<sup>nd</sup> order) of the nuclear site  $I_j$ . In isotropic liquids and gases, the molecules tumble rapidly through every conceivable molecular orientation, with equal probability for each orientation. The observed chemical

## 2.1. Nuclear Magnetic Resonance

---

shift is therefore the isotropic average of  $\sigma^j$  and is then a scalar quantity independent on the orientation of the sample with respect to the magnetic field that can be interpreted as a shielding constant. Using equation (2.54) the resonance condition (2.28) becomes:

$$\nu = \left( \frac{\gamma}{2\pi} \right) B_0(1 - \sigma) \quad (2.55)$$

Most often chemical shifts are not expressed in units of Hertz, since makes chemical shifts dependent on the magnetic field strength. Instead chemical shifts are expressed in relative terms of ppm (parts per million). By convention the chemical shift is defined as:

$$\delta = \frac{\nu - \nu_{ref}}{\nu_{ref}} \times 10^6 \quad (2.56)$$

where  $\nu$  and  $\nu_{ref}$  are the frequencies of the compound under investigation and of a reference compound, respectively. The reference compound should ideally be chemically inert and its chemical shift should be independent of external variables and should produce a strong (singlet) resonance signal well separated from all other resonances.

### 2.1.6 $T_1$ Relaxation

In Section (2.1.3),  $T_1$  and  $T_2$  were introduced as longitudinal (spin - lattice) relaxation and transverse (spin - spin) relaxation time, respectively.  $T_1$  and  $T_2$  relaxation are fundamental to NMR because they essentially affect any NMR experiment. In particular, knowledge of  $T_1$  relaxation is required for signal quantification, the study of chemical exchange and the design of optimal timings of pulse sequence for data acquisition.

Consider a simple pulse - acquire experiment with an  $\alpha$  excitation pulse and a repetition time TR. After the RF pulse the magnetisation is flipped from  $z$  - axis, it recovers through  $T_1$  relaxation according to:

$$M_z(\alpha, T_1) = \frac{M_0(1 - e^{-TR/T_1})}{(1 - \cos\alpha e^{-TR/T_1})} \quad (2.57)$$

Note that Equations (2.57) is derived under the assumption that  $M_{\perp} = 0$  immediately prior to excitation. Experimentally this can be achieved by using  $TR > 5T_2$  or by applying magnetic field gradient crushers to dephase any remaining transverse magnetisation. Figure (2.8) shows the amount of longitudinal magnetisation over time when the sequence is continuously repeated, as would be the situation in the case of signal averaging. In the case of a  $90^\circ$  pulse the

## 2. THEORETICAL BACKGROUND

---

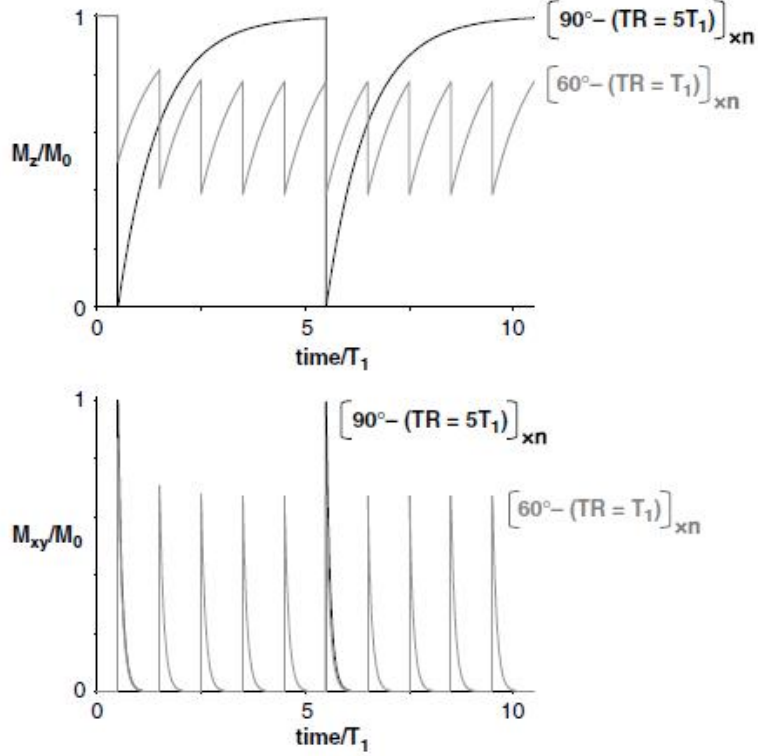


Figure 2.8: The effects of multiple excitations and  $T_1$  relaxation on the establishment of a longitudinal steady - state condition.

longitudinal magnetisation is reduced to zero after each pulse, after which it is allowed to recover through  $T_1$  relaxation according to (2.57), which reduces to  $M_z = M_0$  for  $TR > 5T_1$ . The amplitude of the transverse magnetisation is given by  $M_\perp = M_z \sin \alpha = M_0$ . However, even though full excitation is achieved during each scan, the experiment is not optimal in terms of signal per unit of time  $[= 0.2(M_0/T_1)]$  because the majority of scan time is used to wait for recovery of the longitudinal magnetisation. For this reason, data acquisitions with short repetition time are frequently used. However, for short TR acquisitions, the nutation angle  $\alpha$  plays a fundamental role. It is straightforward to show that the optimal nutation angle  $\alpha_{opt}$  for maximum signal per unit time is given by:

$$\alpha_{opt} = \arccos(e^{-TR/T_1}) \quad (2.58)$$

which is known as the Ernst angle. When  $TR > 5T_1$ , the exponential term vanishes and the optimal nutation angle is  $90^\circ$ . For shorter TR, the nutation angle gets smaller in order to reduce the saturation of longitudinal magnetisation and to maximise the acquired signal.

## 2.1. Nuclear Magnetic Resonance

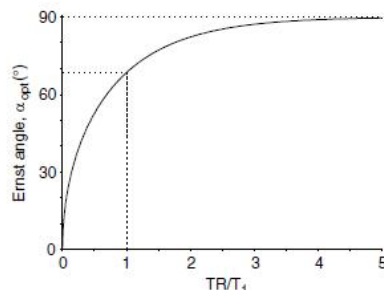


Figure 2.9: Graphical representation of the relation between the optimal nutation angle (Ernst angle, in degrees) and the ratio of repetition time  $TR$  to the  $T_1$  relaxation time.

### Inversion recovery sequence

The inversion recovery sequence is the "gold standard" technique for measuring the  $T_1$  relaxation time. The inversion recovery method consists of two pulses and two delays. The longitudinal magnetisation is inverted by a  $180^\circ$  pulse, then it partially recovers during a delay  $t$ , after which the longitudinal magnetisation is excited by a  $90^\circ$  pulse. Following data acquisition, the sequence can be repeated starting with recovery of longitudinal magnetisation during  $TR$ . The signal intensity  $M_z(t)$  during the recovery time is given by:

$$M_z(t) = M_0 - (1 - 2e^{-t/T_1}) \quad T_1 = \frac{t_{null}}{\ln 2} \quad (2.59)$$

where  $M_0$  is the longitudinal magnetisation at  $t = 0$  immediately after the inversion pulse. The  $T_1$  relaxation time constant can be obtained by acquiring NMR spectra at different recovery times between 0 and  $5T_1$ . Figure (2.10) shows typical inversion recovery spectra as a function of the recovery time. Fitting the integrated resonance areas to equation (2.59) gives an estimation of the  $T_1$  relaxation time.

### 2.1.7 $T_2$ Relaxation and spin-echoes

The observation of NMR signal depends upon the generation of phase coherence. The existence of phase coherence is finite due to  $T_2^*$  relaxation. According to Equation (2.46),  $T_2^*$  relaxation is composed of intrinsic  $T_2$  relaxation and dephasing by macroscopic and microscopic magnetic field inhomogeneity. Following a  $90^\circ$  pulse, phase coherence is generated which disappears with time constant  $T_2^*$ , thereby masking any information about  $T_2$ .

## 2. THEORETICAL BACKGROUND

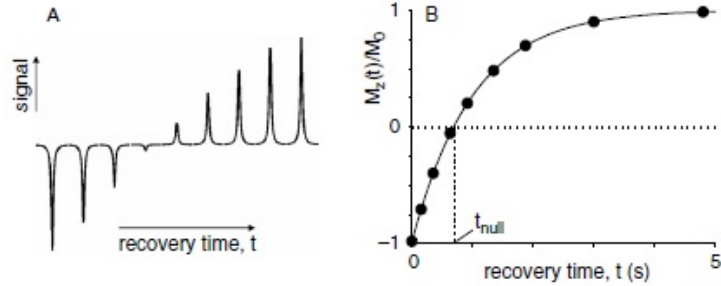


Figure 2.10: Measurement of  $T_1$  relaxation through the use of the inversion recovery method

However, through the generation of so - called spin - echoes it is possible to separate the contribution of  $T_2$  and magnetic field inhomogeneity. The first experiment was proposed by Hahn [Hahn, 1950]. In the Hahn sequence, the spins are excited by a  $90^\circ$  pulse after which they dephase in the transverse plane during the first half of the echo time, due to magnetic field inhomogeneity and frequency offsets. Then a  $180^\circ$  pulse tilts all magnetization vectors about the y axis (according to Figure 2.11), after which the spins rephase during the second half of the echo time due to the same magnetic field inhomogeneity and frequency offsets. At the echo time TE, the rephasing is complete and a spin - echo is formed. The Hahn sequence pulse time diagram is shown in Figure (2.11). The

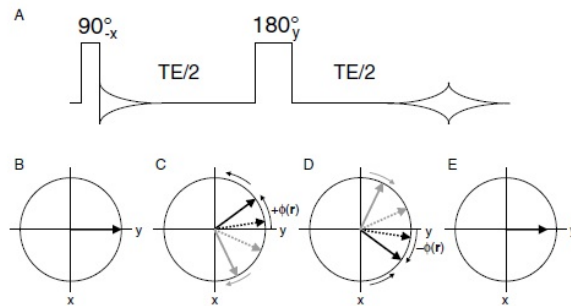


Figure 2.11: Spin - echo formation for uncoupled spins.

corresponding spectra can be fitted to an exponential curve, according to:

$$M_{\perp}(TE) = M_{\perp} e^{-TE/T_2} \quad (2.60)$$

An alternative method to measure  $T_2$  is the Carr - Purcell - Meiboom - Gill (CPMG) experiment, in which the single refocusing pulse is replaced by a train of successive  $180^\circ$  pulses.

## 2.2. Physical properties of Xenon (Xe)

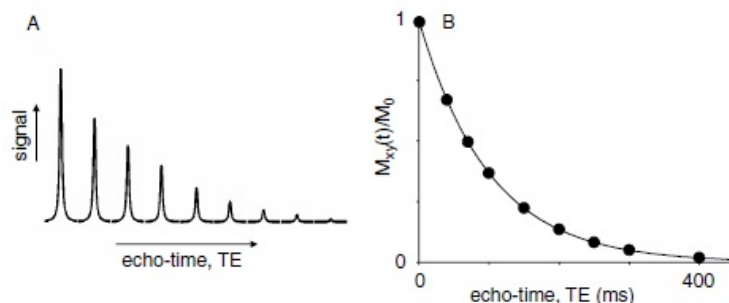


Figure 2.12: Measurement of  $T_2$  relaxation through the use of the spin - echo method.

## 2.2 Physical properties of Xenon (Xe)

Noble gases with nonzero nuclear spin are excellent NMR sensors for material science and biological tissue due to their very low reactivity and due to their very large range of chemical shifts, solubility and diffusivity. Some NMR properties of the stable noble gases with nonzero nuclear spin are listed in Table (2.2).

Table 2.2: Some physical properties of the stable noble gases

| Noble gas         | Spin | Boiling point<br>$T_b$ [K] | Melting point<br>$T_m$ [K] | Isotopic fraction<br>[%] | Gyromagnetic ratio<br>[kHz/G] |
|-------------------|------|----------------------------|----------------------------|--------------------------|-------------------------------|
| $^3\text{He}$     | 1/2  | 4.22                       | 0.95                       | $1.37 \times 10^{-4}$    | 3.2435                        |
| $^{21}\text{Ne}$  | 3/2  | 27.07                      | 24.56                      | 0.257                    | 0.3363                        |
| $^{83}\text{Kr}$  | 9/2  | 119,93                     | 115.79                     | 11.55                    | 0.164                         |
| $^{129}\text{Xe}$ | 1/2  | 165.15                     | 161.45                     | 26.44                    | 1.178                         |
| $^{131}\text{Xe}$ | 3/2  | 165.15                     | 161.45                     | 21.18                    | 0.349                         |

In this work we focus our discussion on the 1/2 spin noble gas  $^{129}\text{Xe}$ , that we employed for our experimental measurements.

Xenon, from the greek word *xeno*, stranger, was discovered in 1898 by William Ramsay and Morris Travers in the residue left after evaporating the other components of liquid air. Xenon is present as a trace gas in the atmosphere, at concentrations of 0.087 ppm. At room temperature and atmospheric pressure, xenon is a gas, but liquefies at moderate temperatures (160 K - 290 K) and pressures (1 bar - 60 bar). At liquid nitrogen temperatures Xe is a solid, this allows the accumulation and storage of laser - polarised xenon applying an external magnetic field [Gatzke et al., 1993]. Figure (2.13) shows the p - T phase diagram of Xenon [Cherubini and Bifone, 2003]; triple point [t.p. 161.3 K, 81.6 kPa], critical

## 2. THEORETICAL BACKGROUND

point [c.p. 289.7 K, 5.88 MPa].

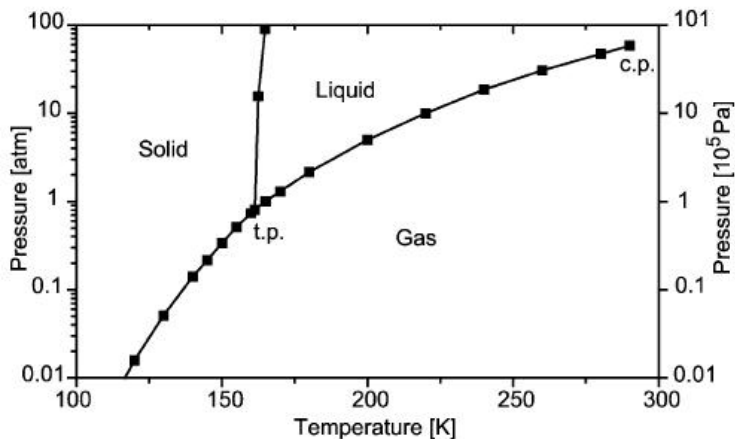


Figure 2.13: Phase diagram of Xenon [Cherubini and Bifone, 2003]

Xenon has an atomic number of  $Z = 54$  and an atomic mass of 131 a.u., resulting from a combination of nine naturally occurring isotopes with masses ranging from 124 to 136 a.u.; more than 35 unstable isotopes have been discovered. Two isotopes of xenon have very long radiocative half lives  $T_{1/2}$  ( $^{124}\text{Xe}$ , 0.01 % natural abundance,  $T_{1/2} \geq 1.6 \times 10^{14}$  years and  $^{136}\text{Xe}$ , 8.9 % natural abundance,  $T_{1/2} \geq 3.6 \times 10^{20}$  years). Moreover, natural xenon contains two isotopes with a nonzero spin quantum number,  $^{129}\text{Xe}$  and  $^{131}\text{Xe}$  with natural abundance 26.4 % and 21.29 % respectively. The basic NMR properties of these isotopes are given in Table (2.3).

Table 2.3: NMR properties of  $^{129}\text{Xe}$  and  $^{131}\text{Xe}$ : ground-state spin, magnetic moment  $\mu$ , gyromagnetic ratio, quadrupole moment, sensitivity relative to proton (assuming thermal polarization) [Oros and Shah, 2004].

| Isotope           | Spin | Magnetic moment<br>$\mu$ | Gyromagnetic ratio<br>[MHz/T] | Quadrupole moment | Sensitivity           |
|-------------------|------|--------------------------|-------------------------------|-------------------|-----------------------|
| $^{129}\text{Xe}$ | 1/2  | -0.7779763               | -11.7774                      | 0.00              | 0.021                 |
| $^{131}\text{Xe}$ | 3/2  | +0.6918619               | +3.4912                       | -0.120            | $2.76 \times 10^{-3}$ |

In particular,  $^{129}\text{Xe}$  is an excellent NMR probe for the following reasons: the extremely long spin - lattice relaxation time ( $T_1$ ), that makes it possible to

## 2.2. Physical properties of Xenon (Xe)

optically polarise this nucleus for NMR applications; the large range of chemical shifts.

### 2.2.1 $^{129}\text{Xe}$ chemical shift

Due to its fully occupied external electronic orbitals, xenon is chemically inert. However, the large and highly polarisable electron cloud makes the Larmor frequency of xenon very sensitive to the chemical environment. Indeed, the chemical shift range of  $^{129}\text{Xe}$  extends over several thousand ppm; it is usually referenced to xenon gas extrapolated to zero density.

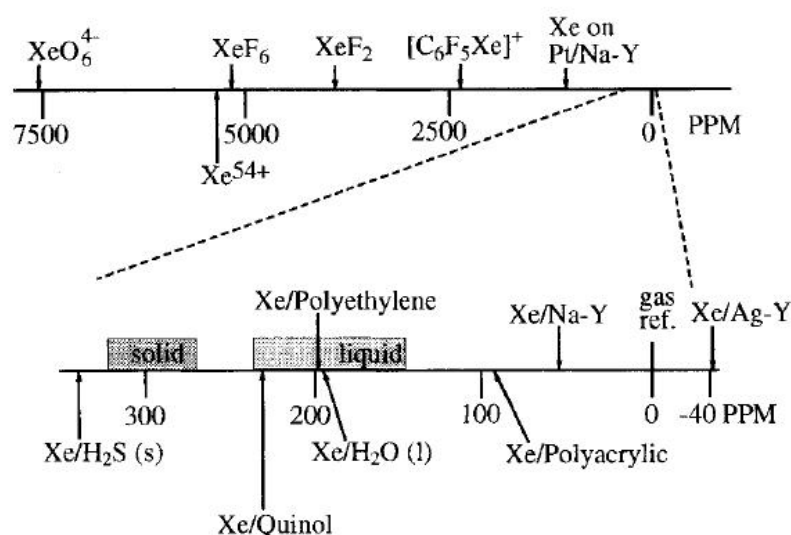


Figure 2.14:  $^{129}\text{Xe}$  chemical shift range [Pietraiss and Gaede, 1995]

Several studies investigating the influence of pressure and temperature on the chemical shift in gas, liquid, and solid, as well the underlying mechanism have been carried out in the past decades. In our experimental range of pressures and temperatures,  $^{129}\text{Xe}$  is in the gaseous phase. In xenon gas, the chemical shift is due to collisions between Xe atoms, which have a deshielding effect and depends on temperature and pressure. The chemical shift dependence on the temperature and pressure of the Xe gas has the general expression [Jameson et al., 1973]:

$$\sigma = \sigma_0 + \sigma_1(T)\rho + \sigma_2(T)\rho^2 + \dots \quad (2.61)$$

For Xe gas the first virial coefficient  $\sigma_0$  is constant (temperature independent) and is set by definition to zero,  $\sigma_1 = -0.553$  ppm/amagat at 298 K and showing temperature dependence, and  $\sigma_2 \sim -0.17 \times 10^{-3}$  ppm/amagat<sup>2</sup> (can be neglected for pressure below  $\sim 100$  amagat).

## 2. THEORETICAL BACKGROUND

---

### 2.3 Physical properties of Rubidium (Rb)

Alkali - metal atoms are suitable for SEOP for the following reasons: (i) they absorb the pumping light very efficiently because of their large electrical dipole moment; (ii) the ground state has optical transitions in the near infrared. Moreover, due to their relatively simple quantum - mechanical structure (one electron in the S - state) they have well defined selection rules. In our experimental measurements we used rubidium for SEOP of xenon gas.

Rubidium, which was discovered by Gustav Kirchhoff and Robert Bunsen in 1861, was the second element, following cesium, to be identified by use of the spectroscope, which they had invented the year before. Rubidium, from the Latin *rubidus*, which means deep red, was named after the red lines in its emission spectrum. [Weeks, 1932].

Rubidium is a silvery - white metal, soft, ductile, and, with a melting point of only  $t_{melting} = 38.9^\circ\text{C}$ , liquid at elevated ambient temperatures. As cited above, it is one of the alkali metals, atomic number 37, atomic weight 85.47, and electron configuration [Kr]5s1. In nature, rubidium consists of two isotopes that have atomic weights 85 and 87 and that occur in the proportions of 72.2 % and 27.8 %, by weight, respectively.  $^{87}\text{Rb}$  is slightly radioactive with a half - life of  $t_{1/2} = 4,88 \times 10^{10}$  years.

The number densities for Rb atoms, as a function of the absolute temperature  $T$ , have been determined from the vapor pressure curves [Cates et al., 1992; Killian, 1926]:

$$[Rb] = \frac{10^{(10.55-4132K/T)}}{k_B T} \quad (2.62)$$

where  $T$  is the absolute temperature in Kelvin and  $k_B = 1.38 \cdot 10^{-23}\text{J/K}$  is the Boltzmann constant. Typical Rb number densities present in optical pumping cells range from  $1.05 \cdot 10^{11} \text{ cm}^{-3}$  at 297 K to  $9.9 \cdot 10^{15} \text{ cm}^{-3}$  at 473 K. Figure (2.15) shows the number density of rubidium plotted as a function of temperature. In the temperature range used in the experimental measurements, we can notice a strong exponential dependence.

The nuclear spins of the two rubidium isotopes,  $^{87}\text{Rb}$  and  $^{85}\text{Rb}$ , are  $I = 3/2$  and  $I = 5/2$  respectively. The energy levels of an alkali - metal atom interacting with an external magnetic field,  $\vec{B}_z$ , are determined by the ground - state Hamilton operator [Happer, 1972]:

$$\hat{H} = \underbrace{A_g \hat{I} \cdot \hat{S}}_{\text{spin-spin}} + \underbrace{\gamma_S \hat{S}_z \cdot \vec{B}_z + \gamma_I \hat{I}_z \cdot \vec{B}_z}_{\text{Zeeman}} \quad (2.63)$$

The term  $A_g \hat{I} \cdot \hat{S}$  describes the hyperfine coupling of the alkali - metal nuclear spin to the electron spin in the ground state,  $\gamma_S \hat{S}_z \cdot \vec{B}_z$  and  $\gamma_I \hat{I}_z \cdot \vec{B}_z$  both are Zeeman

## 2.4. Optical pumping of noble gas nuclei

---

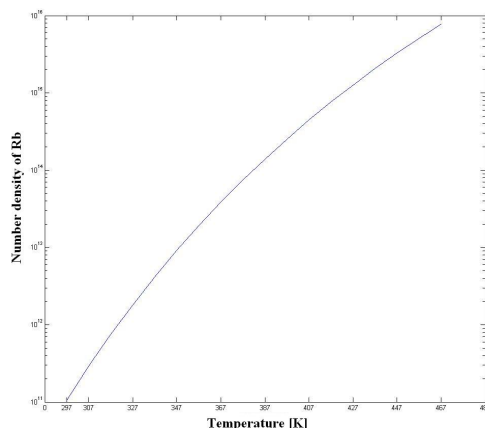


Figure 2.15: The temperature dependence of the Rb density [Rb] as a function of temperature in Kelvin from Equation (2.62). Note the logarithmic scale of the vertical axis.

terms describing the magnetic - dipole coupling of the nuclear and electron spin to the magnetic field, respectively. A similar expression can be derived for the first excited state  $^2P_{1/2}$ . Energy level schemes of  $^{87}\text{Rb}$  and  $^{85}\text{Rb}$  are shown in Figure (2.16).

Rubidium is an extremely reactive metal; it ignites spontaneously in the presence of air, and reacts violently with oxidizers, halogens and halogenated hydrocarbons, and water, which it decomposes under release of hydrogen. Because of its reactivity, in experimental applications on animals and humans it must be ensured that the inhaled gas is free of Rb. To ensure safety and purity, this metal is usually kept under a dry mineral oil or sealed in glass ampoules in an inert atmosphere.

## 2.4 Optical pumping of noble gas nuclei

Ever since the pioneering work of Hanle on the magnetic depolarisation of resonance light, it has been known that the excited atomic states that are produced by the absorption of anisotropic light are strongly polarised. In 1949, Kastler [Kastler, 1950] pointed out that the absorption and scattering of resonance light could lead to large population imbalances in atomic ground states as well as in excited states. The Nobel prize in physics 1966 was awarded to Alfred Kastler "for the discovery and development of optical methods for studying Hertzian resonances in atoms". After his work, ground state polarisation by optical pumping

## 2. THEORETICAL BACKGROUND

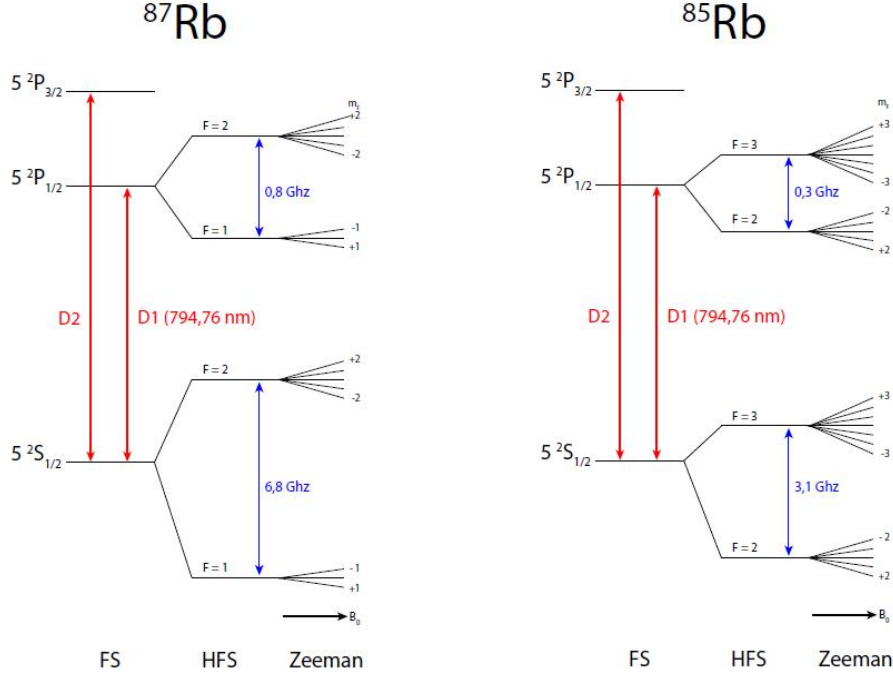


Figure 2.16: Energy level schemes of  $^{87}\text{Rb}$  and  $^{85}\text{Rb}$  with the fine structure (FS), the hyperfine structure (HFS) and the Zeeman levels.

was soon observed and became standard method for polarising noble gases via optically pumped alkali metals [Bouchiat et al., 1960].

In this work, experimental measurements have been carried out on a prototype continuous - flow Rb -  $^{129}\text{Xe}$  polariser. In our setup, the alkali - metal atoms are embedded in a high pressure gas mixture composed of: 90%  $^4\text{He}$  (buffer gas), 9%  $\text{N}_2$  (quenching gas) and 1%  $^{129}\text{Xe}$ . Circularly polarised light is absorbed by a saturated vapor of alkali - metal atoms, here Rb, polarising its ground state. Then, polarisation is transferred to  $^{129}\text{Xe}$  nuclei via spin - exchange. The spin exchange optical pumping process depends not only on the microscopic mechanisms, which will be further described in the following and have already been understood quite well, but also on macroscopic thermodynamical parameters that we investigated.

An in - depth description of the theoretical framework of optical pumping process can be found in the reviews [Happer, 1972; Walker and Happer, 1997], as well as in [Appelt et al., 1998].

### 2.4.1 Spin exchange optical pumping

The physics of spin exchange optical pumping can be schematically described as a two steps polarisation transfer mechanism. Polarisation is first transferred from circularly polarised light to alkali - metal atoms, then via spin exchange to noble gas nuclei. This, simplified, picture of SEOP is shown in Figure (2.17).

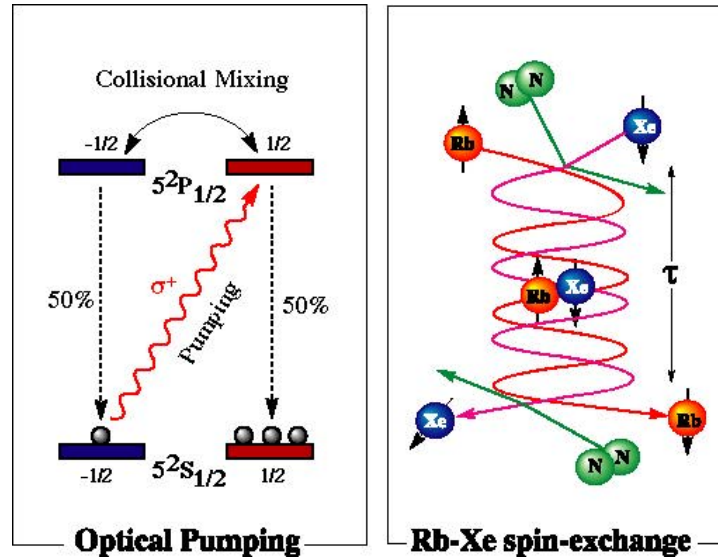


Figure 2.17: (Left) The optical pumping process which polarises the ground state of Rb. (Right) The spin exchange process between the polarised Rb electron spin and the Xe nuclear spin mediated through by the hyperfine interaction in binary collisions.

#### Optical pumping

The photon spin ( $s_z = 1$ ) of the circularly polarised laser beam, tuned to the  $D_1$  transition line of Rb, is transferred to alkali metal atoms. The selective optical transition from the  $5S_{1/2}$  to the  $5P_{1/2}$  ( $J = 1/2$ ;  $m_j = +1/2$ ) excited states depopulates only the  $m_s = -1/2$  ground state with an optical rate  $R$ , because for right circularly polarised light ( $s_z = 1$ ) no transition is allowed from the  $m_s = +1/2$  ground state to the two excited states. This follows from the conservation of angular momentum ( $\Delta L = +1$ ) of the Rb atom, but it does not affect the intrinsic electron spin orientation ( $\Delta s = 0$ ). After the  $m_j = +1/2$  state is selectively populated, frequent collisions with He atoms mixes the excited  $P_{1/2}$  state into an incoherent superposition of  $m_j = \pm 1/2$ . The collisional mixing leads to an equal population of the two excited state. Subsequent collisions with quenching

## 2. THEORETICAL BACKGROUND

---

gas molecules ( $N_2$ ) induce transitions from the excited state to the ground state. In high - pressure conditions, quenching collisional rate corresponds to an average life time of  $< 1$  ns which is much shorter than the natural excited state life time of about 30 ns. Therefore the excited Rb atoms decay nonradiatively to the ground state. The repopulation and depopulation pumping produces a ground state electron spin polarisation, which is destroyed with a rate  $\gamma_{sd}$  through collisions with Xe,  $N_2$  or He atoms.

### Spin exchange

Figure (2.17) shows the process which transfers electron spin polarisation from the Rb atoms to the nuclear spin of Xe atoms. Under high pressure conditions the main contribution is from binary collisions between Rb and Xe atoms in the gas phase which lead to short living Rb - Xe complexes. Quantum - mechanical treatment [Happer, 1972] shows that the Rb electron spin of the short living Rb - Xe complex has a non - vanishing probability for localization at the site the Xe - nuclear spin. This is the physical reason for the isotropic hyperfine coupling, also called Fermi contact interaction. The spin exchange transfer is mediated by flip - flop processes between Rb - electron spin and Xe - nuclear spin. At low gas pressure, the contribution for the spin exchange process mainly originates from long - lived van der Waals complexes. This three - body process has been intensively studied by Happer et al. [Happer et al., 1984].

### 2.4.2 Evolution of Rb - atom ground state

In this section the evolution of the ground state of Rb atom is described, including spatial diffusion, optical pumping, spin exchange, and spin relaxation process. Figure (2.18) shows schematically the atoms, molecules and electromagnetic fields involved in our spin exchange optical pumping experiment. The optical pumping cell, which is subject to a magnetic field  $B_z$ , is filled with 1 g of rubidium which, heated up to temperatures between  $60^\circ - 200^\circ C$ , builds an alkali - metal vapor. Rubidium atoms are embedded in a gas mixture of  $^4He$ ,  $N_2$ , and  $^{129}Xe$  and are pumped with a circularly polarised laser, which is propagating along the external magnetic field direction.

From the viewpoint of the alkali - metal atoms the following processes and interactions occur in the optical pumping cell: (a) spatial diffusion, (b) interactions with the magnetic field and with the pumping light, (c) electron spin exchange with other alkali - metal atoms, (d) electron spin relaxation due to the alkali - alkali atom collisions or all other buffer gas atoms, (e) spin exchange between electron spin of alkali - metal atoms and nuclear spin of noble gas atoms, (f) relaxation and exchange processes of the total alkali spin. Defining  $\hat{S}$  as the op-

## 2.4. Optical pumping of noble gas nuclei

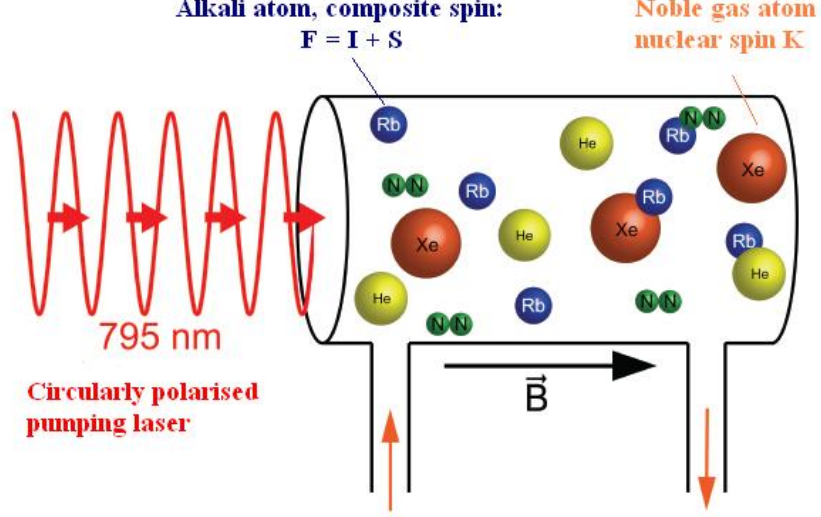


Figure 2.18: Atomic, molecular and radiative components involved in the SEOP experiment.

erator for the rubidium electron spin,  $\hat{F} = \hat{S} + \hat{I}$  as the total spin operator, with  $\hat{I}$  being the nuclear spin operator, and  $\hat{K}$  as the nuclear spin operator of xenon atom, the evolution of the ground state of the alkali - metal atom is given by [Appelt et al., 1998]:

$$\begin{aligned}
 \frac{\partial \hat{\rho}}{\partial t} = & \underbrace{D \nabla^2 \hat{\rho}}_a + \underbrace{\frac{1}{i\hbar} [H'_g, \hat{\rho}] + R [\varphi (1 + 2\hat{s} \cdot \hat{S}) - \hat{\rho}]}_b + \\
 & + \underbrace{\sum_j \gamma_{ex,ij} [\varphi (1 + 4 \langle \hat{S}_j \rangle \cdot \hat{S}) - \hat{\rho}]}_c + \underbrace{\gamma_{sd} [\varphi - \hat{\rho}]}_d + \underbrace{4\gamma_{se} \langle \hat{K} \rangle \cdot \hat{S} \varphi}_e + \\
 & + \underbrace{\frac{\gamma_{FD}}{[I]^2} [\hat{F} \cdot \hat{\rho} \hat{F} - \hat{F} \cdot \hat{F} \hat{\rho}] + \frac{\gamma_{FE}}{[I]^2} \langle \hat{K} \rangle \cdot (\{\hat{F}, \hat{\rho}\} - 2i\hat{F} \times -\hat{\rho} \hat{F})}_f
 \end{aligned} \tag{2.64}$$

The terms on the right side are discussed in the following:

- (a) The first term describes spatial diffusion of the alkali metal atoms, where  $D$  is the diffusion coefficient. Because the alkali metal atoms loose their polarisation completely through collisions with the walls of the pumping cell, the boundary condition for the density operator is  $\hat{\rho} = 0$ . Spatial

## 2. THEORETICAL BACKGROUND

---

diffusion in combination with optical pumping builds up a diffusion layer, where the alkali - metal polarisation grows exponentially from zero at the wall to the maximum equilibrium polarisation in the bulk.

- (b) The interaction with the laser light and the external magnetic field is given by the second term. Here,  $H'_g$  is the sum of the free alkali - metal Hamiltonian of the ground state (Equation 2.63) and Hamiltonians representing the interaction with radio frequency fields and small frequency - shifts associated with collisional and pumping process. The expression  $R[\varphi(1 + 2\hat{s} \cdot \hat{S}) - \hat{\rho}]$  describes the evolution of alkali - metal ground state due to depopulation and repopulation optical pumping.  $R$  is the mean optical pumping rate per unpolarised Rb atom and  $\hat{s}$  is the photon spin.
- (c) The third expression describes the electron spin exchange process, through collisions, between pairs of alkali - metal atoms. This exchange process can occur between like ( $i = j$ ) and unlike ( $i \neq j$ ) alkali - metal atoms. Here,  $\varphi$  is defined as the ground state density operator which has no electron spin polarisation, but which may contain some nuclear spin polarisation.
- (d) This term is also called  $\hat{S}$  - damping term. It accounts for the relaxation of density operator due to binary collision of Rb atoms with each other and with buffer gas atoms. These binary collisions destroy part of  $\hat{\rho}$  with electron polarisation, but do not affect the part  $\varphi$  with purely nuclear polarisation. The  $\hat{S}$  - damping term is characterised by the relaxation rate  $\gamma_{SD}$ , which will be discussed later.
- (e) The fifth term describes the transfer of polarisation between the nuclear spin  $\hat{K}$  of the noble gas and the alkali - metal electron spin  $\hat{S}$ . The binary spin exchange rate  $\gamma_{SE}$ , which will be discussed later, has contributions from binary collisions and short - lived van der Waals molecules.
- (f) The last term accounts for relaxation processes due to long - lived van der Waals molecules. These processes, called  $\hat{F}$  - damping and  $\hat{F}$  - exchange, are slow and cause Zeeman transitions within one hyperfine multiplet. At high gas pressure these slow relaxation processes can be neglected [Bouchiat et al., 1972].

### Spin destruction rate

The spin destruction rate is given by [Fink et al., 2005]:

$$\gamma_{SD} = \kappa_{Rb}n_{Rb} + \kappa_{Xe}n_{Xe} + \kappa_{N_2}n_{N_2} + \kappa_{He}n_{He} + \gamma_{SE} + \gamma_{trap} \quad (2.65)$$

## 2.4. Optical pumping of noble gas nuclei

---

where  $n_{Rb}$ ,  $n_{Xe}$ ,  $n_{N_2}$ ,  $n_{He}$  are the number densities of the different species and  $\kappa_{Rb}$ ,  $\kappa_{Xe}$ ,  $\kappa_{N_2}$ ,  $\kappa_{He}$  are the experimentally determined spin destruction coefficients for binary collisions with rubidium atoms (Table (2.4)).

The rubidium spin destruction rate  $\gamma_{SD}$  accounts for all spin polarisation destroying processes apart from wall relaxation. It contains contributions of binary collisions or alkali - metal atoms with each other and with buffer gas. Another important relaxation process is the radiation trapping, here called  $\gamma_{trap}$ , i. e., the depolarisation of a Rb atom by the interaction with a photon that has previously been emitted by another relaxing Rb atom. This relaxation mechanism is quenched by the nitrogen in the gas mixture.

### Spin exchange rate

The spin exchange rate, measuring the transfer of polarisation from the alkali electron spin to the noble gas nuclear spin, is given by [Fink et al., 2005]:

$$\gamma_{SE} = n_{Rb} \left( \langle \sigma v \rangle + \frac{\kappa_{SE,He}}{n_{He}} + \frac{\kappa_{SE,Xe}}{n_{Xe} \left( 1 + 0.275 \frac{n_{N_2}}{n_{Xe}} \right)} \right) \quad (2.66)$$

where  $\langle \sigma v \rangle$  is the experimentally measured cross section for spin - exchange binary collisions of rubidium and xenon,  $\kappa_{SE,He}$  and  $\kappa_{SE,Xe}$  are coefficients giving the probability of spin exchange via van der Waals molecules with helium and xenon as third interaction components (Table (2.4)).

Table 2.4: Spin destruction and spin exchange parameters for Rb - Xe spin exchange optical pumping [Fink et al., 2005]

| Coefficient                | Unit         | Value  |
|----------------------------|--------------|--|
| $\kappa_{Rb}$              | $m^3 s^{-1}$ | $3.9 \times 10^{-20}, 4.4 \times 10^{-20}$                           |
| $\kappa_{Xe}$              | $m^3 s^{-1}$ | $6 \times 10^{-21} \times 10.8$                                      |
| $\kappa_{N_2}$             | $m^3 s^{-1}$ | $9 \times 10^{-24}$  |
| $\kappa_{He}$              | $m^3 s^{-1}$ | $2 \times 10^{-24}$  |
| $\kappa_{SE,Xe}$           | $s^{-1}$     | $5.23 \times 10^3$   |
| $\kappa_{SE,He}$           | $s^{-1}$     | $1.7 \times 10^4$  |
| $\langle \sigma v \rangle$ | $m^3 s^{-1}$ | $0.6 \times 10^{-22}, 1.75 \times 10^{-22}$<br>$3.7 \times 10^{-22}$ |

### 2.4.3 Electronic spin polarisation of Rb

The concept of spin - temperature distribution for alkali - metal atoms in the case of very rapid spin exchange processes was introduced in 1959 by Anderson,

## 2. THEORETICAL BACKGROUND

---

Pipkin and Baird [Anderson et al., 1959]. The existence of a spin - temperature distribution leads to a simplified model for the steady - state population distribution at high gas pressure for SEOP processes.

The steady - state condition of equation (2.64), in our case of continuous longitudinal optical pumping in the  $z$  direction, is  $d\hat{\rho}/dt = 0$ . Assuming that all the exchange processes occur far from the cell wall, so that diffusion can be neglected and ignoring the slow relaxation processes, the solution of Equation (2.64) for  $\hat{\rho}$  in the absence of radio frequency excitation, is given by:

$$\hat{\rho} = \frac{e^{\beta K_z} e^{\beta S_z}}{Z_K Z_S} = \varphi(1 + 4 \langle S_z \rangle S_z) \quad (2.67)$$

where  $\beta = \ln\left(\frac{1+\langle P_{Rb} \rangle}{1-\langle P_{Rb} \rangle}\right)$  is the spin - temperature parameter, and  $\langle P_{Rb} \rangle = 2 \langle S_z \rangle$  is the overall spin polarisation. The Equation (2.67) characterises the whole alkali atoms ground state, for all sudden processes described above, by only a single spin temperature parameter.

Using the spin temperature solution of equation (2.67) in (2.64), it follows that the overall spin polarisation of rubidium atoms is given by:

$$\langle P_{Rb} \rangle = 2 \langle S_z \rangle = \frac{s_z R + 2\gamma_{SE} \langle K_z \rangle}{\gamma_{SD} + R} \approx \frac{s_z R}{\gamma_{SD} + R} \quad (2.68)$$

The last expression is due to the fact that for most practical cases, the optical pumping rate  $R$  is much larger than  $\gamma_{SE}$ .

In summary, the overall spin polarisation of rubidium atoms,  $P_{Rb}$ , during optical pumping is determined by a balance of polarisation induced by the absorption of circularly polarised laser light and depolarisation caused by collisions of the alkali metal atoms with buffer gas atoms.

### 2.4.4 Nuclear spin polarisation of $^{129}\text{Xe}$

The rate of production of polarised  $^{129}\text{Xe}$  via spin exchange with an optically pumped Rb vapor is proportional to the photon current  $\Delta I$  absorbed by the alkali metal [Driehuys et al., 1996]:

$$\frac{d}{dt} 2 \langle K_z \rangle [^{129}\text{Xe}]V = \eta \Delta I \quad (2.69)$$

where  $[^{129}\text{Xe}]V$  is the number of  $^{129}\text{Xe}$  atoms,  $K_z$  is the  $z$  component of the xenon nuclear spin, and  $\eta$  is a measure of the efficiency with which photon angular momentum is converted into nuclear spin angular momentum. Following the literature, the spin exchange efficiency in the  $^{129}\text{Xe}$  - Rb system is  $\eta = 0.07$ .

## 2.4. Optical pumping of noble gas nuclei

---

Besides the laser power, the maximum achievable polarisation of  $^{129}\text{Xe}$  depends on at least three other factors: (i) the spin exchange rate between Rb electron spin and  $^{129}\text{Xe}$  nuclear spin, (ii) the losses of nuclear spin polarisation due to relaxation processes in the pumping cell, (iii) the loss of polarisation during storage and delivery processes. Altogether, the nuclear spin polarisation of  $^{129}\text{Xe}$  achieved through spin exchange with optically pumped Rb vapor can be described as:

$$\frac{d}{dt} \langle P_{Xe} \rangle = \gamma_{SE}(\langle P_{Rb} \rangle - \langle P_{Xe} \rangle) - \gamma_{wall} \langle P_{Xe} \rangle \quad (2.70)$$

where  $\gamma_{SE}$  is the above discussed spin exchange rate and  $\gamma_{wall}$  is the total loss rate that accounts for the losses of nuclear spin polarisation due to wall relaxation and additional mechanisms. Assuming that  $\gamma_{SE}$ ,  $\gamma_{wall}$ , and number density of Rb are constant during the SEOP process, the solution of equation (2.70) is given by:

$$\langle P_{Xe} \rangle (t) = \frac{\gamma_{SE}}{\gamma_{SE} + \gamma_{SD}} \langle P_{Rb} \rangle (1 - \exp^{-(\gamma_{SE} + \gamma_{wall})t}) \quad (2.71)$$

For steady - state and long relaxation time  $t$ , a simple expression of the nuclear polarisation of  $^{129}\text{Xe}$  can be derived:

$$\langle P_{Xe} \rangle = \frac{\gamma_{SE}}{\gamma_{SE} + \gamma_{SD}} \langle P_{Rb} \rangle \quad (2.72)$$

The analogy between equation (2.72) and (2.68) is obvious. The overall polarisation of  $^{129}\text{Xe}$  atoms results from an equilibrium between the rate of polarisation transfer  $\gamma_{SE}$  to  $^{129}\text{Xe}$  through spin exchange collisions with Rb and the rate of polarisation loss  $\gamma_{wall}$ .

### Dependence on thermodynamical parameters

As cited above, the thermodynamical and aerodynamical processes in a pumping cell during SEOP of noble gases have not yet been studied in detail. [Fink et al., 2005] propose a theoretical model of the transport processes involved in SEOP. In particular, using a numerical approach, the influence of different thermodynamical parameters, such as temperature and gas partial pressures, have been analysed.

First we consider the external temperature, which is directly connected to the number densities of rubidium vapor within the cell and to the convection pattern. The dependence of the overall  $^{129}\text{Xe}$  polarisation on the temperature is shown in Figure (2.19). Numerical results show that the mean  $^{129}\text{Xe}$  spin polarisation increases linearly with the external temperature up to a maximum value, depending on the applied laser power. Upon further increasing temperature, the noble gas

## 2. THEORETICAL BACKGROUND

---

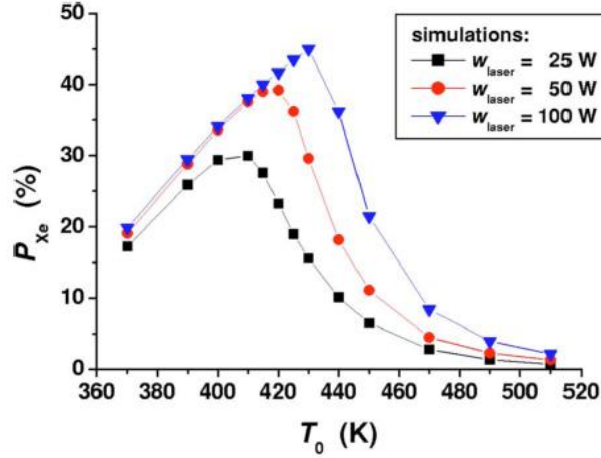


Figure 2.19: Dependence of mean  $^{129}\text{Xe}$  polarisation as a function of temperature.

polarisation decays exponentially. This result can be explained using Equation (2.65), which describes the spin destruction rate  $\gamma_{SD}$ . Increasing the external temperature, the number density of Rb becomes the dominant factor in the polarisation destruction process and we know from Equation (2.62) its dependence on temperature.

Concerning the pressure dependence of  $^{129}\text{Xe}$  polarisation, results from [Fink et al., 2005] are shown in Figure (2.20). Figure (2.20) shows that with increas-

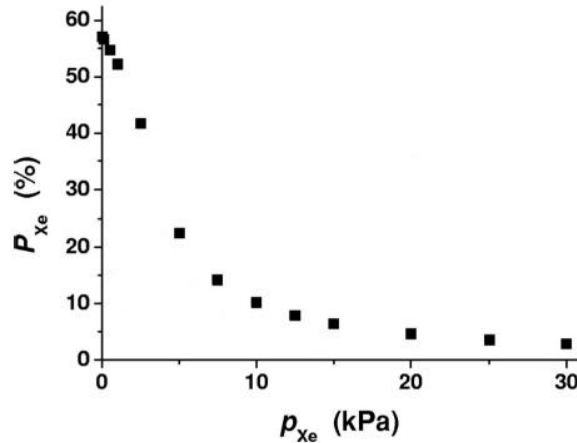


Figure 2.20: Dependence of mean  $^{129}\text{Xe}$  polarisation as a function of xenon partial pressure.

## 2.4. Optical pumping of noble gas nuclei

---

ing xenon partial pressure, the mean  $^{129}\text{Xe}$  polarisation decreases exponentially. However, the simulated pressure range is very large compared to our experimental conditions, ranging from 0.5 bar to 6 bar, which hampers direct comparison. Nevertheless, the exponential decay can be understood theoretically, because an increase of pressure means an increasing average number of collisions in the pumping cell.

Beside temperature and pressure, the polarisation of  $^{129}\text{Xe}$  achievable through SEOP with Rb vapor depends on several other thermodynamical processes and their interactions. For example, the so - called laser heating effect has been reported [Walter et al., 2001] which is connected to absorbed optical energy converted to thermal energy by Rb vapor during the optical pumping process. This heat transfer process is coupled to transport processes inside the pumping cell leading to convective phenomena. Moreover, rising temperature leads to increasing number density of Rb which causes a substantial decrease of the volume averaged Rb polarisation, because the pumping light cannot penetrate sufficiently into the cell. Another effect, also related to heating processes and Rb density, is the so - called Rb - runaway effect reported in [Zook et al., 2002]. At elevated temperatures, the cell temperature becomes unstable since the heating produces an increased Rb density that in turn further increases the optical absorption. As the region near the front window becomes optically dense, the laser light ceases to effectively pump the Rb vapor near the rear of the cell. These process produces a deep temperature gradient between the front and rear windows of the pumping cell, leading to turbulent transport phenomena and to an inefficient optical pumping of Rb vapor.



# Chapter 3

## Materials and methods

In this chapter, the design and operation of the hyperpolarisation equipment are described. Furthermore, the MR system, used to collect experimental data, is presented. Finally, an overview of data analysis is provided. A schematic drawing of the experimental setup is shown in Figure (3.1)

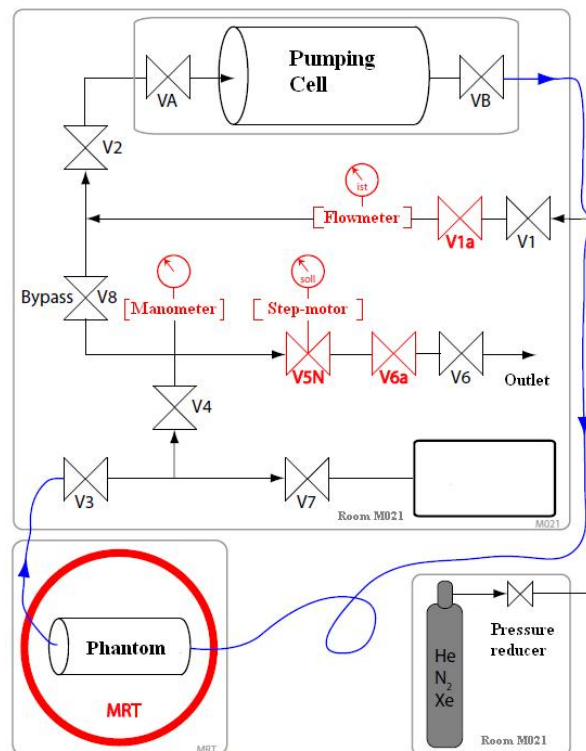


Figure 3.1: Schematic drawing of the Rb - Xe polariser, including the whole - body MR tomograph (MRT) to measure the absolute Xe polarisation.

## 3. MATERIALS AND METHODS

---

### 3.1 Hyperpolarisation equipment

In our experiment we use a prototype continuous - flow Rb - Xe polariser built by Stephan Appelt (FZ Julich, Germany). The hyperpolarisation device (HPD) was assembled and technically improved at DKFZ by Guido Antweiler (Hochschule Karlsruhe für Technik und Wirtschaft, Karlsruhe). In the next step, we improved several crucial components of the apparatus in order to optimise the production of hyperpolarised xenon and to enhance the degree of polarisation. The main components of the hyperpolarisation equipment, in detail described in the following sections, are: (i) valves system for gas mixture supply, (ii) the laser system and optical elements for pumping of rubidium, (iii) the polariser, containing the pumping cell.

#### 3.1.1 Gas supply system

In our experimental measurements we used a gas mixture (Air Liquide Medical GmbH, Leipzig). It was provided in an high - pressure container filled with 90.3% helium, 8.75% nitrogen and 0.95% xenon in natural abundances. Due to the high pressure, for safety issues, the gas bottle is stored in a special cabinet in a separate room. The pressure of the gas container is first reduced by a pressure transducer to 10 bar total gas pressure. Via an high - pressure pipeline, the gas mixture is delivered to the hyperpolarisation lab where the total gas pressure is further reduced, in a range between 1.5 bar and 7 bar, before flowing through the HPD.

#### 3.1.2 Laser system

The laser system used for optical pumping of Rb atoms was a cw - laser with a output power of 60 W (2xFAP Duo system, Coherent Inc., Santa Clara, USA). This unit is composed of two diodes, operating separately with a maximum output power of 30 W each, coupled to an optical fiber delivery system. The laser beam is tuned to the D<sub>1</sub> absorption line of rubidium,  $\lambda = 794.8$  nm (in the invisible near - infrared region), and has a Gaussian optical profile with linewidth ( $\Delta\lambda_{Laser}$ ) of 1.5 nm. By thermoelectric temperature control of the diodes, the wavelength of the maximum peak can be shifted by 0.28 nm/°C.

Due to its spectral region and the high output power, our laser system is classified as class - 4. The laser radiation of a class - 4 laser system is very dangerous for eyes and skin; diffusively scattered radiation can also be dangerous. Therefore, the laser system can be used only under strict safety regulation to avoid damages to the users.

For spatial adjustments and setup the laser system is provided by a low - energy visible beam, the so - called aim beam. Using the aim beam, we adjusted

### 3.1. Hyperpolarisation equipment

the laser system such that the entire pumping cell is irradiated. The laser beam has a cross section at the pumping cell window of about 40 mm, thus the delivered power per unit of area is  $0.48 \text{ mW/cm}^2$ .

#### Optical elements

As described in the theory Section (2.4.1), for selective optical pumping of Rb atoms, the irradiating laser light must be right - circularly polarised ( $\sigma^+$ ). This was achieved, using the optical unit shown in Figure (3.2).

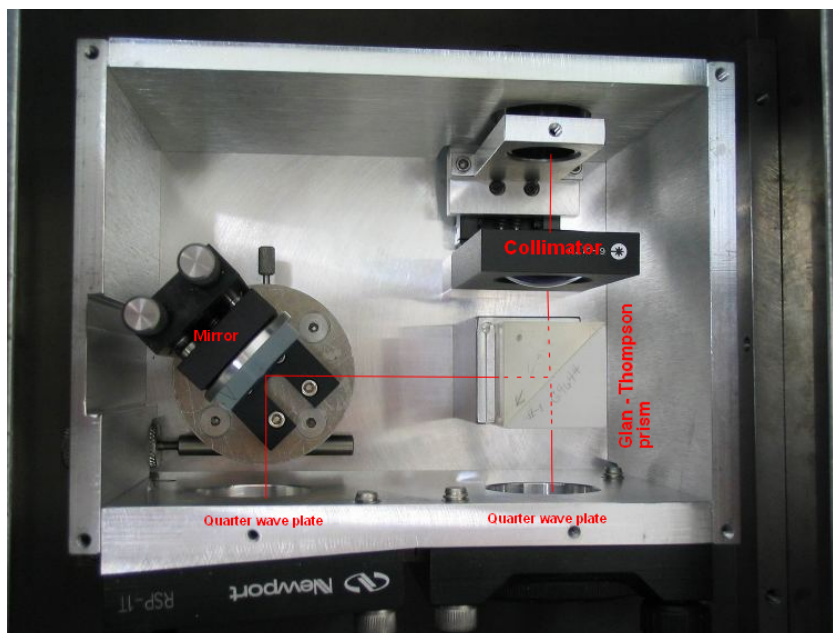


Figure 3.2: View of the optical unit.

The unpolarised beam emerging from the optical fiber cable enters the optical polariser where it is collimated before passing through a beam - splitting cube to divide the beam into horizontal and vertical polarisation components. The vertically polarised beam exits the optical polariser through a quarter wave plate. The horizontally polarised beam is reflected by an adjustable mirror and exits through a second quarter wave plate with the fast axis aligned parallel to the slow axis of the first quarter wave plate. The mirror mount is adjusted such that the two beams intersect at the pumping cell window. This optical unit arrangement permits the full power of the laser system to be circularly polarised even though the output of the fiber is unpolarised.

### 3. MATERIALS AND METHODS

---

#### IR - spectrometer

The maximum achievable  $^{129}\text{Xe}$  polarisation is directly proportional to the Rb polarisation, produced via optical pumping (Equation (2.69)). To determine the absorption of laser light by the Rb vapor, the laser output and transmission through the optical pumping cell was continuously monitored with a fiber - coupled optical spectrometer (getSpec 3648, Sentronic GmbH, Dresden). The detector of the spectrometer is a 3648 - pixel high - sensitive CCD SONY detector and can be used for measurements from 720 to 870 nm (in the near infrared), with high spectral resolution of up to 0.1 nm full width at half maximum (FWHM). The spectrometer has a fiber optic entrance connector (Standard SMA), collimating and focusing mirror and diffractive grating. A 2 - mm wide optical density filter (OPT getSpec 3005, Sentronic GmbH, Dresden), transmitting 1% of the laser power, was necessary to avoid saturation of the spectrometer detector. The spectrometer has an USB 2.0 interface which allows fast data sampling spectra and data transfer to pc - control unit.

#### 3.1.3 Rb - Xe polariser

The continuous - flow Rb - Xe polariser is a 60 x 51 x 51 cm<sup>3</sup> large metal box, containing the gas handling system and the optical pumping cell. A front view of the polariser is shown in Figure (3.3).

#### Gas handling system

In the front panel Figure (3.3) there are 7 valves, controlling the gas flow through the polariser. Two other valves (V1a and V6a), placed at the inlet and outlet of the polariser respectively, can be opened/closed by remote pc - unit to control the gas flow. At the top right of the front panel we have the inlet valve (V1), here the gas coming from the gas supply system flows in the polariser. Before flowing through the pumping cell, by valve V2 (top left), the gas flow is measured using a mass flowmeter (GFM17, Aalborg Instruments & Controls Inc., New York, USA). The mechanical layout of the flowmeter design includes an LCD readout and it is also connected to the pc - control unit. After measuring the flow, the gas mixture passes through the pumping cell where the hyperpolarised  $^{129}\text{Xe}$  is produced. Polyurethane (PU) tubes (Festo AG & Co. KG) are used to deliver the polarised gas to a made of plastic phantom (material: PVDF,  $V = (376.2 \pm 1.3)$  mL, EM-Technik GmbH, Maxdorf), placed in the MR tomograph where the hyperpolarisation of  $^{129}\text{Xe}$  is measured, and to bring it back to the polariser. On the way to the outlet valve (V6) a stepper motor and a manometer are installed, both connected to the pc - control unit. The stepper motor together with the flowmeter allows the control of the gas flow through the polariser. The

### 3.1. Hyperpolarisation equipment



Figure 3.3: Front view of Rb - Xe polariser.

### 3. MATERIALS AND METHODS

---

manometer has analogical and digital output and measures the total pressure inside the polariser. The other valves (V8 bypass, V7 and V4) in the gas handling system are used for polariser maintenance and setup when the system is not in operation.

#### Optical pumping cell

The "central unit" of the polarizer is the optical pumping cell (OPC) Figure (3.4). The cylindrical OPC is a 75 - mm - long borosilicate glass cylinder with 25 mm

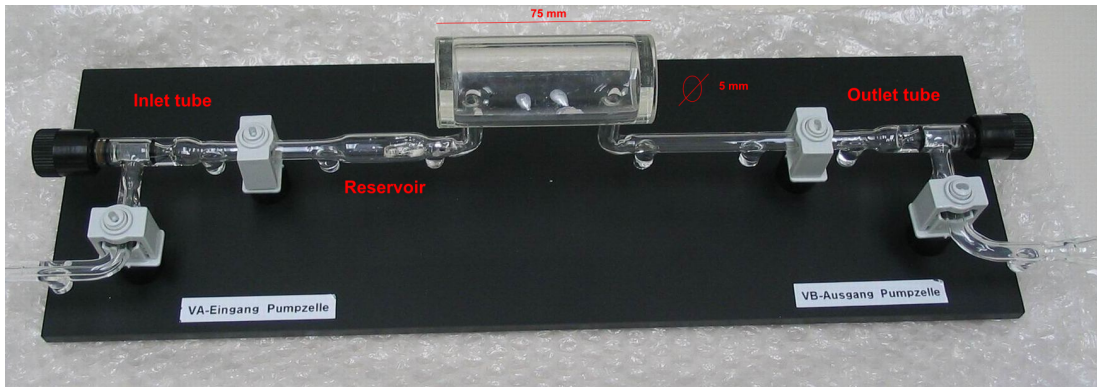


Figure 3.4: Optical Pumping cell.

diameter, resulting in a volume of 36.82 ml. The borosilicate glass is about 5 mm thick and it was tested for high pressure operating condition up to 10 bar. The inlet and outlet of the OPC consists of 6 - mm - outer diameter borosilicate tubes. The inlet arm has a 4 cm long expanded region, the reservoir, to accommodate a small quantity (approximately 1 g) of Rb metal. The reservoir is heated up by an heating gun; using a PID temperature controller the temperature can be regulated in a range between room temperature and 200 °C. However, during our measurements we found that the measured degree of hyperpolarisation of the  $^{129}\text{Xe}$  was higher when the Rb was present inside the OPC which is reasonable, despite the unfavourable far away heating point. The OPC is housed in a borosilicate glass oven so that the hot air, produced by the heating gun, surrounds the OPC. Moreover, OPC is located in the center of a pair of Helmholtz coils which produce an uniform weak magnetic field ( $B \approx 1$  mT). Two stable current supplies deliver a current of  $I = 1$  A to the Helmholtz coils in order to produce the magnetic field.

## 3.2 MR equipment

The measurements of the  $^{129}\text{Xe}$  hyperpolarisation have been performed using a 1.5 - T whole - body scanner (Magnetom Avanto Tim System [76 x 32]; Siemens AG, Erlangen), at the MR imaging department of the DKFZ (Deutsches Krebsforschungszentrum, Heidelberg). A superconducting magnet provides the magnetic field,  $B_0 = 1.5$  T, of the MR scanner. In our system the superconducting material is a niobium - titanium (Nb - Ti) alloy embedded in a copper matrix. The copper is required to add mechanical stability, and to provide current stability in the case that the temperature of the Nb - Ti alloy rises above its critical temperature ( $T_c = 10$  K) and superconductivity is lost (quenching process). During operation, the Nb - Ti wire must be cooled below the critical temperature, i.e., the temperature at which the material changes from the normal resistive state to superconductivity. For Nb - Ti alloy, liquid helium, which has a boiling temperature  $T_b = 4.22$  K, is used as a coolant.

The MR scanner is equipped with an RF - integrated coil system, the so-called Tim (Total imaging matrix) system. Tim is based on matrix coil concept, where 76 integrated matrix coil elements and 32 independent RF channels are combined to create one total imaging matrix. The magnet has total length of 150 cm and wide inner bore of 60 cm inner diameter. Concerning the gradient system, the MR scanner used in this work, has a maximum gradient field strength of 45 mT/m with a slew rate of 200 T/m/s and has a field of view (FOV) up to 50 cm.

In our department, the Magnetom Avanto MR scanner is used in daily clinical applications. For experimental measurements with polarised  $^{129}\text{Xe}$  we used an home - built coil. The  $^{129}\text{Xe}$  coil was built and developed by Moritz Berger in 2009, for his diploma thesis experimental work at the DKFZ. This  $^{129}\text{Xe}$  coil is a volume coil with total length of 150 mm and inner diameter of 80 mm, it was originally thought for small - animal applications. The resonance frequency of the coil is set to the  $^{129}\text{Xe}$  Larmor frequency at 1.5 T, i.e.  $\omega_0 = 17.615$  MHz and can be adjusted using an RF sweeper.

The MR scanner is controlled by a software, called *syngo*, developed by Siemens. This software provides an user friendly interface to set the parameters of the measurement protocol. For our measurements, we used self - programmed pulse sequences. We created two sequences, one FID sequence to evaluate  $^{129}\text{Xe}$  hyperpolarisation and a FLASH sequence for MRI applications. The sequences have been created using the development environment, provided by Siemens, called IDEA based on C++ programming language.

## 3. MATERIALS AND METHODS

---

### 3.3 Maintenance and setup of the OPC

As described in theory Section (2.3), rubidium is an extremely reactive metal; it ignites spontaneously in the presence of air and interacts violently with oxidizers, halogens and halogenated hydrocarbons, and water. For this reason, rubidium has to be handled with care and all experimental procedures involving it must be done following safety regulations. In this section, the procedures concerning filling, cleaning, and setup of the OPC are described.

#### 3.3.1 Filling procedure

The filling procedure of the OPC is carried out in a nonreactive atmosphere with the use of a buffer gas. The rubidium (1 g - Rb 99.75% metal basis, Alfa Aesar GmbH & Co KG, Karlsruhe), stored in a glass ampoule under argon atmosphere, and the OPC are placed in a vinyl glove box (Coy Laboratory Products Inc., Michigan, USA), where a nonreactive atmosphere of N<sub>2</sub> is established via the inflating/deflating method. The glove box is connected to an N<sub>2</sub> gas bottle, whose output pressure is set to 1.5 bar. The N<sub>2</sub> inflow runs for 24 hours to ensure that the nonreactive atmosphere is established. To prevent any damage, during inflating, the glove box is provided with a pressure relief mechanism. When the inflating procedure is completed, the oxygen/hydrogen content inside the glove box is measured using specific indicators.

When the N<sub>2</sub> atmosphere is established, by means of a glass cutter, the glass ampoule containing the Rb is opened. However, at room temperature, Rb is in a solid state therefore by means of an heating gun it is melted. The Rb in liquid state, is collected with a pipette and introduced into the pumping cell. Once Rb is placed in the OPC reservoir, the inlet and outlet valves are closed to prevent that oxygen could flow in. When the filling procedure is completed, the OPC can be moved from the glove box to the polariser. However, before opening the glove box, all instruments contaminated with Rb are stored in a sealed plastic box to prevent any chemical reaction.

#### 3.3.2 Cleaning and refilling procedures

The rubidium stays in the OPC for about four months. Meanwhile experiments of SEOP can be carried out. Despite all precautionary measures to prevent that oxygen enters the polariser, during that time the Rb inside the OPC is subject to a slow oxydation process. When Rb is mostly oxidised, it cannot be used anymore for optical pumping. Therefore cleaning and refilling procedures are needed. Before the cleaning procedure, the OPC is removed from the polariser and placed in a chemical lab. Here, low and controlled oxygen gas flow is pumped

in the OPC to completely oxidise the Rb. When Rb is fully oxidised, the OPC is washed using an ethanol - distilled water mixture. First, pure ethanol is used to prevent violent chemical reactions of non - oxidised Rb with water, then the amount of water in the cleaning mixture is gradually increased. When the OPC is completely cleaned and dried, a new filling procedure can be started.

### 3.3.3 Setup procedure

After filling, the OPC is placed in the polariser. However, due to reactive properties of Rb, precautionary measures has to be applied to prevent oxygen can flow in the system. In stand - by mode, the OPC is isolated from external atmosphere by closing the inlet/outlet valves and establishing high pressure,  $p = 2$  bar, inside the gas handling system. Before running the operating mode for each measurement, vacuum is generated in the system using a vacuum pump (TSH 071, Pfeiffer GmbH, Asslar). First, a mechanical vacuum pump runs for about 5 min up to  $p_{vacuum} \approx 3 \cdot 10^{-1}$  mbar, then a turbomolecular pump is used to achieve a vacuum of  $p_{vacuum} \approx 3 \cdot 10^{-3}$  mbar. The turbomolecular pump needs a running time of about 20 min to achieve the desired vacuum. When vacuum is established in the system, it is flushed using the gas mixture of He, Xe and N<sub>2</sub>. The evacuating and flushing procedures are repeated twice. They are carried out to get rid of the oxygen from the system, in order to prevent chemical reaction with Rb and because oxygen, due to its paramagnetic properties, has a destructive effect on <sup>129</sup>Xe hyperpolarisation. During evacuating and flushing of the system the inlet/outlet valves of the OPC are closed. After the evacuating and flushing procedures, the stand - by pressure,  $p = 2$  bar, is established in gas handling system and the inlet/outlet valves of the OPC can be carefully opened. When the OPC is connected to the gas handling system, the desired pressure is set and the polariser is ready for operating mode.

## 3.4 Data analysis

After performing experiments on hyperpolarised <sup>129</sup>Xe - gas, in collaboration with M. Schnurr, data analysis has been carried out using Matlab software (Version R2011a, MathWorks Inc., Natick, Massachusetts, USA). The Matlab programs used to evaluate the experimental results can be found in appendix A.

### 3. MATERIALS AND METHODS

---

#### 3.4.1 Evaluation of $^{129}\text{Xe}$ hyperpolarisation

##### Mechanical factor

In this work, measurements has been carried out on a gas mixture of 90.3% helium, 8.75% nitrogen and 0.95% xenon in natural abundances. Due to the low concentration, it was not possible to measure the thermal polarisation of  $^{129}\text{Xe}$ , as reference to evaluate the hyperpolarisation, using the gas mixture. For this reason a glass phantom ( $V_{th} = 470$  ml,  $p_{th} = 1$  bar) filled with 70% of  $^{129}\text{Xe}$  has been used to measure the thermal polarisation. To evaluate correctly the acquired signals using hyperpolarised  $^{129}\text{Xe}$  via SEOP a mechanical factor  $M$  is needed, taking into account the different concentration between the reference and the gas phantom. Under the assumption of xenon being an ideal gas ( $pV = Nk_B T$ ) and using the Dalton's law ( $p_{total} = \sum_{i=1}^n p_i$ ), the mechanical factor  $M$  is given by:

$$M = \frac{N_{th}}{N_{hyp}} = \frac{0.7 p_{th} V_{th} k_B T_{hyp}}{0.264 \cdot 0.0095 p_{hyp} V_{hyp} k_B T_{th}} \approx \frac{0.7 p_{th} V_{th}}{0.002508 p_{hyp} V_{hyp}} \quad (3.1)$$

In the final step it was assumed that  $T_{hyp} = T_{th}$  in the MR scanner. However, the temperature dependence of the chemical shift, Section (2.1.5), of hyperpolarised  $^{129}\text{Xe}$  proves that this assumption is not entirely correct, due to small difference of temperature between the thermally polarized and the hyperpolarized  $^{129}\text{Xe}$ .

Concerning the other numerical values to calculate  $M$ ,  $V_{hyp} = (378.7 \pm 1.3)$  ml and  $p_{hyp}$  ranges between 2 and 7 bar, depending on the experimental setup. We want to remark that  $p_{hyp}$  is given by  $p_{hyp} = p + 1$  bar, where  $p$  is the pressure measured by the manometer of the gas handling system. The factor 0.0095 takes into account the concentration of xenon in the gas mixture, which is only 26.4% of the isotope  $^{129}\text{Xe}$ .

##### Signal intensity

To evaluate the achieved hyperpolarisation of  $^{129}\text{Xe}$ , FID signals were acquired using the  $^{129}\text{Xe}$  - coil described above. The acquired spectra show a peak at the resonance frequency of  $^{129}\text{Xe}$ . To calculate the area under the peak, i.e. the signal intensity, a non commercial Matlab routine was used (PeakFit, version 1.1, TC O'Haver). This Matlab routine additionally performs phase correction and zero - filling, which are standard data processing techniques in NMR signals analysis. Zero filling is processing where zeros are appended to the free induction decay data before Fourier transformation. The effect of zero filling is to increase the digital resolution in the spectrum. There is no new information added to the spectrum. For fit the resonance peak of the acquired signals, a Cauchy - Lorentz distribution has been used. However, due to experimental conditions a broadening of the resonance peaks has been observed. For this reason, to improve

fitting results of the acquired signals, the resonance peaks have been fitted using a sum of two Cauchy - Lorentz distributions. The sum of the two integrals of the distributions is equal to the signal intensity and this value can be used to evaluate the polarisation enhancement via SEOP of  $^{129}\text{Xe}$ , comparing it to the thermal polarisation. The hyperpolarisation of  $^{129}\text{Xe}$  produced via SEOP is given by:

$$P_{Xe} = \frac{\gamma \hbar B_0}{2k_B T_0} \cdot M \cdot \frac{I_{hyp}}{I_{th}} \quad (3.2)$$

Defining  $\varepsilon = M \cdot I_{hyp}/I_{th}$ , Equation (3.2) becomes:

$$P_{Xe} = \varepsilon \cdot \frac{\gamma \hbar B_0}{2k_B T_0} \quad (3.3)$$

where  $\varepsilon$  is the enhancement factor of  $^{129}\text{Xe}$  polarisation via SEOP, relative to its thermal polarisation.



# Chapter 4

## Results

### 4.1 Polarisation of the pumping laser beam

As described in the theoretical background chapter (2.4.1), the spin exchange optical pumping (SEOP) can be explained by a chain of transfer processes whereby angular momentum is transferred from resonant, circularly polarised light to the electronic spins of Rb vapor and is then subsequently transferred to the  $^{129}\text{Xe}$  nuclear spins during collisions. For this reason, to effectively pump the Rb ground state and achieve a high level of  $^{129}\text{Xe}$  polarisation, a fully circularly polarised light is required. The higher is the degree of circular polarisation of the laser beam the higher the  $^{129}\text{Xe}$  hyperpolarisation is.

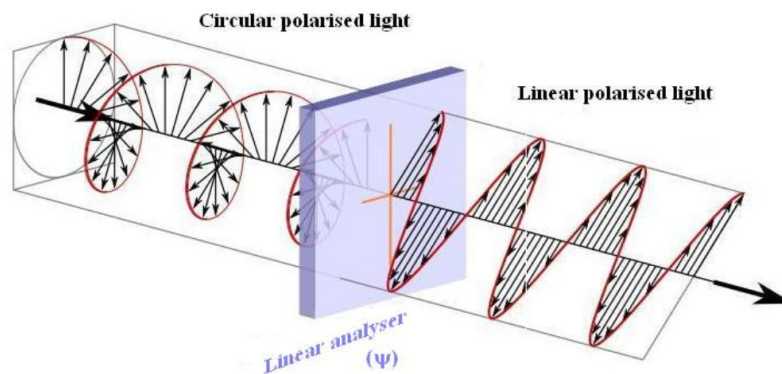


Figure 4.1: Experimental setup for measuring circular polarisation

Serial experiments, aimed to optimise the laser polarisation, have been carried out. In order to evaluate the laser beam polarisation we used a linear filter (analyser), placed after the  $\lambda/4$  - plate of our optical setup (3.2) and the IR -

## 4. RESULTS

---

spectrometer to measure the transmitted light. The two laser beams have been measured separately. The angles of the  $\lambda/4$  - plates, relative to the direction of the linear polarisation of the incident light, were calculated previously by G. Antweiler. The optimal configuration aimed to produce the maximum degree of circular polarisation is:

$$\theta_{left} = (44.8 \pm 0.2)^\circ \text{ and } \theta_{right} = (50.0 \pm 0.2)^\circ \quad (4.1)$$

where  $\theta_{left}$  and  $\theta_{right}$  are referred to the left and the right  $\lambda/4$  - plate, respectively. The relative errors are due to the analyser sensitivity.

According to theory, the transmitted intensity of the laser beam through the analyser is given by:

$$I_{tr} = \frac{E_0^2}{2} \left( \cos 2\theta \cdot \cos 2(\psi - \theta) \right) \quad (4.2)$$

where  $\theta$  and  $\psi$  are the angles of the  $\lambda/4$  - plate and of the linear analyser fast axis, respectively. If the laser beam is perfectly circularly polarised ( $\sigma^+ = 100\%$ ), rotation of  $\theta$  will not affect the measured transmitted intensity.

The percentage of polarisation is given by  $P = (I_{min}/I_{max}) \cdot 100$  and has been evaluated measuring the transmitted intensity at different  $\theta$ , from  $0^\circ$  to  $360^\circ$ , and fitting results using Equation (4.2). Our results showed that the circular polarisation of the left beam is better than that of the right beam. The values were:  $\sigma_{left}^+ = 97 \pm 4\%$  and  $\sigma_{right}^+ = 87 \pm 4\%$ .

### 4.2 Laser absorption by Rb vapor

The optical pumping laser reference spectrum is shown in Figure (4.3). Absorption spectra have been measured irradiating the optical pumping cell (OPC), by the pumping laser, and measuring the transmitted intensity using the IR - spectrometer. Our IR - spectrometer resolution is  $\Delta\lambda_{spec} = 0.1$  nm. To evaluate the amount of laser light absorption by Rb, a reference spectrum has been measured at room temperature in the absence of Rb vapor. Reference measurements has been carried out at standard running condition, with maximum laser power (60 W c.w.) and diode temperatures set up to provide maximum intensity at the Rb - D<sub>1</sub> absorption line. For our system optimal diode temperatures for laser tuning are  $T_{diode_1} = 17.8^\circ\text{C}$  and  $T_{diode_2} = 18.8^\circ\text{C}$ . By absorption measurement we evaluated the pumping laser FWHM, and obtained  $\delta\lambda = (1.5 \pm 0.1)$  nm.

In Figure (4.3), an absorption spectrum of Rb vapor at the temperature of  $40^\circ\text{C}$  is also plotted. It shows absorption in the OPC, filled with Rb vapor, at  $\lambda = (794.7 \pm 0.1)$  nm, in agreement with the theoretical value of the Rb - D<sub>1</sub>

## 4.2. Laser absorption by Rb vapor

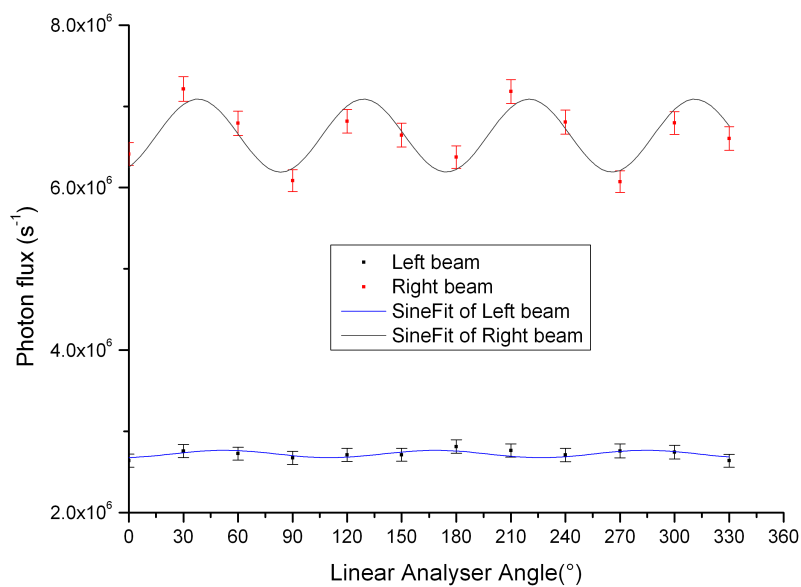


Figure 4.2: Results of pumping laser circular polarisation measurements

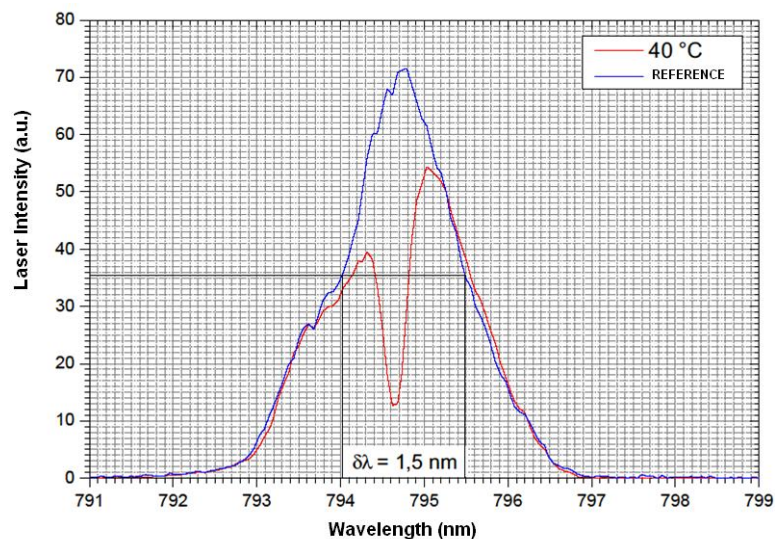


Figure 4.3: Laser absorption reference spectrum (blue line) and absorption by Rb vapor at the temperature of  $40^\circ \text{C}$  (red line). Measurement parameters were  $F = 100 \text{ ml/min}$ , the gas flow through the OPC, and  $p = 1 \text{ bar}$ , the total pressure in the system.

## 4. RESULTS

---

absorption line ( $\lambda_{D_1} = 794.76$  nm). The percentage of the incoming light which is absorbed has been calculated, giving:

$$A = 1 - \frac{Int_{40C}}{Int_{ref}} = 19.5\% \quad (4.3)$$

where  $Int_{40C}$  and  $Int_{ref}$  are the integrals under the curves.

### 4.2.1 Temperature dependence

Serial experiments, aimed to evaluate the temperature dependence of laser absorption by Rb vapor, have been carried out by varying the Rb temperature in the range of 40°C - 200°C. Resulting absorption spectra at different temperatures are plotted in Figure (4.4). Experimental data have been collected at different temperature stepped by ( $\Delta T = 10^\circ$  C). During measurements about temperature dependence others macroscopic parameters, gas flow through the OPC and total pressure, were kept constant ( $F = 100$  ml/min and  $p = 1$  bar).

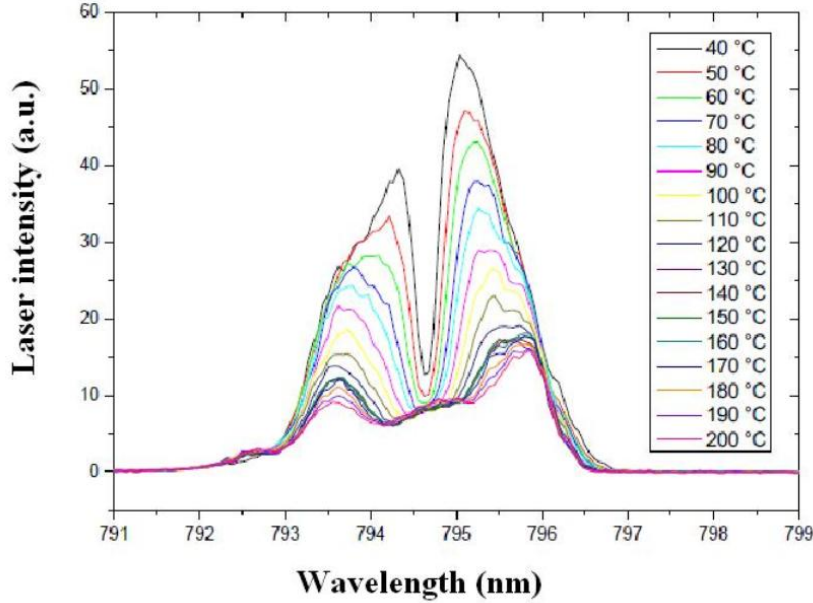


Figure 4.4: Spectra of laser absorption by Rb vapor at different Rb temperatures. Measurement parameters were,  $F = 100$  ml/min, the gas flow through the OPC, and  $p = 1$  bar, the total pressure in the system.

Our results show that higher laser absorption by Rb vapor arises is obtained by increasing the temperature up to 130° C. Beyond that value a saturation effect

was observed up to 200° C. It is remarkable how the spectrum profile changes at high temperatures. It widens significantly probably due to a shielding effect of Rb vapor, related to the increasing of Rb number density inside the OPC when the temperature increases.

### 4.2.2 Pressure broadening of the D<sub>1</sub> - absorption line

A technical challenge for optical pumping is the efficient utilization of the diode laser spectral output. One way to permit the Rb vapor to absorb light is to collisionally broaden the D<sub>1</sub> line absorption profile using a suitable high pressure buffer gas. Using the IR - spectrometer we measured the transmitted light through the OPC, to assess the broadening of Rb D<sub>1</sub> absorption line by varying the buffer gas pressure in the range of 1 bar - 6 bar. Each spectrum has been collected at steady - state, after 25 - min irradiation time with continuous laser power of 60 W c.w. to avoid the laser heating effect. Others macroscopic parameters were  $F = 100$  ml/min and  $T_{Rb} = 70^\circ$  C. Experimental results are shown in Figure (4.5).

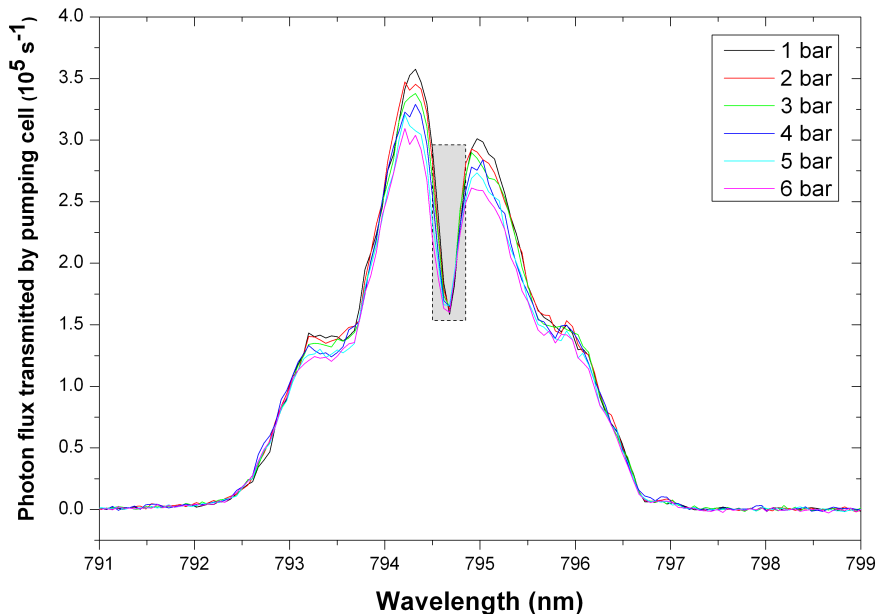


*Figure 4.5: Spectra of laser absorption by Rb vapor at varying buffer gas pressure. Measurement parameters were  $F = 100$  ml/min, the gas flow through the OPC, and  $T_{Rb} = 70^\circ$  C, Rb temperature.*

Figure (4.6) shows details of the dips about the Rb absorption line, highlighting the pressure broadening of the Rb D<sub>1</sub> line. Moreover, in Figure (4.7)

## 4. RESULTS

---

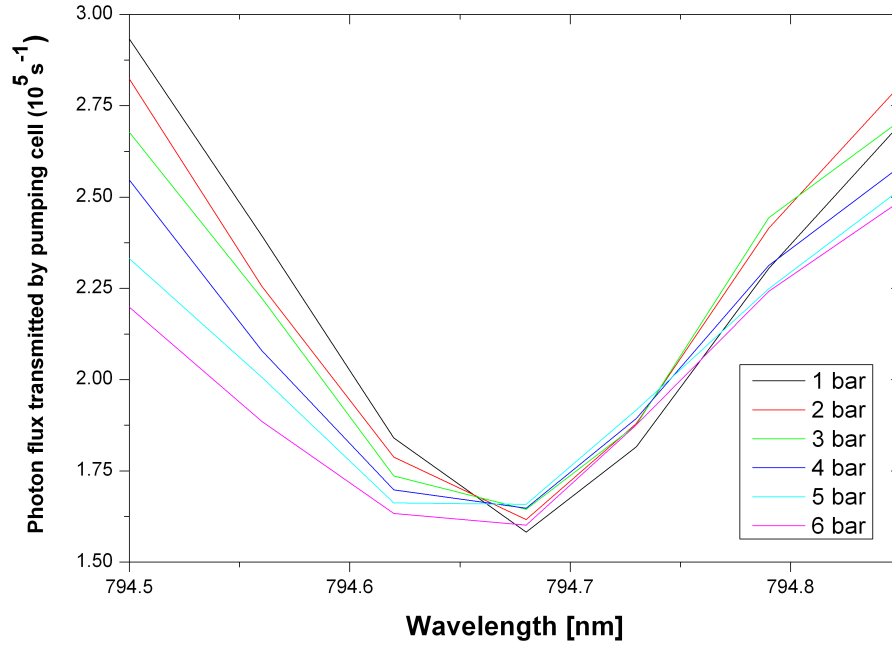


Figure 4.6: Detail of the absorption spectra about Rb  $D_1$  at different pressures.

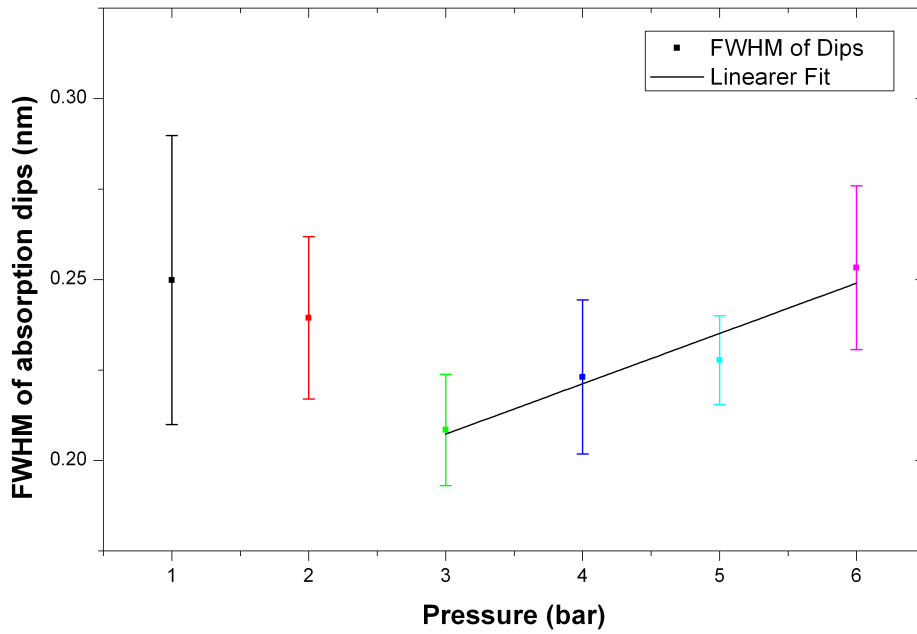


Figure 4.7: Rb  $D_1$  absorption line broadening versus pressure.

### 4.3. Thermal polarisation of $^{129}\text{Xe}$

---

the linewidth of the absorption dips versus buffer gas pressure are plotted. The FWHM of each absorption spectrum has been evaluated by fitting experimental data with a Gaussian function. The large error bars in Figure (4.7) are due to the IR - spectrometer resolution,  $\Delta\lambda_{spec} = 0.1$  nm, and to the small number of experimental data about the Rb absorption line.

By linear fit of experimental data of the Rb  $D_1$  absorption line broadening as a function of pressure, we obtained a slope of:

$$s = (0.01391 \pm 0.00277) \text{ nm/bar} \quad (4.4)$$

leading to a pressure broadening of:

$$\frac{\delta\nu}{p} = (6.60 \pm 1.32) \text{ GHz/bar} \quad (4.5)$$

### 4.3 Thermal polarisation of $^{129}\text{Xe}$

Signal produced by thermally polarised  $^{129}\text{Xe}$  has been measured as reference to evaluate the achieved hyperpolarisation by SEOP, see Section (3.4.1). The reference measurement has been carried out by placing a glass phantom, containing a gas mixture of  $^{129}\text{Xe}$  and  $\text{O}_2$ , for 5 hours in the MR scanner and afterwards collecting FID signal. Long measurement time was needed due to long spin - lattice relaxation of  $^{129}\text{Xe}$  magnetisation and  $\text{O}_2$  was added to decrease  $T_1$  time.

The signal intensity produced by thermally polarised  $^{129}\text{Xe}$  has been calculated by fitting experimental data and evaluating the integral under the resonance using an own Matlab program, see appendix (A.1). Our result is:

$$I_{th} = 5.19 \pm 0.05 \cdot 10^6 \quad (4.6)$$

This value has been used for data analysis in Equation (3.2).

### 4.4 Hyperpolarisation of $^{129}\text{Xe}$

Production of hyperpolarised  $^{129}\text{Xe}$  gas depends on many thermodynamical parameters, which are correlated. In our work we investigated how some of these macroscopic parameters can influence the achieved degree of hyperpolarisation by SEOP between Rb and  $^{129}\text{Xe}$ . In particular, using the setup described in chapter 3 (Materials and Methods), we studied how macroscopic parameters like Rb temperature, buffer gas pressure, and gas mixture flow (6 l/h - 30 l/h), can affect the measured degree of  $^{129}\text{Xe}$  hyperpolarisation.

In Figure (4.8) an overview of the achieved  $^{129}\text{Xe}$  hyperpolarisation is shown as a function of above cited thermodynamical parameters. Before each measurement

## 4. RESULTS

---

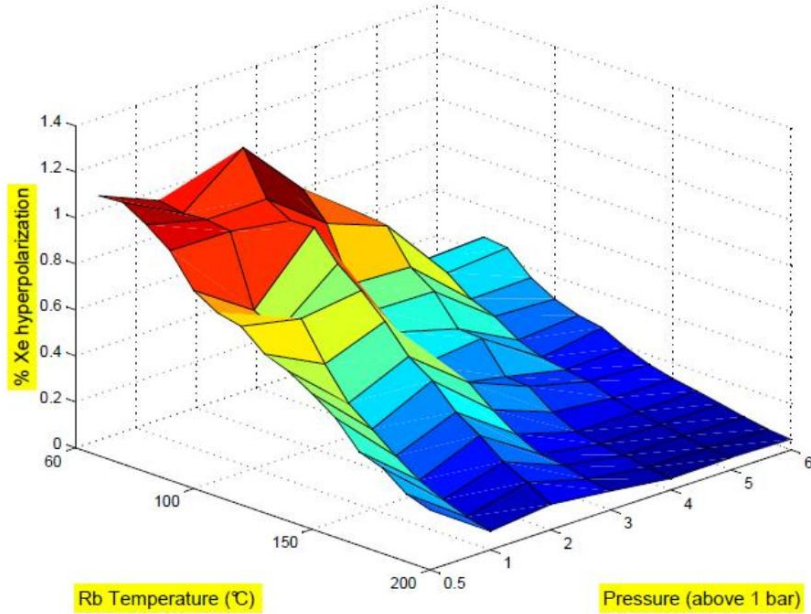


Figure 4.8: Hyperpolarisation of  $^{129}\text{Xe}$  as a function of temperature, pressure and gas flow. Measurement parameters:  $T_{\text{Rb}} = 60^\circ\text{C}$  to  $200^\circ\text{C}$ ,  $p = 0.5$  bar to 6 bar and  $F = 100$  ml/min to 500 ml/min.

session, the HPD was set up to the desired pressure, the Rb was heated up to  $60^\circ\text{C}$  and the OPC was irradiated at maximum laser power for half an hour to reach steady - state. Afterwards, serial experiments were performed increasing temperature up to  $200^\circ\text{C}$ , stepped by  $10^\circ\text{C}$ ; for each Rb temperature, gas flow was varied between 100 ml/min and 500 ml/min, stepped by 100 ml/min. Total measurement time for each session was about 3 hours. Because for each session the last set Rb temperature was  $200^\circ\text{C}$ , the HPD was cooled overnight before another measurement session was started.

In the following sections, our results concerning the individual influence of the thermodynamical parameters on the production of hyperpolarised  $^{129}\text{Xe}$  is presented.

### 4.4.1 Influence of Rb temperature

First we consider the external temperature which is controlled by the heating unit surrounding the OPC. It directly determines the amount of rubidium vapor within the OPC and the convection pattern. Our results, Figure (4.9), show that the mean  $^{129}\text{Xe}$  spin polarisation throughout the OPC slightly increases with the external temperature up to a maximum value. At further increasing

#### 4.4. Hyperpolarisation of $^{129}\text{Xe}$

temperatures, the  $^{129}\text{Xe}$  polarisation decays exponentially.

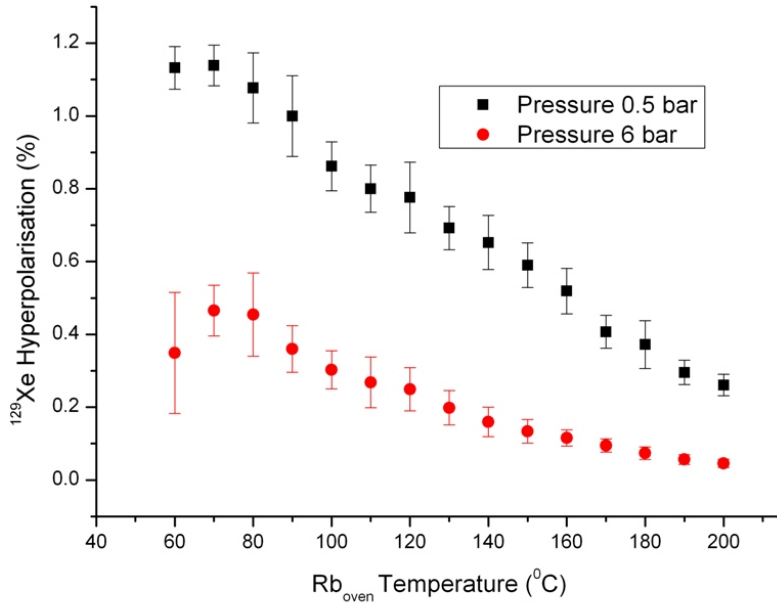


Figure 4.9: Hyperpolarisation of  $^{129}\text{Xe}$  as a function of Rb temperature at different buffer gas pressures (0.5 bar and 6 bar).

Values of hyperpolarisation plotted in Figure (4.9) are lower than values in Figure (4.8), because the mean value from different gas flows has been considered. Only two data sets, referred to different system pressures, are plotted. Other data sets show the same dependence on Rb temperature and appear between maximum (0.5 bar) and minimum (6 bar) values. The error bars are the standard deviations related to the mean values from different gas flows.

It is remarkable that the initial increase of  $^{129}\text{Xe}$  spin polarisation with temperature is by no means trivial, as the rubidium density, and therefore also the rubidium - xenon spin exchange rate, increases with temperature according to the exponential function given by Equation (2.62). At a critical rubidium density, a substantial part of the laser power is absorbed in the front part of the OPC, causing rubidium and hence xenon spin polarisations to drop down in the other regions of the OPC.

## 4. RESULTS

---

### 4.4.2 Influence of pressure

Another important parameter for production of hyperpolarised  $^{129}\text{Xe}$  is the gas pressure. Indeed Equation (2.65) states that the rubidium spin destruction rate increases with increasing gas pressure. In agreement with theoretical predictions, our results show that with increasing pressure the degree of  $^{129}\text{Xe}$  polarisation decreases exponentially. Figure (4.10a) shows the degree of  $^{129}\text{Xe}$  polarisation as a function of total gas pressure and xenon partial pressure, for four different Rb temperature (60°C, 100°C, 150°C, 200°C). As described in Section (4.4.1), the mean value of hyperpolarisation from different gas flows has been considered. Other data sets show the same dependence on total gas pressure and appear in Figure (4.10a) between maximum (60°C) and minimum (200°C) values.

For the applications, however, the crucial parameter is the enhancement of the signal intensity produced by polarised  $^{129}\text{Xe}$ , which is determined by the product of xenon density and degree of polarisation. Our measurements show an approximately  $\sim \sinh$  dependence on xenon partial pressure and the optimum value for our experiment corresponds to about 0.2 bar; see Figure (4.10b).

### 4.4.3 Influence of gas flow

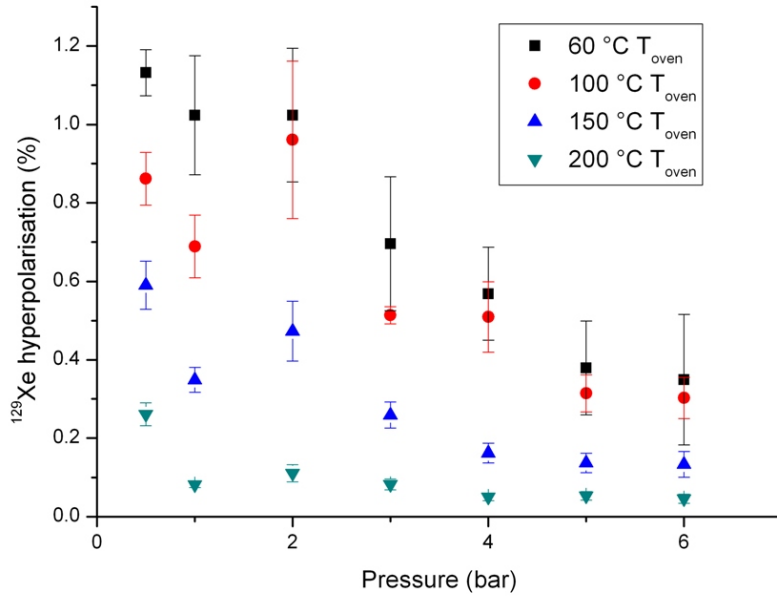
The third macroscopic parameter that plays an important role in the production of hyperpolarised  $^{129}\text{Xe}$  and has been studied in this work is the gas flow rate through the OPC. Figure (4.11) shows the achieved hyperpolarisation of  $^{129}\text{Xe}$  as a function of the gas flow rate at different Rb temperatures. The measured values for other Rb temperatures are not shown in order to make the figure more clear. It is remarkable that, despite the temperature dependence of the achieved degree of  $^{129}\text{Xe}$  hyperpolarisation, looking at the flow dependence our results show the same regime at different temperatures, with a minimum for 200 ml/min and a maximum for 500 ml/min of flow rate.

### 4.4.4 Maximum enhancement of $^{129}\text{Xe}$ polarisation

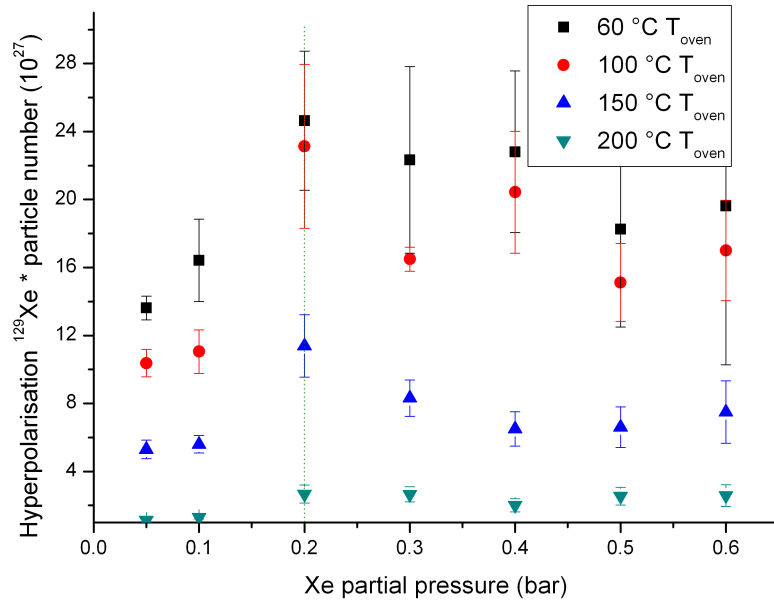
The maximum achieved degree of  $^{129}\text{Xe}$  hyperpolarisation which has been measured was  $P_{Xe} = 1.29\%$ , with measurement parameters  $T_{Rb} = 90^\circ\text{C}$ ,  $P = 2$  bar and  $F = 500$  ml/min. The integral of the recorded FID signal was  $I_{hyp} = (2.51 \pm 0.04) \cdot 10^9$ . At 2 bar the mechanical factor is  $M = 116.29$ . By substitution of these values in Equation (3.2) and taking into account the reference value, Equation (4.6) the maximum experimentally achieved enhancement factor of  $^{129}\text{Xe}$  hyperpolarisation via SEOP was:

$$\epsilon = 5.6196 \pm 0.0986 \cdot 10^4 \quad (4.7)$$

#### 4.4. Hyperpolarisation of $^{129}\text{Xe}$



(a)



(b)

Figure 4.10: (a) Hyperpolarisation of  $^{129}\text{Xe}$  as a function of total gas pressure at different Rb temperatures. (b) Dependence of the product of the  $^{129}\text{Xe}$  polarisation and density of number of particles on the xenon partial pressure.

## 4. RESULTS

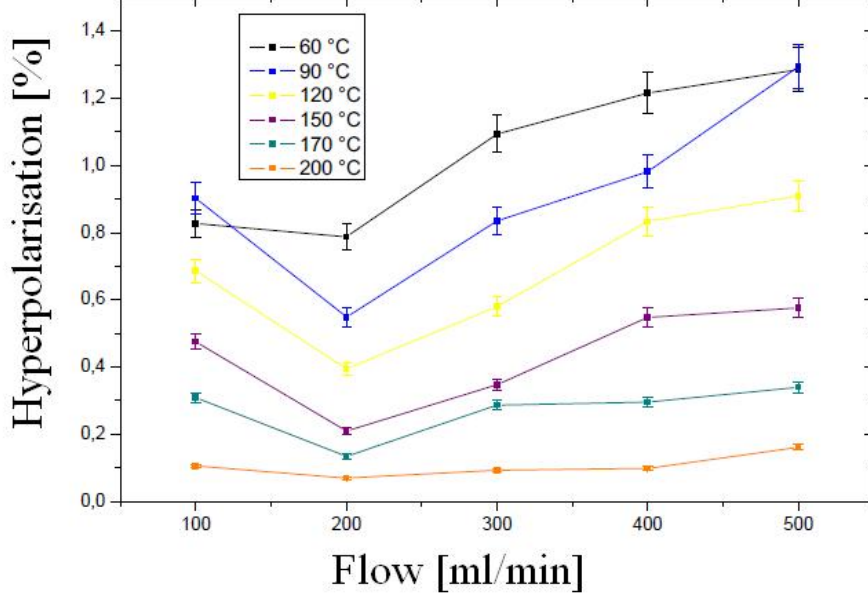


Figure 4.11: Hyperpolarisation of  $^{129}\text{Xe}$  as a function of the gas flow rate at different Rb temperatures ( $60^\circ\text{C}$ ,  $90^\circ\text{C}$ ,  $120^\circ\text{C}$ ,  $150^\circ\text{C}$ ,  $170^\circ\text{C}$ ,  $200^\circ\text{C}$ ).

### 4.5 Laser - Heating effect

In the first step of the SEOP process, a circularly polarized  $D_1$  photon is absorbed by the ground state Rb - atom. In order to suppress emission by the excited state atom,  $\text{N}_2$  buffer gas is added to the gas mixture to relax a large fraction of the excited alkali atoms via radiationless, two - body quenching collisions. The consequence is that the optical energy absorbed by the alkali vapor is converted almost completely into heat [Walter et al., 2001]. This is the laser heating effect (LHE).

To evaluate the LHE we investigated the time evolution of  $^{129}\text{Xe}$  hyperpolarisation when the pumping laser is switched on, monitoring the temperature measured in the OPC. Figure (4.12) shows the results of an experiment with  $T_{\text{Rb}} = 140^\circ\text{C}$ ,  $p_{\text{tot}} = 6$  bar and  $F = 400$  ml/min. At time  $t_{\text{pump}} = 0$ , the pumping laser is switched on with maximum power of continuous 60 W c.w. The results show that the measured temperature of the OPC rapidly rises up to a maximum at pumping time  $t_{\text{pump}} \approx 20$  min. Afterwards the system is at thermal equilibrium. The measured  $^{129}\text{Xe}$  hyperpolarisation shows, in agreement with theoretical predictions, an hyperbolic profile. Hyperpolarisation is characterised by a non - exponential growth up to a maximum at  $t_{\text{pump}} \approx 5$  min, and is then followed by an exponential decay towards a non - zero equilibrium value. The 3 - min time

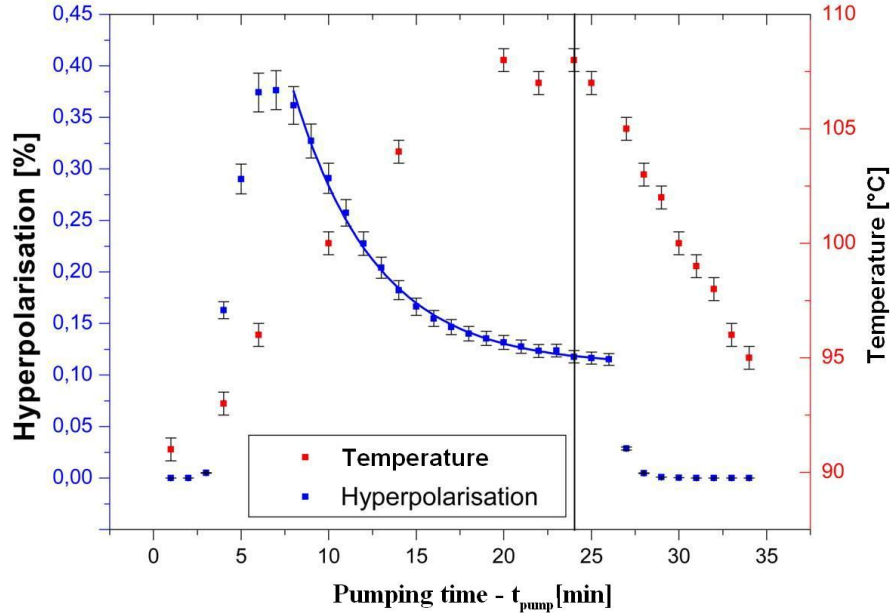


Figure 4.12: Time - dependent evolution of the  $^{129}\text{Xe}$  hyperpolarisation in the OPC under flowing conditions. Measurement parameters:  $T_{\text{Rb}} = 140^\circ\text{C}$ ,  $p_{\text{tot}} = 6$  bar and  $F = 400$  ml/min. The measured OPC temperature is also plotted.

delay between switching on of the pumping laser and the first measured signal from hyperpolarised  $^{129}\text{Xe}$ , is due to the gas delivery time between the HPD and the MR scanner. The same time delay can be observed after switching off the pumping laser: the signal produced by hyperpolarised  $^{129}\text{Xe}$  takes about 3 min to disappear.

In Figure (4.13), the laser absorption spectra of Rb vapor at different optical pumping times are shown. It is remarkable how the LHE affects the absorption profile of the pumping laser light by the Rb atoms. The total absorption increases as optical pumping time increases, leading to an OPC temperature rise described above. After about 17 min of optical pumping, the system is in thermal equilibrium and the absorption profile does not change significantly upon further pumping the Rb vapor.

A possible explanation is that at high Rb vapor densities and at high laser power, a Rb layer which has a local number density much higher than in the bulk is building up on the cell walls. This layer absorbs a significant fraction of the pumping laser light on the front window, leading to a reduction of the volume - averaged Rb polarisation and subsequently of the  $^{129}\text{Xe}$  hyperpolarisation.

## 4. RESULTS

---

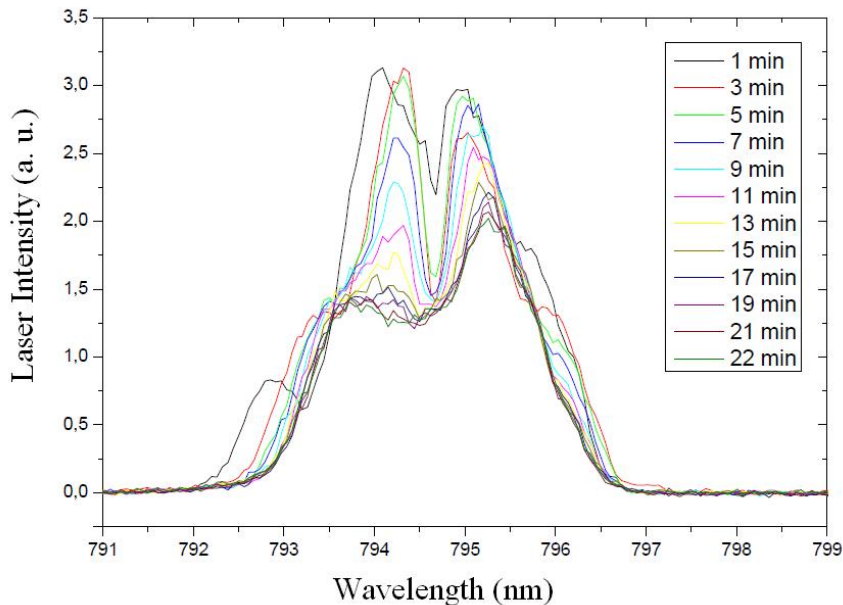


Figure 4.13: Evolution of measured laser absorption spectra by Rb vapor as a function of optical pumping time. Measurement parameters:  $T_{Rb} = 70^{\circ}C$ ,  $p_{tot} = 1$  bar and  $F = 100$  ml/min.

### 4.6 Relaxation in PU tubes

As described in Section (3.1.3), in our system the hyperpolarized  $^{129}\text{Xe}$  gas is delivered to the MR scanner by a PU tube. For this reason we measured the loss of signal along the above cited connection tube. In serial measurements we acquired the  $^{129}\text{Xe}$  FID signal for different tubes length while keeping constant all other parameters. In Figure (4.14) the achieved  $^{129}\text{Xe}$  hyperpolarisation as a function of delivery tube length is shown. By linear fit of experimental data we obtained a linear slope of  $(-0.014 \pm 0.07)$  %/m. Therefore a relatively small relaxation of hyperpolarised  $^{129}\text{Xe}$  in PU tubes has been observed.

### 4.7 Dependence of xenon gas chemical shift on temperature

As previously described, see Section (2.1.5), when an atomic or molecular species with non zero nuclear spin is subject to an external magnetic field  $B_0$  the local field seen by the nucleus is affected by its chemical environment according to Equation (2.54). For a monoatomic gas no temperature dependence of chemical

## 4.7. Dependence of xenon gas chemical shift on temperature

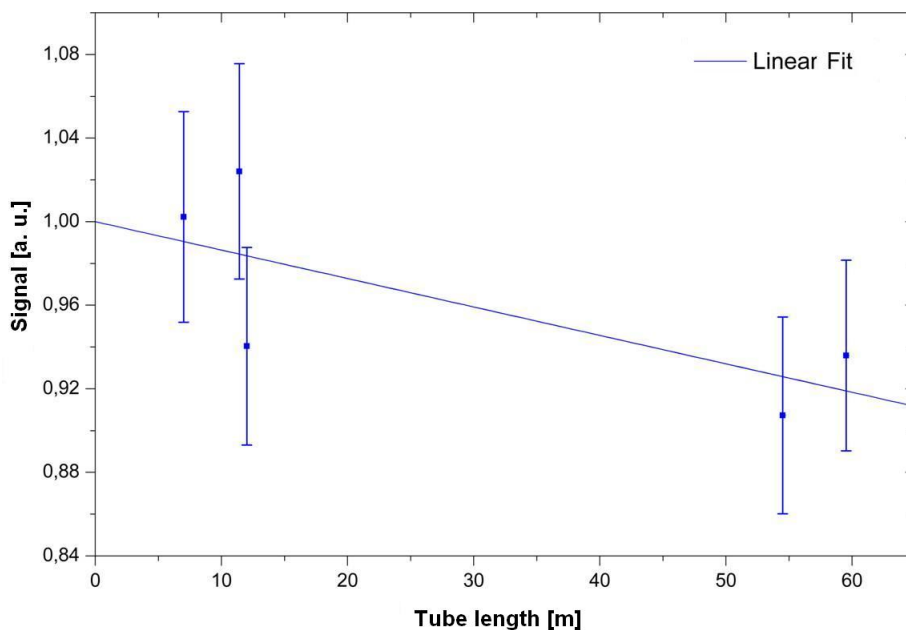


Figure 4.14: Signal versus PU connection tube length. Measurements parameters:  $T_{Rb} = 90^\circ C$ ,  $p_{tot} = 0.5$  bar and  $F = 300$  ml/min.

shift is expected in first order. However, this effect is observed and attributed to van der Waals interacting Xe - Xe molecules.

Following [Jameson et al., 1973], the nuclear chemical shift tensor of xenon gas can be described, as a function of temperature and gas density, by a virial expansion:

$$\sigma\left(T, [Xe_{gas}]\right) = \sigma_0(T) + \sigma_1(T)[Xe_{gas}] + \sigma_2(T)[Xe_{gas}]^2 \quad (4.8)$$

For Xenon gas the first virial coefficient  $\sigma_0(T)$  is constant and is set to zero, while the second virial coefficient can be approximated by:

$$\sigma_1(T) = \alpha_1 + \alpha_2 \cdot e^{-E_A/kT} \quad (4.9)$$

The first term can be interpreted as the temperature - independent chemical shift which originates from long - range Xe - Xe interactions. The second one represents the temperature - dependent contribution due to short - range contact Xe - Xe.

To evaluate the temperature dependence of xenon gas chemical shift, serial measurements have been carried out keeping constant the buffer gas pressure (0.5 bar) and flow (300 ml/min). The temperature dependence has been measured

## 4. RESULTS

---

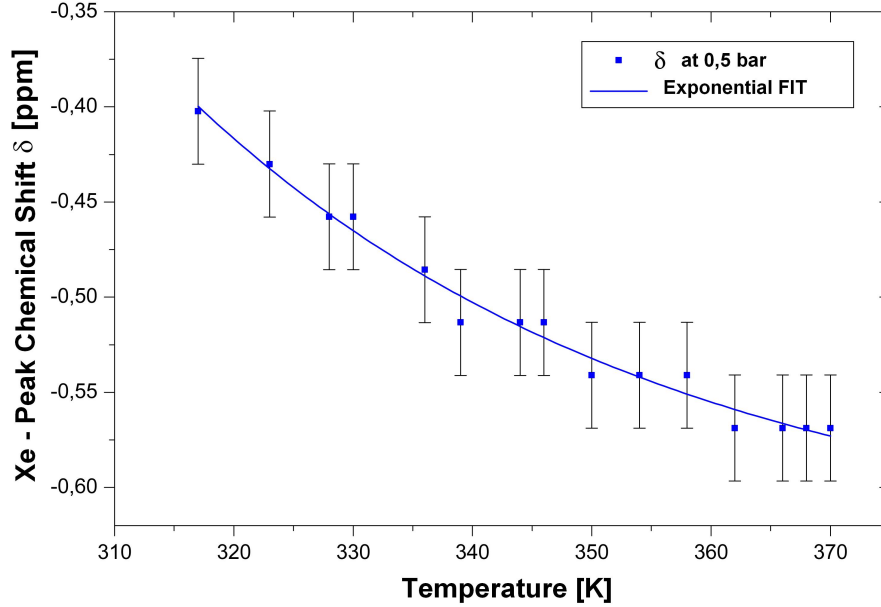


Figure 4.15: Xenon gas chemical shift as a function of temperature. Measurement parameters:  $T_{Rb} = 60 - 200^\circ C$  ( $\Delta t = 10^\circ C$ ),  $p_{tot} = 0.5$  bar and  $F = 300$  ml/min.

at Rb temperature ranging from  $60^\circ C$  to  $200^\circ C$ , stepped by  $10^\circ C$ . For each measurement settings an FID with  $90^\circ$  pulse was recorded and analysed. The resonance frequency of thermally polarised Xe was used as reference to evaluate the chemical shift,  $\nu_{ref} = 17.61555$  MHz, and the error bars are due to the MR scanner sensitivity. Our results qualitatively agree with theory, and demonstrate an exponential temperature dependence of the xenon gas chemical shift even if they are quantitatively different. This is a crucial measurement for applications like in - vivo spectroscopy. Results are plotted in Figure (4.15).

# Chapter 5

## Discussion

### Polarisation of the optical pumping laser beam

The two laser beams used in the Xe polariser of the DKFZ for optical pumping of Rb vapor have different quality of circular polarisation. The left beam shows a nearly perfect circular polarisation,  $\sigma_{left}^+ = 97 \pm 4\%$ . The right beam has circular polarisation of  $\sigma_{right}^+ = 87 \pm 4\%$ , 10% lower than that of the left beam, resulting in a poor quality of total circular polarisation of the optical pumping laser at the window of the pumping cell. The low quality of circular polarisation can be attributed to imperfections of the mirror, used for deflecting of the laser beam, and / or the  $\lambda/4$  - plate on the right beam path. The quality of the Glan - Thompson prism has been evaluated by inserting a second beam splitter with optical axes rotated by  $90^\circ$  with respect to the first. From these measurements we estimated a nearly perfect linear polarisation of the two beams transmitted by the Glan - Thompson prism. Considering the mirror as a passive element, the quality of circular polarisation could be improved by replacing the  $\lambda/4$  plates. However, looking at the production rate of hyperpolarised xenon, the benefits arising from replacing the  $\lambda/4$  plates are negligible due to the poor quality of the pumping laser profile (large bandwidth,  $\delta\lambda = (1.5 \pm 0.1)$  nm). For this reason, the replacement of the  $\lambda/4$  plates should be one of the last optimisation steps.

### Laser absorption by Rb vapor

The main source of angular momentum for the experiments presented in this work was the fiber - coupled beam - optimised broad laser. The optical pumping laser is capable to output typically 60 W c.w. of broad - spectrum uniform beam, with a spectrum characterized by  $\delta\lambda = (1.5 \pm 0.1)$  nm FWHM. However, only 20% of the incoming light is absorbed through the optical pumping cell (OPC). This means that at the window of the OPC a maximum laser power of 12 W c.w. is available

## 5. DISCUSSION

---

for optical pumping of the Rb vapor. So in order to improve the achieved  $^{129}\text{Xe}$  hyperpolarisation we are focusing on: (i) increasing the laser power, changing laser source; (ii) narrowing the laser bandwidth, using an external cavity.

It has been demonstrated that appropriately designed external cavities feedback can be used to lock the laser and force it into a narrow emission [Levron et al., 1998; Zenger et al., 2000]. In [Nelson et al., 2000], coupling a laser diode array (LDA) to an external cavity, the bandwidth has been narrowed from 2 nm to 0.1 nm, with a power amplification factor of 8.4. Moreover, narrowing feasibility at high laser power has been shown in [Zhu et al., 2005], where bandwidth of a laser system with power of 297 W has been narrowed from 3 nm to 0.4 with an amplification factor of 7.5. Figure (5.1) shows two different external cavities used in narrowing an LDA output. The principle of an external cavity is that light from each emitter must be collimated, reflected off a diffraction grating at the first-order diffraction angle, and imaged back onto the emitter with high efficiency.

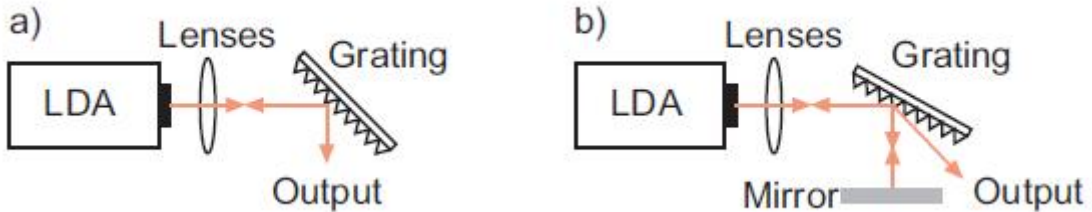


Figure 5.1: External cavities used in LDA frequency narrowing: a) Littrow cavity; b) Littman-Metcalf cavity.

### Temperature dependence

Increased laser absorption by Rb vapor is achieved by increasing the temperature of Rb up to  $130^\circ\text{C}$ . Beyond that value a saturation effect has been observed up to  $200^\circ\text{C}$ . It is remarkable how the spectrum profile changes at high temperatures. Our results show a decrease of transmitted laser power over the entire spectrum. This means that at high temperatures a critical high value of rubidium density is produced in the OPC, thereby laser light no longer can penetrate the whole cell. At oven temperature of  $200^\circ\text{C}$ , a grey vapor, probably Rb vapor, is visible inside the OPC. At this critical rubidium density, a substantial part of the laser power is absorbed in the front part of the OPC, resulting in a reduction of rubidium (and hence xenon) spin polarisation in the other regions of the OPC. Moreover,

---

because optical pumping of Rb vapor is coupled to the laser heating effect, at high temperatures the area close to the laser entry window is heated stronger which results in a longitudinal convection pattern, decreasing the spin polarisation. The inhomogenous optical pumping of rubidium vapor is a challenging aspect in the production of hyperpolarised  $^{129}\text{Xe}$  via SEOP. To prevent the above described effects a counterflow system, where gas mixture flows in opposite direction to the laser beam, have been developed and will be described in the next chapter.

### Pressure dependence

Figure (4.6) shows a detail of the dips about the Rb absorption line, highlighting the pressure broadening of the Rb D<sub>1</sub> line. The calculated value of  $\frac{\delta\nu}{p} = (6.60 \pm 1.32)$  GHz/atm for the pressure broadening is not in good agreement with values reported in literature. [Ottinger et al., 1975] and [Romalis et al., 1997] have reported a pressure broadening of the Rb D<sub>1</sub> line of  $\frac{\delta\nu}{p} = (16.6 \pm 3)$  GHz/atm and  $\frac{\delta\nu}{p} = (18 \pm 0.2)$  GHz/atm, respectively. Deviation of our result from previously reported values is possibly related to the small amount of available experimental data. In fact to evaluate the pressure broadening of the Rb D<sub>1</sub> line we performed a linear fit on a dataset consisting of only 4 points. Moreover, the IR spectrometer used for this work has a very poor resolution,  $\delta\nu_{spec} = 47$  GHz, leading to inaccurate measurements. The calculated values of pressure broadening of the Rb D<sub>1</sub> line for pressure values lower than 3 atm are smaller than the IR spectrometer resolution. Therefore we neglected those values and performed our calculation in the range of 3 atm to 6 atm. However, looking at the minimum of the absorption dips, it is remarkable that our results show that with increasing pressure the minimum is slightly shifted to lower wavelengths. This result is, qualitatively, in agreement with absorption minimum displacement described in [Romalis et al., 1997], where a value of  $\frac{\delta\nu}{p} = (4.3 \pm 0, 1)$  GHz/atm was reported. In this work, however, a quantitative estimation of the minimum of the absorption dip was not possible due again to the low resolution of the IR spectrometer.

## Hyperpolarisation of $^{129}\text{Xe}$

### Temperature dependence

In serial experiments performed at constant pressure of the buffer gas, to evaluate the influence of the Rb temperature on the achieved hyperpolarisation of  $^{129}\text{Xe}$  we found maximum values for  $T_{Rb} < 100^\circ$  C. Our experimental results show a maximum of hyperpolarisation of  $^{129}\text{Xe}$  at lower temperatures than predicted in [Fink et al., 2005]. The difference between our results and the above cited numerical simulation might be caused by a difference of the real temperature

## 5. DISCUSSION

---

inside the OPC compared to the measured Rb temperature. Infact, in our setup we measured the temperature at the external window of the OPC, however the laser heating effect plays a very important role and can lead to gas temperatures hundreds of degree above the Rb temperature [Walter et al., 2001]. Nevertheless, our results, in agreement with literature, show a linear regime at low temperatures up to the maximum hyperpolarisation of  $^{129}\text{Xe}$  and an exponential decay when the temperature is further increased.

### Pressure dependence

Our experimental results demonstrate that with increasing buffer gas pressure the degree of  $^{129}\text{Xe}$  polarisation decreases exponentially. These results, in agreement with theoretical predictions, can be explained by the increase of number density of each gas mixture component ( $^4\text{He}$ ,  $^{129}\text{Xe}$  and  $\text{N}_2$ ) and the subsequent increase of the spin destruction rate of Rb polarisation:

$$\gamma_{SD} = \kappa_{\text{Rb}}n_{\text{Rb}} + \kappa_{\text{Xe}}n_{\text{Xe}} + \kappa_{\text{N}_2}n_{\text{N}_2} + \kappa_{\text{He}}n_{\text{He}} + \gamma_{SE} + \gamma_{\text{trap}} \quad (5.1)$$

Finding the optimal value for buffer gas pressure is a challenging aspect of the production of hyperpolarised  $^{129}\text{Xe}$ , because high pressure is required for broadening of the Rb  $\text{D}_1$  absorption line and to make possible the efficient use of the pumping laser. But as described above, increasing pressure results in increasing of the Rb polarisation spin destruction rate.

### Flow rate dependence

In this work we observed a maximum degree of  $^{129}\text{Xe}$  hyperpolarisation achieved for a gas flow rate of 500 ml/min (30 l/h). This shows that our experimental setup allows production of large amounts of hyperpolarised  $^{129}\text{Xe}$ . The average lung volume in healthy adults is 3.1 l in women and 4.6 l in men. Our system provides the required gas volume for lung imaging in about 8 min. Our system has been designed for a maximum gas flow of 500 ml/min, therefore it was not possible to study the effects of higher flow rates. Moreover, our gas flow control unit showed an unstable response at high buffer gas pressure leading to inaccurate measurements at those experimental conditions.

### Maximum degree of $^{129}\text{Xe}$ polarisation

Table (5.1) presents the maximum degrees of  $^{129}\text{Xe}$  polarisation at different buffer gas pressures and the quite optimal experimental conditions of temperature and flow rate for our device. The highest value of hyperpolarisation was achieved at  $p = 2$  bar,  $T = 90^\circ\text{C}$  and  $F = 500$  ml/min and was:

$$P_{\text{Xe}} = (1.29 \pm 0.07)\% \quad (5.2)$$

---

Table 5.1: Maximum degrees of  $^{129}\text{Xe}$  polarisation at different  $p$  and the quite optimal experimental conditions of  $T$  and  $F$  for our device.

| $p$ [bar] | $T$ [ $^{\circ}\text{C}$ ] | $F$ [ml/min] | $P_{\text{Xe}}$ [%] |
|-----------|----------------------------|--------------|---------------------|
| 0.5       | 60                         | 300          | $1.22 \pm 0.06$     |
| 1         | 60                         | 500          | $1.13 \pm 0.05$     |
| 2         | 90                         | 500          | $1.29 \pm 0.07$     |
| 3         | 80                         | 500          | $1.14 \pm 0.06$     |
| 4         | 80                         | 100          | $1.08 \pm 0.05$     |
| 5         | 60                         | 500          | $0.58 \pm 0.03$     |
| 6         | 80                         | 400          | $0.62 \pm 0.03$     |

Table (5.1) shows that maximum degrees of  $^{129}\text{Xe}$  polarisation have been measured at low Rb temperatures. As described above, this can be explained by the laser heating effect. Indeed, the measured Rb temperatures do not reflect the true temperatures inside the OPC. For this reason a quantitative comparison of our results with values reported in literature was not possible. A better estimation of temperature inside the OPC could be achieved by infrared thermometers.

## Laser - heating effect

Figure (4.12) displays the time dependent evolution of the  $^{129}\text{Xe}$  polarisation in the OPC under flowing conditions. It clearly shows how the LHE affects the degree of polarisation. The drop of  $^{129}\text{Xe}$  polarisation has been fitted by an exponential function, this may be explained by reference to Equation (2.62). During optical pumping of Rb vapor the energy is converted almost completely into heat, resulting in an increase of the Rb number density inside the OPC. The LHE results in the decay of the achieved  $^{129}\text{Xe}$  polarisation, the decay factor is about 3. This loss in the production of hyperpolarised  $^{129}\text{Xe}$  could be recovered by employing "batch mode" with short pumping time and accumulation of the produced hyperpolarised  $^{129}\text{Xe}$ . The latter can be achieved freezing out the xenon from the gas mixture by a cold trap during several pumping cycles.

## Relaxation in PU tubes

The loss of  $^{129}\text{Xe}$  hyperpolarisation due to relaxation in PU tubes, during gas delivering from OPC to the MR scanner, has been estimated to  $(-0.014 \pm 0.07)$  %/m. This is a relatively small loss that can be neglected for systems where a high level of  $^{129}\text{Xe}$  hyperpolarisation is achieved. However, for our level of hyperpolarisation, relaxation in the PU tube leads to a loss of about 50% of

## 5. DISCUSSION

---

polarisation. Taking into account the total length of the PU tube connecting the OPC to the scanner gives:

$$1.29\% + 7.5\text{m} \cdot 0.14\%/m = 2.34\% \quad (5.3)$$

This is the correction factor for the maximum degree of  $^{129}\text{Xe}$  polarisation achieved.

### Temperature dependence of xenon gas chemical shift

In qualitative agreement with [Jameson et al., 1973] our results show an exponential dependence of the xenon gas chemical shift on temperature. However, our experimental value is significantly lower than value reported in literature. This discrepancy can possibly be explained by the unknown value of the true temperature inside the gas phantom, during recording of  $^{129}\text{Xe}$  MR spectra. Here, we assumed that the temperature inside the gas phantom at the MR scanner equals the measured temperature at the OPC surface. However, this value is presumably too high, because the gas mixture cools down quickly flowing through the 7.5 m long PU tube from the OPC to the gas phantom. A better estimation of temperature dependence of xenon gas chemical shift could be achieved by placing a thermometer at the gas phantom surface. Nevertheless, this is a crucial measurement for application like in - vivo spectroscopy because it shows the feasibility of frequency shift estimation.

# Chapter 6

## Newly developed HPD

In previous chapters, experimental results on the influence of thermodynamical parameters on the production rate of hyperpolarised  $^{129}\text{Xe}$  via SEOP with alkali metals have been discussed. This knowledge is a prerequisite for optimisation of the apparatus aimed to increase the achievable degree of polarisation of  $^{129}\text{Xe}$  gas. In this chapter concepts concerning new developments of the design and manufacturing of the hyperpolarisation equipment are described.

### 6.1 New HPD concepts

Novel ideas concerning improvements of our HPD resulted from the experience with the device and our experimental results. Xenon polarisers are separated in two main categories: "batch" production mode and continuous flow production mode. As mentioned in the introduction, the purpose of this work is the development of a version of a continuous - flow polariser.

Figure (6.1) displays the theoretical Rb absorption profile at different total pressures of the gas mixture, assuming an average  $D_1$  broadening of 18 GHz/atm. The absorption cross - section is defined in [Larson et al., 1991] and for low pressure can be simplified to a pure Lorentzian:

$$\sigma(\nu) = \sigma_0 \cdot \frac{(\Gamma_{abs})^2}{4(\nu - \nu_0)^2 + (\Gamma_{abs})^2} \quad (6.1)$$

where the peak amplitude,  $\sigma_0$ , and the FWHM,  $\Gamma_{abs}$ , are given by [Wagshul and Chupp, 1994]:

$$\sigma_0 \cdot \Gamma_{abs} = 5.7 \times 10^{-3} \text{ cm}^2 Hz \quad (6.2)$$

It shows the advantage of using high pressure buffer gases, which results in a high optical pumping rate, even for lasers with a broad spectrum like diode lasers. Most of the reported polarisers were build following the Princeton group design

## 6. NEWLY DEVELOPED HPD

---

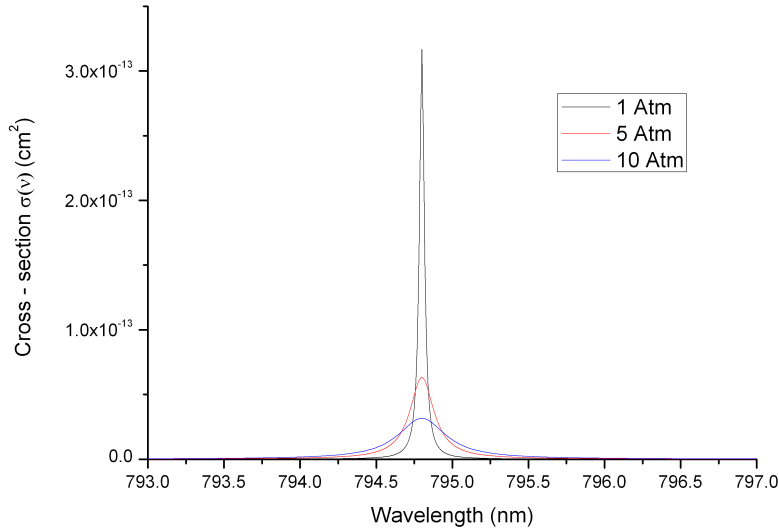


Figure 6.1: Theoretical laser absorption cross section for different total gas pressure of the system assuming an average  $D_1$  line broadening of 18 GHz/atm.

[Driehuys et al., 1996], working at high pressure regimes ( $> 10$  atm) for an efficient absorption of the laser light. The only known exception was reported by [Ruth et al., 1999]: their work involved very low concentration of Xe combined with a very low total pressure of the pumping mixture of only 75 Torr. Their number of 70% is still the largest  $^{129}\text{Xe}$  polarisation reported and was obtained at only 10% Xe concentration in the mixture (the other component was  $\text{N}_2$ ). The polarisation build - up time constant  $\gamma_{SE}$  varied between 7 s and 30 s, depending on temperature, 7 s corresponding to 150° C, the highest temperature used. Although the Xe polarisation was extremely high compared with all other values reported at that time, the production rates were still too low for MRI applications.

In 2001, the group of C. Bowers from the University of Florida built a continuous flow polariser working at moderate pressure in the regime of 2 - 5 atmospheres and using a 210 W laser power, probably the highest laser power ever used in an optical pumping experiment. The system was tested for different operating parameters, [Zook et al., 2002], and they observed increased polarisation values as they reduced the total pressure. We observed just the same in our system. Also, they observed polarisation saturation after a certain flow rate for constant total pressure. Their largest polarisation reported was 67% for low Xe concentrations and at optimum running parameters.

Low xenon concentration in the optical pumping mixture results in high electronic polarisation of Rb and high nuclear Xe polarisation. Another option for a high Rb polarisation is to use very high power diode lasers, resulting in large optical pumping rates. The disadvantage is the low absorption in the "wings" of the laser spectrum at low pressure. One way to enhance the laser absorption is to increase the hot optical pumping region length and volume, such that more Rb atoms are available for laser absorption.

For high spin - exchange rates and low residence times for the pumping mixture (necessary for high flow and production rates) the appropriate choice is to use a low pressure regime. Starting from these basic ideas we improved our system, the arguments are displayed in Figure (6.3).

The main characteristics of our HPD design are:

**Low pressure regime.** Working at low total pressure results in a high spin - exchange rate because of the molecular contribution. It is about five times larger than for high - pressure systems. A higher spin - exchange rate enables a shorter time for the Xe polarisation to reach saturation. The time - constant  $\gamma_{SE}$  at low pressure and 160°C is  $>5$  s. This short spin - exchange time allows higher gas flow rates to be used, resulting finally in higher hyperpolarised xenon production rates.

**"Counterflow" of laser with the gas mixture.** In our system we placed the laser entrance window on the left side of the polariser and the gas input mixture on the right of the OPC. As a consequence, both Rb and Xe start being polarized as they move leftwards towards the exit. We expect the highest Xe polarisation to be achieved at the exit from the optical pumping region. After that, Rb density drops and Rb atoms are trapped on the glass surface. Laser intensity and the optical pumping rate are highest in the cold region, therefore we should expect full Rb polarisation and minimum Xe polarisation loss.

**Long optical pumping region.** A large - volume high - temperature OPC results in a higher absorption of the laser light. By using a large diameter the surface - to - volume ratio is decreased and the Rb and Xe surface interactions are reduced. Nevertheless, an optimum diameter exists. For a too large diameter difficulties arise in shaping the laser beam to uniformly illuminate the whole region. Also, lower flow velocity affects the final Xe polarisation by a long residence time inside the OPC. Small diameter results in a high gas flow velocity, hence there is not enough time to reach steady - state for Xe polarisation.

**Rb pre - saturator** Another concept implemented was to pre - saturate the gas mixture with Rb vapor before entering the optical pumping region.

## 6. NEWLY DEVELOPED HPD

---

By this means higher flow rates of the gas mixture could be used without worrying about saturation by Rb vapor. Therefore, we decided to use a long serpentine shaped glass tube placed before the OPC and outside the region where the laser heating effects occur. A larger amount of Rb metal is loaded in the special - design pre - saturator (see Figure 6.3). The gas mixture is heated up to the oven temperature as it travels rightwards to the optical pumping region, carrying the Rb vapor with it.

Another advantage of the pre - saturator is that by separating the Rb vapor source from the optical pumping region we can eliminate possible runaways of the Rb vapor pressure from its equilibrium value. As mentioned above, measurements of the gas mixture temperature inside optical pumping cells indicated large deviations from the oven temperature [Walter et al., 2001]. Laser absorption could result in high temperature gradients inside the cell and the Rb vapor pressure can not be considered to be in equilibrium with the oven temperature anymore.

Figure (6.2) displays the connections of these new elements of the HPD with their advantages and disadvantages. From the scheme we observe the relationship between different properties of the polariser and how an advantage cancels another disadvantage.

### 6.2 New OPC design

The improvement of our system results mainly from the new design of the optical pumping cell. The cell is a long piece of glass with total length of  $\sim 50$  cm and can be described in terms of three different operational regions: i) rubidium pre - saturation regions (serpentine), ii) laser absorption and polarising region (hot region), iii) rubidium condensing region (cold region). The cell was built by Mr. R. Stadler in the Physikalisches Institut of the University of Heidelberg, this contribution is gratefully acknowledged. The left side,  $\sim 18$  cm long, includes two of the above mentioned regions: the Rb saturation and the polarising region. In order to obtain a large Rb vapor density this part of the polariser needs to be immersed inside of an oven and kept at a high temperature. A large cubic glass oven encloses this part.

The Rb saturator is a serpentine - shaped glass tube connected to the OPC. The serpentine has close to 60 cm in length, 4 loops, and is made from 1.2 cm diameter glass tube. Its purpose is to offer a long path for the entering gas mixture to reach the oven temperature and to saturate the gas mixture with Rb vapor before entering the optical pumping region.

The gas mixture, saturated now with Rb vapor, moves from the serpentine into the optical pumping cell. The OPC is a straight cylinder, 5 cm diameter and 15 cm long. The mixture starts flowing rightwards, against the laser beam

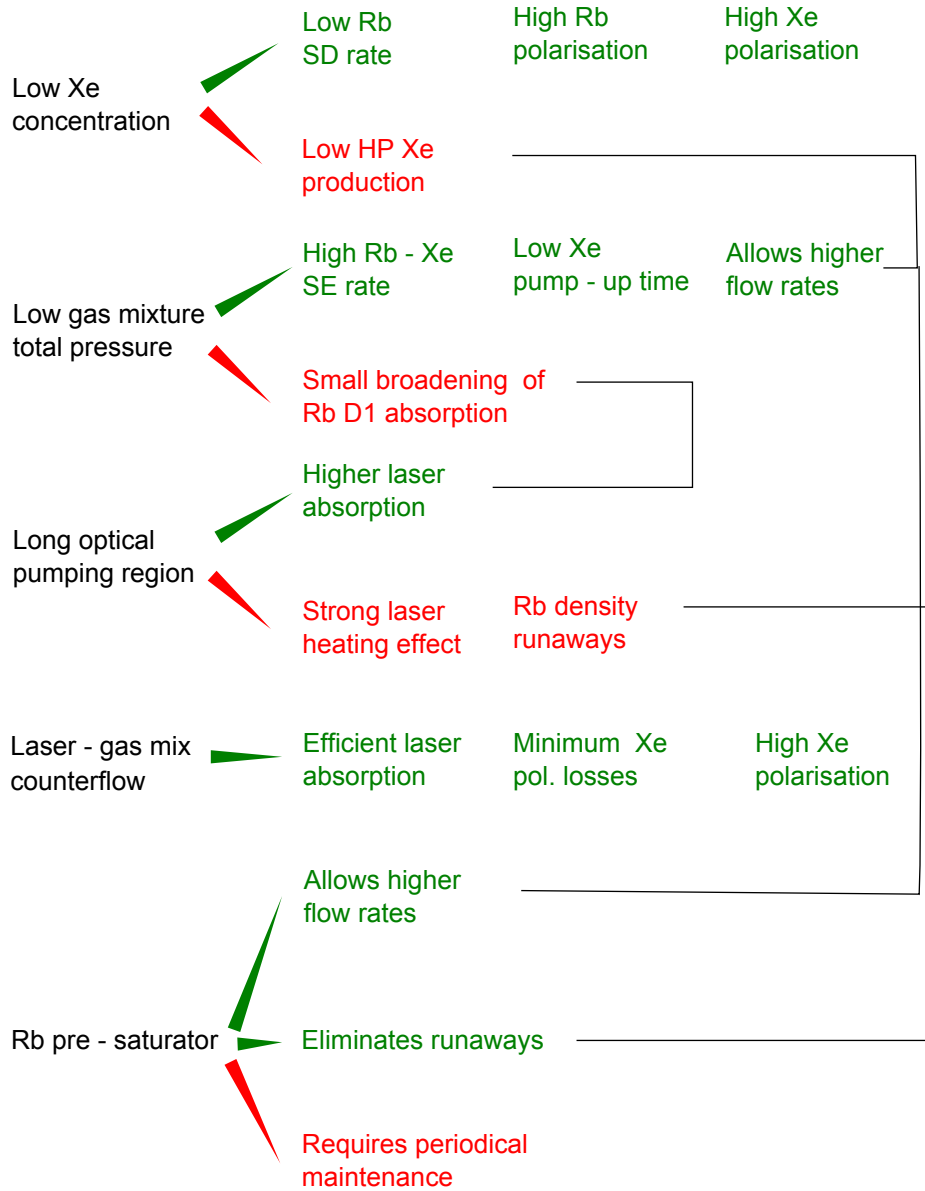


Figure 6.2: HPD polariser logistics showing advantages (green) and disadvantages (red) of our design. Most of the disadvantages are corrected by other implementations in the system. Low xenon production rate required high polarisation output that can be increased because of the low pressure regime and Rb pre-saturator. Rb density runaways from equilibrium in the optical pumping region because the laser heating effect is greatly reduced by the pre-saturator.

## 6. NEWLY DEVELOPED HPD

---



Figure 6.3: New OPC design.

coming from the right top of OPC (counterflowing). The polarisation process begins at the left window of the OPC, with the optical pumping mixture being illuminated with attenuated laser light, and progresses as it moves rightwards the highly illuminated region of the cell. The highest polarisation level is expected to be attained in the first few centimeters of the cold region, where most of the laser light is absorbed.

After, the gas mixture including the hyperpolarised xenon, passing through the cold region, exits the OPC into the down - tube. The down tube is a PU tube and drives the gas mixture from the OPC to the base of the polariser where the freeze - out system for xenon accumulation is located. Finally, the xenon can be frozen and separated from the He and N<sub>2</sub> using the freeze - out system. The freeze - out system and freeze - thaw results will be discussed in detail in the next section.

### 6.3 Accumulation of hyperpolarised <sup>129</sup>Xe

The hyperpolarised <sup>129</sup>Xe is just a small fraction of the high flow low - pressure gas mixture in the optical pumping process. In order to achieve high polarisation degrees N<sub>2</sub> and He are added to the gas mixture as buffer gases. To efficiently use the hyperpolarised <sup>129</sup>Xe one has to separate it from the gas mixture. Typically this is done with a liquid N<sub>2</sub> trap which freezes and separates the <sup>129</sup>Xe from He and N<sub>2</sub>. Figure (2.13) shows the p - T phase diagram of Xenon. At room temperature and atmospheric pressure, it is a gas, but liquefies at moderate temperatures (160 K - 290 K) and pressures (1 bar - 60 bar). At liquid nitrogen temperatures Xe is a solid, which allows the accumulation and storage of laser - polarised xenon applying an external magnetic field.

### 6.3.1 Frozen xenon relaxation mechanism

It is well - known [Cates et al., 1990; Gatzke et al., 1993; Kuzma et al., 2002] that xenon in the frozen state has extremely long spin - lattice relaxation times. For example, at 77 K and moderate magnetic field values solid  $^{129}\text{Xe}$  has a relaxation time of  $>2.5$  hours.  $T_1$  can even reach hundreds of hours at very low temperatures. The mechanisms for spin - lattice relaxation of solid Xe are still under debate. The models assume that there are three temperature regimes with different relaxation mechanisms for the solid state [Kuzma et al., 2002].

For temperatures below 50 K, the nuclear dipole - dipole interaction mediates cross - relaxation between  $^{129}\text{Xe}$  ( $I_\alpha = 1/2$ ) and  $^{131}\text{Xe}$  ( $I_\beta = 3/2$ ):

$$\hat{H}_{DD} = \frac{\mu_0}{4\pi} \cdot \frac{\gamma_\alpha \gamma_\beta \hbar^2}{r_{\alpha\beta}^3} \left( \hat{I}_\alpha \cdot \hat{I}_\beta - 3 \frac{(\hat{I}_\alpha \cdot r_{\alpha\beta})(\hat{I}_\beta \cdot r_{\alpha\beta})}{r_{\alpha\beta}^2} \right) \quad (6.3)$$

For temperatures in the range  $50 \leq T \leq 120$  K, the dominant interaction responsible for relaxation of  $^{129}\text{Xe}$  is the spin - rotation interaction:

$$\hat{H}_{SR} = c_k(r_{\alpha\beta})(\hat{I}_\alpha \cdot \hat{N}_{\alpha\beta}) \quad (6.4)$$

where  $I_\alpha$  is the nuclear spin of  $^{129}\text{Xe}$  and  $N_{\alpha\beta}$  is the angular momentum of the pair formed by the  $^{129}\text{Xe}$  and a second atom separated by the distance  $r_{\alpha\beta}$ . This Hamiltonian also characterises the spin - lattice relaxation mechanisms for the gas and liquid states.

For temperatures above 120 K, the relaxation of  $^{129}\text{Xe}$  is well described by a combination of the spin - rotation interaction (Equation 6.4) and the magnetic dipole - dipole interaction (Equation 6.3), which leads to  $T_1$  values several orders of magnitude smaller than predicted by the spin-rotation interaction alone.

Figure (6.4) shows reported results [Kuzma et al., 2002] on the relaxation mechanisms and the accumulation process of frozen  $^{129}\text{Xe}$ .

### 6.3.2 Xenon accumulation

The relaxation at liquid nitrogen temperature of 77 K is known to be  $>2.5$  hours, a relatively large value. For the transition from and back to the gas state the relaxation depends strongly on temperature and on the holding magnetic field. A major issue in recovering the xenon polarisation from its frozen state is the time spent near the phase transition, where  $T_1$  are in the order of seconds. Despite reported recovery ratios of over 90% for small quantities [Gatzke et al., 1993; Ruth et al., 1999], losses as high as 30 - 50% are routinely observed.

The typical xenon trap is the coaxial double - tube condenser ("cold finger") sketched in Figure (6.5a). The initial gas mixture comes through the inner glass

## 6. NEWLY DEVELOPED HPD

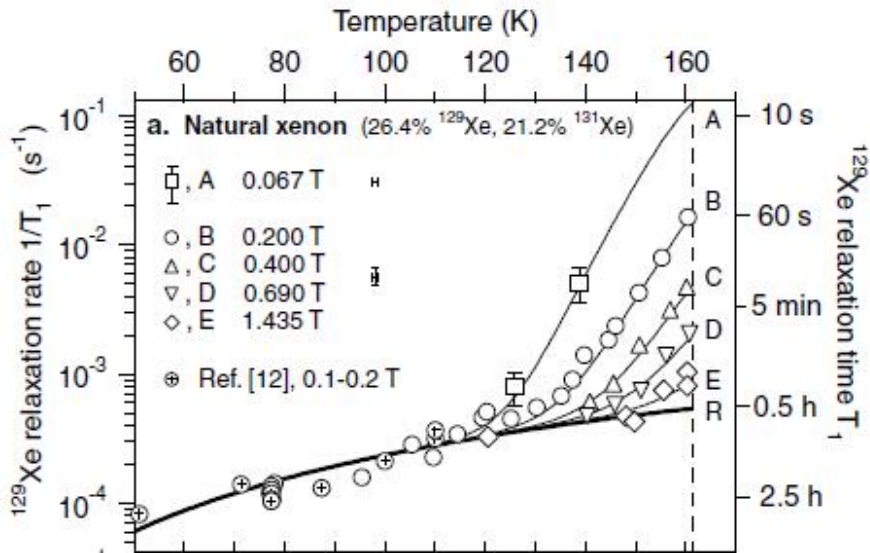


Figure 6.4: Natural abundance xenon relaxation rates in frozen state as a function of temperature and magnetic field. Adapted from [Kuzma et al., 2002].

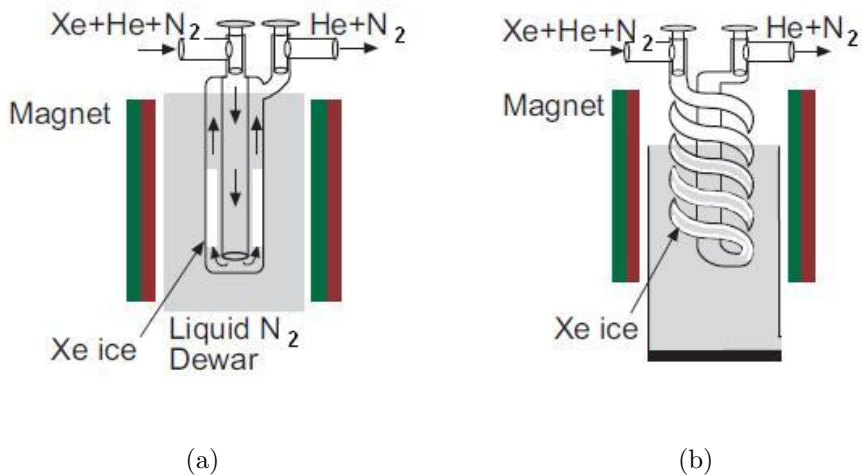


Figure 6.5: (a) Typical design of a "cold finger" or straight tube  $^{129}\text{Xe}$  trap. (b) New design of spiral freeze-out  $^{129}\text{Xe}$  trap.

tube, starts to cool down, and freezes in a thick layer on the outer tube walls. Hypotheses exist for loss mechanisms of polarisation during both accumulation and thawing. During accumulation warm gas mixture passing over already frozen xenon could maintain the top layer of frozen xenon at a higher temperature, particularly for large quantities of frozen xenon. The relaxation time of the inner layers of xenon could be much smaller if its temperature falls into a region where dipole - dipole interaction dominates. [Kuzma et al., 2002] observed that when xenon thawed and passed through liquid phase, it could drop at the bottom of the freeze - out Xe trap and spend long time in the liquid phase, where relaxation times is in the order of seconds.

Starting from these hypotheses we considered a different freeze - out system which would eliminate the fast relaxation mechanisms during phase transitions. The scheme of the implemented freeze - out system is shown in Figure (6.5b). Made from a glass helix tube, the "spiral" freeze - out unit offers a large surface for xenon trapping.

The working principle of our freeze - out system is quite simple. Gas mixture containing hyperpolarized  $^{129}\text{Xe}$  comes from the HPD through the PU connection tube, it enters the freeze - out unit and flows downwards through the spiral partially or fully immersed in the liquid nitrogen dewar. Xenon forms a thin layer of ice distributed over the spiral wall surface with a minimum gradient temperature between the glass surface and the inner layer of frozen xenon. At the end of the accumulation process the xenon snow is uniformly spread inside the spiral in a layer proportional with the quantity of xenon frozen. Thawing this thin uniform layer proceeds quickly when immersed in hot water, such that the relaxation is minimised.

## 6.4 NMR of dissolved $^{129}\text{Xe}$

Hyperpolarised  $^{129}\text{Xe}$  is increasingly applied to *in vivo* MRI, e.g. in lung [Dregely et al., 2011; Driehuys et al., 2012; Imai et al., 2011] and brain imaging [Imai et al., 2012; Mazzanti et al., 2011], as well as for NMR spectroscopy [Boutin et al., 2011; Schroeder, 2011]. The use of hyperpolarised  $^{129}\text{Xe}$  is especially beneficial for lung MRI since conventional proton pulmonary MRI applications are limited by low sensitivity and contrast because of the low proton density and short  $T_2^*$  in the lung. Moreover, hyperpolarised  $^{129}\text{Xe}$  may be of great profit for NMR spectroscopy measurements due to its higher solubility in liquids, e.g. blood [Bifone et al., 1996]. Additionally, as described in the theoretical background chapter, hyperpolarised  $^{129}\text{Xe}$  provides another important advantage: a large chemical shift good for spectroscopy, difference of approx. 200 ppm between dissolved  $^{129}\text{Xe}$  and gaseous  $^{129}\text{Xe}$  can be observed (Figure 2.14).

## 6. NEWLY DEVELOPED HPD

---

However, dissolution of hyperpolarised  $^{129}\text{Xe}$  into blood via inhalation is hindered by the the presence of depolarizing oxygen. This problem can be circumvented by pre - dissolving xenon gas into a suitable carrier liquid and subsequent injection of this free diffusible biomarker. The dissolution of xenon into a solvent is an important feature not only for in vivo MRI, but also for many biological applications, such as the study of biomolecules or protein folding mechanisms. Recently, the main obstacle of efficient and fast dissolution of hyperpolarised  $^{129}\text{Xe}$  without formation of foams or bubbles has been solved by applying a continuous flow system on the basis of commercially available hollow fiber membranes [Amor et al., 2009].

In our system, a commercially available membrane pump (Futur10 T, AL-MATEC Maschinenbau GmbH, Kamp-Lintfort, Germany) has been used and implemented that provides a continuous flow of up to several tens of ml/min of the Xe enriched contrast agent. Its usage will be explored in future experiments.

### Membrane pump

Figure (6.6) shows a schematic drawing of the membrane pump and how it is implemented in the HPD. The hyperpolarised  $^{129}\text{Xe}$  is produced by SEOP using our HPD. Liquid solvent is circulated through the setup including the membrane module driven by a nonmagnetic pump at a rate depending on applied external pressure. Simultaneously, hyperpolarised  $^{129}\text{Xe}$ , produced by SEOP, counterflows through the membranes and dissolves into the liquid. After one passage through the membrane module, the xenon - enriched liquid can be removed and used for further applications.

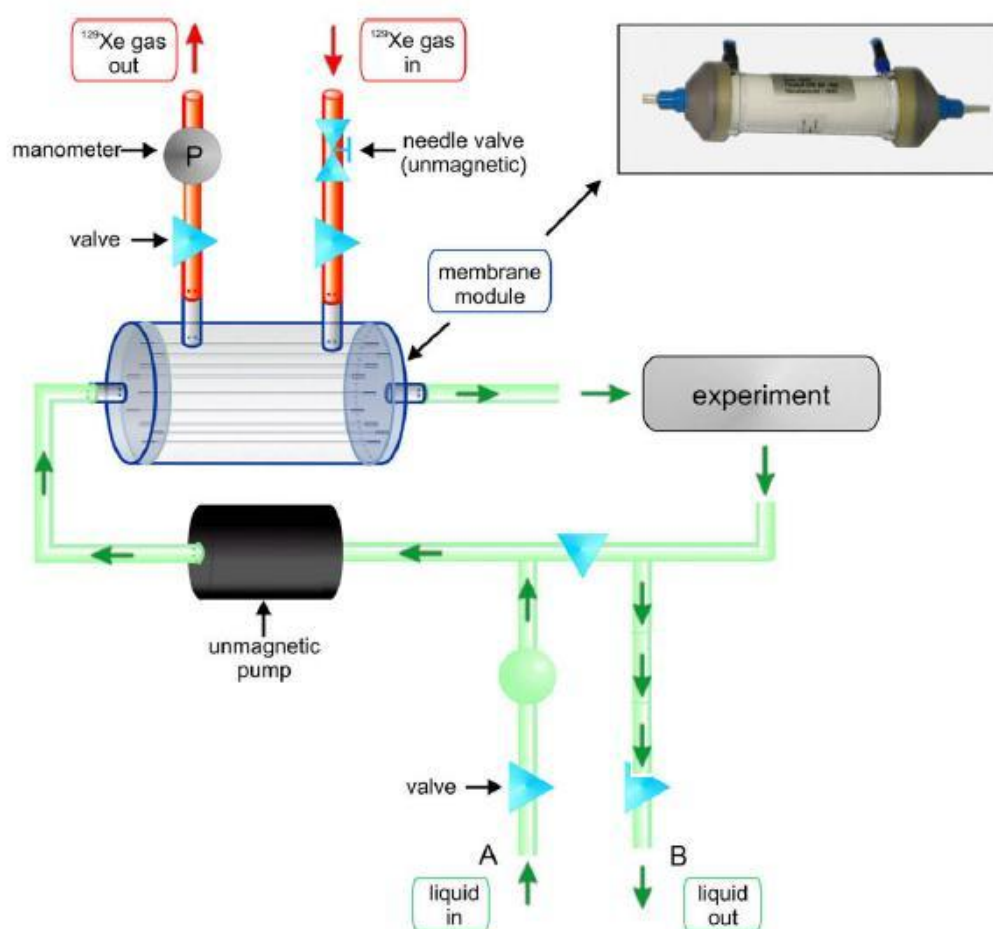


Figure 6.6: Schematic drawing of the membrane pump aimed to hyperpolarised  $^{129}\text{Xe}$  dissolution in liquid solvent. Membrane module photograph on upper right.



# Chapter 7

## Conclusions

In this work we used a continuous flow Rb - Xe polariser to study how the macroscopic thermodynamical parameters can affect the production of hyperpolarised  $^{129}\text{Xe}$  via spin exchange optical pumping (SEOP) of Rb atoms. This knowledge was a prerequisite for design optimisation of an hyperpolarisation device (HPD) for producing large quantities of highly polarised  $^{129}\text{Xe}$ , aimed to perform measurements on  $^{129}\text{Xe}$  gas diffusion and the chemical shift of  $^{129}\text{Xe}$  resonances in vivo. In the following the most relevant results are summarised.

- In serial experiments, varying macroscopic parameters like Rb temperature ( $60^\circ\text{C}$  -  $200^\circ\text{C}$ ), buffer gas pressure (2 atm - 7 atm), and gas mixture flow rate (6 l/h - 30 l/h), we studied the dependence on those thermodynamical parameters of the achieved  $^{129}\text{Xe}$  hyperpolarisation. Our results show maximum values of  $^{129}\text{Xe}$  hyperpolarisation for  $T_{\text{Rb}} < 100^\circ\text{C}$ . At further temperature increasing an exponential decay of  $^{129}\text{Xe}$  hyperpolarisation was observed. The explanation is Rb density, which increases with temperature according to the exponential function given by Equation (2.62). Moreover, an exponential decrease of  $^{129}\text{Xe}$  hyperpolarisation was observed when the buffer gas pressure was enhanced. No flow dependence on the flow rate has been observed.
- At optimal experimental condition the achieved maximum level of  $^{129}\text{Xe}$  hyperpolarisation was 1.29%, measured in the MR scanner, and 2.34% in the optical pumping cell (OPC). This corresponds to an enhancement factor of  $^{129}\text{Xe}$  hyperpolarisation, compared to thermal polarisation, of  $(10.019 \pm 0.0986) \cdot 10^4$ . The achieved  $^{129}\text{Xe}$  hyperpolarisation could be improved by two orders of magnitude: the initial value of polarisation was 0.01% obtained using old system setup.
- The direct relation between the absorbed laser - power by the Rb atoms

## 7. CONCLUSIONS

---

and the hyperpolarisation, the laser - heating effect and the dependence of  $^{129}\text{Xe}$  chemical shift on temperature could be experimentally observed.

- The main characteristics of our improved HPD design are: (i) low pressure regime, for higher production rates of hyperpolarised Xe; (ii) Rb pre - saturator; (iii) "counterflow" of laser and gas mixture; (iv) extended optical pumping region; the purpose of the last two features was to counteract the laser - heating effect.
- We implemented a freeze - out system for accumulation of hyperpolarised  $^{129}\text{Xe}$  and to efficiently separate xenon from gas mixture. We used a spiral - shaped glass tube immersed in a dewar filled with  $\text{N}_2$ . Due to xenon physical properties, the spiral freeze - out trap offers many advantages compared to the typical design of a "cold finger" (straight tube).
- We implemented a membrane pump for efficient and fast dissolution of hyperpolarised  $^{129}\text{Xe}$  in liquid solvents. Liquid solvent is circulated up to several tens of ml/min through the setup including the membrane module driven by a nonmagnetic pump at a rate depending on applied external pressure. Simultaneously, hyperpolarised  $^{129}\text{Xe}$ , produced by SEOP using our HPD, counterflows through the membranes and dissolves into the liquid. Xe - enriched contrast agent and their use for NMR applications will be explored in future experiments.

# Appendix A

## Matlab programs

The experimental data have been acquired using a 1.5 - T whole - body tomograph (Magnetom Avanto Tim System [76 x 32]; Siemens AG, Erlangen). The raw data format file is DICOM (Digital Imaging and Communications in Medicine), which is a standard for handling, storing, printing, and transmitting information in medical applications. To evaluate the experimental results the Matlab software was used: first the DICOM file was read and converted in a Matlab format, then the achieved degree of hyperpolarisation of  $^{129}\text{Xe}$  was calculated. M. Schnurr wrote a program to analyse the data collected with the IR - spectrometer.

### A.1 Reading and evaluating raw data

#### A.1.1 Main program

```
%-----  
% Read Spectroscopy Data from Dicom Files  
% Save each spec series in a different file  
% Francesco Borgosano 08.11.10  
%-----  
cd(uigetdir)  
listoffiles = dir('*.ima');
```

## A. MATLAB PROGRAMS

---

```
numfiles = size(listoffiles,1);

% Variables declaration and index initialization

XeMeasNEW = struct;
FID = struct('pressure',0,'temperature',0,'flow',0,'data',0);
FFT = struct('pressure',0,'temperature',0,'flow',0,'data',0);
Pxe = struct('pressure',0,'temperature',0,'flow',0,'data',0);

% Cycle to create Matlab variables containing raw data exported
% from dicom files

for k = 1:numfiles

    file = listoffiles(k).name;
    fh = dicom_open(file);
    info = dicominfo(file);
    fid = dicom_get_spectrum_siemens(fh);
    FID = setfield (FID,'data',fid(:));

    % Function to perform: phase correction,zero filling and FFT
    % see help 'nmrft'

    result = nmrft(fid,1024,'f');

    %A = real(result);
    %B = imag(result);
    %result = B+(A*i);
    result = flipud(result);
```

## A.1. Reading and evaluating raw data

---

```
FFT = setfield (FFT, 'data', result(:));

XeMeasNEW.fid(k) = FID;
XeMeasNEW.fft(k) = FFT;

end

% Defining different fields associated to the data set (Pressure,
% temperature, flow)

for k = 1:numfiles

    XeMeasNEW.fid(1,k).pressure = 1;
    XeMeasNEW.fft(1,k).pressure = 1;
    XeMeasNEW.Pxe(1,k).pressure = 1;
    XeMeasNEW.fid(1,k).temperature = T(k);
    XeMeasNEW.fft(1,k).temperature = T(k);
    XeMeasNEW.Pxe(1,k).temperature = T(k);
    XeMeasNEW.fid(1,k).flow = F(k);
    XeMeasNEW.fft(1,k).flow = F(k);
    XeMeasNEW.Pxe(1,k).flow = F(k);

end

for k = 1:numfiles

    % Fitting of Experimental data
    s(:,1) = 1:1024;
    s(:,2) = abs(XeMeasNEW.fft(1,k).data(:,1));
    [FitResults, MeanFitError] = peakfit(s, 512, 100, 2, 2, 0, 40);
```

## A. MATLAB PROGRAMS

---

```
Int = FitResults(1,5)+FitResults(2,5);

% Fit'Standard deviation
DeltaInt = MeanFitError/100;

% constants:
Boltzmann = 1.3807*10^(-23);
Roomtemp = 293;
Bfield = 1.5;
hbar = 1.0547*10^(-34);
gyro = 11.777*10^6;
IntThermal = 5.19*10^6;
DeltaIntThermal = 5138.1;
C = (gyro*hbar*Bfield)/(2*Boltzmann*Roomtemp)*100;

% Mechanical Factor:
M = 0.7*470/(0.002508*(XeMeasNEW.fft(1,k).pressure(1,1)+1)*378.7);

% Error
DeltaM = 0.7/0.002508*(sqrt((470*(XeMeasNEW.fft(1,k).pressure(1,1)+1)*...
0.05/(((XeMeasNEW.fft(1,k).pressure(1,1)+1)^2)*378.7))^2+(2/...
((XeMeasNEW.fft(1,k).pressure(1,1)+1)*378.7))^2+(470*1.3/...
((XeMeasNEW.fft(1,k).pressure(1,1)+1)*378.7^2))^2));

%Hyperpolarisation in %:
XeMeasNEW.Pxe(1,k).data(1,1)=(gyro*hbar*Bfield)/(2*Boltzmann*Roomtemp)*...
Int/IntThermal*100*M;
Pxe1_v(k,1) = real(XeMeasNEW.Pxe(1,k).data);
Pxe1_v(k,2) = C*(sqrt(((Int/IntThermal*DeltaM)^2+(DeltaInt/IntThermal*M)...
^2+(Int/(IntThermal)^2*M*DeltaIntThermal)^2));
```

```
end

% ending commands
fclose(fh);
clear FFT FID info ans;
clear fd fh file k listoffiles oldimgnum name A B fid result;
clear s Int Boltzmann Roomtemp Bfield hbar gyro IntThermal M;;
clear FitResults MeanFitError DeltaInt DeltaIntThermal DeltaM C;
clear Pxe;
```

### A.1.2 Functions

#### DICOM open

```
function fd = dicom_open(strFilename)

%-----
% Gets a file descriptor to a DICOM file and check
% it vaguely for DICOM like properties...
%-----

fd = fopen(strFilename, 'rb');

if -1 == fd
    fprintf(' nFailed to open DICOM file. ');
    return;
end

% loose the header
hdr = fread(fd, 128, 'uchar');
```

## A. MATLAB PROGRAMS

---

```
if strcmp(sprintf('%c', fread(fd, 4, 'schar')), 'DICM')

    % fprintf(' nFile appears to be valid DICOM. ');
else
    fprintf(' nFile does NOT appear to be valid DICOM. ');
    fclose(fd);
    fd = -1;
    return;
end
```

### Read FID data

```
%-----
% A special function to read Siemens' spectroscopy FIDs.
%-----

function complex_fid = dicom_get_spectrum_siemens(fd)
% advance the field to the appropriate place
% in the file
field_length = dicom_move(fd, '7FE1', '1010');
field_size = field_length / 4;

% we can use fread to read data in as floats
[fid, fid_size] = fread(fd, field_size, 'float32', 'ieee-le');

if( fid_size ~= field_size )
    fprintf(' nWarning: field size was %d and %d elements were read.', ...
        field_size, fid_size);
end
```

## A.1. Reading and evaluating raw data

---

```
real_part = zeros(length(fid)/2, 1);
imag_part = real_part;

% sort into two columns or make complex
k = 1;
for n = 1:1:length(fid)
    if mod(n,2)
        real_part(k) = fid(n);
    else
        imag_part(k) = fid(n);
        k = k + 1;
    end
end

complex_fid = real_part - j*imag_part;
```

### DICOM move

```
%-----
% Advance to the point in the file where the target group and
% element are and return the length of the field.
% Originally:
% Greg Reynolds 17-June-2005.
%
% Now with in-sequence data support.
%-----

function length = dicom_move(fd, strGroup, strElement)
```

## A. MATLAB PROGRAMS

---

```
%fprintf(' nSearching for target element (%s, %s)...', strGroup, strElement');

% these are all the VRs that have length 2
VR_short_length = struct('strings', ...
    'AE', 'AS', 'AT', 'CS', 'DA', 'DS', 'DT', ...
    'FL', 'FD', 'IS', 'LO', 'LT', 'OF', 'PN', 'SH', ...
    'SL', 'ST', 'SS', 'TM', 'UI', 'UL', 'US' );

dims = size(VR_short_length);
number_of_short_vrs = dims(2);

% these are all the VRs so that we can establish implicit VRs
% without lots of DICOM knowledge
VRs = struct('strings', ...
    'AE', 'AS', 'AT', 'CS', 'DA', 'DS', 'DT', 'FL', ...
    'FD', 'IS', 'LO', 'LT', 'OB', 'OF', 'OW', 'PN', ...
    'SH', 'SL', 'SQ', 'ST', 'SS', 'TM', 'UI', 'UL', ...
    'UN', 'US', 'UT');

dims = size(VRs);
number_of_vrs = dims(2);

done = 0;

while ~done,

    current_tag = fread(fd, 2, 'uint16', 'l');
    current_vr = fread(fd, 2, 'schar', 'l');

    if feof(fd)
```

## A.1. Reading and evaluating raw data

---

```
done = 1;
length = 0;
fprintf(' nReached end of file without match. ');
break;
else
    strGroupCurrent = sprintf('%X', current_tag(1));
    strElementCurrent = sprintf('%X', current_tag(2));
    strVRCurrent = sprintf('%c', current_vr);

    % first of all, check with this is an implicit VR
    explicit_vr = 0;
    for n = 1:1:number_of_vrs
        if strcmp(VRs(n).strings, strVRCurrent)
            explicit_vr = 1;
            break;
        end
    end

    % it was an implicit VR
    if explicit_vr == 0

        % adjust the file pointer back the two-bytes we tentatively
        % read in as being the VR
        fseek(fd, -2, 'cof');

        % possibly need to read in zero padding here?
        current_length = fread(fd, 1, 'uint32', 'l');

        % if the length is undefined, just drop out and move
        % to next element...
```

## A. MATLAB PROGRAMS

---

```
if ~strcmp(sprintf('%X', current_length), 'FFFFFFF')
    if strcmp(strGroupCurrent, strGroup)
        if strcmp(strElementCurrent, strElement)
            length = current_length;
            done = 1;
            break;
        end
    end
end

if done == 0
    fread(fd, current_length, 'uchar', 'l');
end
end

% it was an explicit VR
else
    size_length = 4;

    % check to see whether it has a short length
    for n = 1:number_of_short_vrs
        if strcmp(VR_short_length(n).strings, strVRCurrent)
            size_length = 2;
        end
    end
end

% note that implicit VRs always have 32-bit length
if size_length == 2
    current_length = fread(fd, 1, 'uint16', 'l');
else
    zeropadding = fread(fd, 2, 'uchar', 'l');
```

## A.1. Reading and evaluating raw data

---

```
        current_length = fread(fd, 1, 'uint32', 'l');
    end

    % now see if this was the field we wanted
    if strcmp(strGroupCurrent, strGroup)
        if strcmp(strElementCurrent, strElement)
            length = current_length;
            done = 1;
            break;
        end
    end

    end

    % some implicit VRs, e.g. an SQ can have undefined
    % length if they have 32-bit length, so if that
    % isn't the case, proceed and read, otherwise just
    % skip to the next element
    if ~strcmp(sprintf('%X', current_length), 'FFFFFFF')

        % it wasn't, so advance pointer
        if done == 0
            fread(fd, current_length, 'uchar', 'l');
        end
    end

    end

    end

    end

    end
```

### A.2 IR - spectrometer data

```
%-----  
% Read in of the data of the IR-Spectrometer  
% Written by Matthias Schnurr  
% Last day modified: 17.11.2011  
%-----  
  
cd(uigetdir)  
listoffiles = dir('*.trt');  
numfiles = size(listoffiles,1);  
AbsLaserHeat=struct;  
  
AbsLaserHeat(1).data = dlmread('LASERHEATINGSPECTRA0001.trt',';', 8, 0);  
AbsLaserHeat(2).data = dlmread('LASERHEATINGSPECTRA0002.trt',';', 8, 0);  
AbsLaserHeat(3).data = dlmread('LASERHEATINGSPECTRA0003.trt',';', 8, 0);  
AbsLaserHeat(4).data = dlmread('LASERHEATINGSPECTRA0004.trt',';', 8, 0);  
AbsLaserHeat(5).data = dlmread('LASERHEATINGSPECTRA0005.trt',';', 8, 0);  
AbsLaserHeat(6).data = dlmread('LASERHEATINGSPECTRA0006.trt',';', 8, 0);  
AbsLaserHeat(7).data = dlmread('LASERHEATINGSPECTRA0007.trt',';', 8, 0);  
AbsLaserHeat(8).data = dlmread('LASERHEATINGSPECTRA0008.trt',';', 8, 0);  
AbsLaserHeat(9).data = dlmread('LASERHEATINGSPECTRA0009.trt',';', 8, 0);  
AbsLaserHeat(10).data = dlmread('LASERHEATINGSPECTRA0010.trt',';', 8, 0);  
AbsLaserHeat(11).data = dlmread('LASERHEATINGSPECTRA0011.trt',';', 8, 0);  
AbsLaserHeat(12).data = dlmread('LASERHEATINGSPECTRA0012.trt',';', 8, 0);  
AbsLaserHeat(13).data = dlmread('LASERHEATINGSPECTRA0013.trt',';', 8, 0);  
AbsLaserHeat(14).data = dlmread('LASERHEATINGSPECTRA0014.trt',';', 8, 0);  
AbsLaserHeat(15).data = dlmread('LASERHEATINGSPECTRA0015.trt',';', 8, 0);  
AbsLaserHeat(16).data = dlmread('LASERHEATINGSPECTRA0016.trt',';', 8, 0);  
AbsLaserHeat(17).data = dlmread('LASERHEATINGSPECTRA0017.trt',';', 8, 0);
```

## A.2. IR - spectrometer data

---

```
AbsLaserHeat(18).data = dlmread('LASERHEATINGSPECTRA0018.trt', ';', 8, 0);
AbsLaserHeat(19).data = dlmread('LASERHEATINGSPECTRA0019.trt', ';', 8, 0);
AbsLaserHeat(20).data = dlmread('LASERHEATINGSPECTRA0020.trt', ';', 8, 0);
AbsLaserHeat(21).data = dlmread('LASERHEATINGSPECTRA0021.trt', ';', 8, 0);
AbsLaserHeat(22).data = dlmread('LASERHEATINGSPECTRA0022.trt', ';', 8, 0);

% Calculation of the integral of the absorption peaks
for k=1:22
    sAbsLaserHeat=[(1:3648)',AbsLaserHeat(k).data(:,2)];
    [FitResults,MeanFitError]=peakfit(sAbsLaserHeat,1264,2000,2,1,0,10);
    % Integral of absorption peak
    IntAbsLaserHeat(k)=FitResults(1,5)+FitResults(2,5)%+FitResults(3,5);
    DeltaIntAbsLaserHeat(k)=MeanFitError/100*IntAbsLaserHeat(k);

end

DeltaIntAbsLaserHeat = DeltaIntAbsLaserHeat'

clear FitResults k listoffiles numfiles sAbsLaserHeat;
```



# Bibliography

- A. Abragam. *The Principles of Nuclear Magnetism*. Clarendon Press, Oxford, 1961. 5
- M. S. Albert, D. Balamore, D. F. Kacher, A. K. Venkatesh, and F. A. Jolesz. Hyperpolarized  $^{129}\text{Xe}$   $T_1$  in oxygenated and deoxygenated blood. *NMR Biomed.*, 13(7):407–414, November 2000. ISSN 1099-1492. URL [http://dx.doi.org/10.1002/1099-1492\(200011\)13:7<407::AID-NBM661>3.0.CO;2-1](http://dx.doi.org/10.1002/1099-1492(200011)13:7<407::AID-NBM661>3.0.CO;2-1). 2
- N. Amor, P.P. Zanker, P. Blumler, F.M. Meise, L.M. Schreiber, A. Scholz, J. Schmiedeskamp, H.W. Spiess, and K. Munnemann. Magnetic resonance imaging of dissolved hyperpolarized  $^{129}\text{Xe}$  using a membrane-based continuous flow system. *Journal of Magnetic Resonance*, 201(1):93–99, November 2009. ISSN 1090-7807. URL <http://www.sciencedirect.com/science/article/pii/S1090780709002353>. 84
- L. W. Anderson, F. M. Pipkin, and J. C. Baird Jr.  $\text{N}^{14}$  -  $\text{N}^{15}$  hyperfine anomaly. *Phys. Rev.*, 116(1):87–98, October 1959. URL <http://link.aps.org/doi/10.1103/PhysRev.116.87>. 36
- S. Appelt, A. Ben-Amar Baranga, C. J. Erickson, M. V. Romalis, A. R. Young, and W. Happer. Theory of spin-exchange optical pumping of  $^3\text{He}$  and  $^{129}\text{Xe}$ . *Phys. Rev. A*, 58(2):1412–1439, August 1998. URL <http://link.aps.org/doi/10.1103/PhysRevA.58.1412>. 30, 33
- J. T. Arnold and M. E. Packard. Variations in absolute chemical shift of nuclear induction signals of hydroxyl groups of methyl and ethyl alcohol. *J. Chem. Phys.*, 19(12):1608–1609, December 1951. URL <http://dx.doi.org/10.1063/1.1748134>. 1

## BIBLIOGRAPHY

---

- A. Bifone, Y.-Q. Song, R. Seydoux, R.E. Taylor, B.M. Goodson, T. Pietrass, T.F. Budinger, G. Navon, and A. Pines. Nmr of laser-polarized xenon in human blood. *Proceedings of the National Academy of Sciences*, 93(23):12932–12936, November 1996. URL <http://www.pnas.org/content/93/23/12932.abstract>. 2, 83
- F. Bloch, W. W. Hansen, and M. Packard. The nuclear induction experiment. *Phys. Rev.*, 70(7-8):474–485, October 1946. URL <http://link.aps.org/doi/10.1103/PhysRev.70.474>. 1
- M. A. Bouchiat, T. R. Carver, and C. M. Varnum. Nuclear polarization in He<sup>3</sup> gas induced by optical pumping and dipolar exchange. *Phys. Rev. Lett.*, 5(8):373–375, October 1960. URL <http://link.aps.org/doi/10.1103/PhysRevLett.5.373>. 30
- M. A. Bouchiat, J. Brossel, and L. C. Pottier. Evidence for Rb-rare-gas molecules from the relaxation of polarized Rb atoms in a rare gas. experimental results. *J. Chem. Phys.*, 56(7):3703–3714, April 1972. URL <http://dx.doi.org/10.1063/1.1677750>. 34
- C. Boutin, H. Desvaux, M. Carriere, F. Leteurtre, N. Jamin, Y. Boulard, and P. Berthault. Hyperpolarized <sup>129</sup>Xe nmr signature of living biological cells. *NMR Biomed.*, 24(10):1264 – 1269, December 2011. ISSN 1099-1492. URL <http://dx.doi.org/10.1002/nbm.1686>. 83
- C. R. Bowers, V. Storhaug, C. E. Webster, J. Bharatam, A. Cottone, R. Gianna, K. Betsey, and B. J. Gaffney. Exploring surfaces and cavities in lipoxygenase and other proteins by hyperpolarized xenon-129 nmr. *J. Am. Chem. Soc.*, 121(40):9370–9377, September 1999. ISSN 0002-7863. URL <http://dx.doi.org/10.1021/ja991443+>. 2
- G. D. Cates, D. R. Benton, M. Gatzke, W. Happer, K. C. Hasson, and N. R. Newbury. Laser production of large nuclear-spin polarization in frozen xenon. *Phys. Rev. Lett.*, 65(20):2591–2594, November 1990. URL <http://link.aps.org/doi/10.1103/PhysRevLett.65.2591>. 81
- G. D. Cates, R. J. Fitzgerald, A. S. Barton, P. Bogorad, M. Gatzke, N. R. Newbury, and B. Saam. Rb-<sup>129</sup>Xe spin-exchange rates due to binary and three-body collisions at high Xe

## BIBLIOGRAPHY

---

- pressures. *Phys. Rev. A*, 45(7):4631–4639, April 1992. URL <http://link.aps.org/doi/10.1103/PhysRevA.45.4631>. 28
- A. Cherubini and A. Bifone. Hyperpolarised xenon in biology. *Progress in Nuclear Magnetic Resonance Spectroscopy*, 42(1-2):1–30, June 2003. ISSN 0079-6565. URL <http://www.sciencedirect.com/science/article/pii/S0079656502000523>. 25, 26
- R. A. de Graaf. *In Vivo NMR Spectroscopy: Principles and Techniques*. Wiley & Sons, 2008. 13
- W. C. Dickinson. Dependence of the  $F^{19}$  nuclear resonance position on chemical compound. *Phys. Rev.*, 77(5):736–737, March 1950. URL <http://link.aps.org/doi/10.1103/PhysRev.77.736.2>. 1
- I. Dregely, J. P. Mugler, I. C. Ruset, T. A. Altes, J. F. Mata, G. W. Miller, J. Ketel, S. Ketel, J. Distelbrink, F.W. Hersman, and K. Ruppert. Hyperpolarized xenon-129 gas-exchange imaging of lung microstructure: First case studies in subjects with obstructive lung disease. *J. Magn. Reson. Imaging*, 33(5):1052–1062, May 2011. ISSN 1522-2586. URL <http://dx.doi.org/10.1002/jmri.22533>. 2, 83
- B. Driehuys, G. D. Cates, E. Miron, K. Sauer, D. K. Walter, and W. Happer. High-volume production of laser-polarized  $^{129}\text{Xe}$ . *Appl. Phys. Lett.*, 69(12):1668–1670, September 1996. URL <http://dx.doi.org/10.1063/1.117022>. 3, 36, 76
- B. Driehuys, S. Martinez-Jimenez, Z. I. Cleveland, G. M. Metz, D. M. Beaver, J. C. Nouls, S. S. Kaushik, R. Firszt, C. Willis, K. T. Kelly, J. Wolber, M. Kraft, and H. P. McAdams. Chronic obstructive pulmonary disease: Safety and tolerability of hyperpolarized  $^{129}\text{Xe}$  mr imaging in healthy volunteers and patients. *Radiology*, 262(1):279–289, January 2012. URL <http://radiology.rsna.org/content/262/1/279.abstract>. 83
- G. Duhamel, P. Choquet, E. Grillon, L. Lamalle, J. Leviel, A. Ziegler, and A. Constantinesco. Xenon-129 mr imaging and spectroscopy of rat brain using arterial delivery of hyperpolarized xenon in a lipid emulsion. *Magn. Reson. Med.*, 46(2):208–212, August 2001. ISSN 1522-2594. URL <http://dx.doi.org/10.1002/mrm.1180>. 2

## BIBLIOGRAPHY

---

- R. R. Ernst and W. A. Anderson. Application of fourier transform spectroscopy to magnetic resonance. *Rev. Sci. Instrum.*, 37(1):93–102, January 1966. URL <http://dx.doi.org/10.1063/1.1719961>. 1
- A. Fink, D. Baumer, and E. Brunner. Production of hyperpolarized xenon in a static pump cell: Numerical simulations and experiments. *Phys. Rev. A*, 72(5):053411–, November 2005. URL <http://link.aps.org/doi/10.1103/PhysRevA.72.053411>. 34, 35, 37, 38, 71
- M. Gatzke, G. D. Cates, B. Driehuys, D. Fox, W. Happer, and B. Saam. Extraordinarily slow nuclear spin relaxation in frozen laser-polarized  $^{129}\text{Xe}$ . *Phys. Rev. Lett.*, 70(5):690–693, February 1993. URL <http://link.aps.org/doi/10.1103/PhysRevLett.70.690>. 25, 81
- W. Gerlach and O. Stern. Der experimentelle nachweis der richtungsquantelung im magnetfeld. *Zeitschrift fur Physik A Hadrons and Nuclei*, 9(1):349–352, December 1922. ISSN 0939-7922. URL <http://dx.doi.org/10.1007/BF01326983>. 1, 5
- E. L. Hahn. Spin echoes. *Phys. Rev.*, 80(4):580–594, November 1950. URL <http://link.aps.org/doi/10.1103/PhysRev.80.580>. 24
- W. Happer. Optical pumping. *Rev. Mod. Phys.*, 44(2):169–249, April 1972. URL <http://link.aps.org/doi/10.1103/RevModPhys.44.169>. 3, 28, 30, 32
- W. Happer, E. Miron, S. Schaefer, D. Schreiber, W. A. van Wijngaarden, and X. Zeng. Polarization of the nuclear spins of noble-gas atoms by spin exchange with optically pumped alkali-metal atoms. *Phys. Rev. A*, 29(6):3092–3110, June 1984. URL <http://link.aps.org/doi/10.1103/PhysRevA.29.3092>. 32
- H. Imai, A. Kimura, Y. Hori, S. Iguchi, T. Kitao, E. Okubo, T. Ito, T. Matsuzaki, and H. Fujiwara. Hyperpolarized  $^{129}\text{Xe}$  lung mri in spontaneously breathing mice with respiratory gated fast imaging and its application to pulmonary functional imaging. *NMR Biomed.*, 24(10):1343–1352, May 2011. ISSN 1099-1492. URL <http://dx.doi.org/10.1002/nbm.1697>. 83
- H. Imai, A. Kimura, K. Akiyama, C. Ota, K. Okimoto, and H. Fujiwara. Development of a fast method for quantitative measurement of hyperpolarized  $^{129}\text{Xe}$  dynamics in mouse brain.

## BIBLIOGRAPHY

---

- NMR Biomed.*, 25(2):210–217, February 2012. ISSN 1099-1492. URL <http://dx.doi.org/10.1002/nbm.1733>. 83
- C. J. Jameson, A. K. Jameson, and S. M. Cohen. Temperature and density dependence of  $^{129}\text{Xe}$  chemical shift in xenon gas. *J. Chem. Phys.*, 59(8):4540–4546, October 1973. URL <http://dx.doi.org/10.1063/1.1680652>. 27, 67, 74
- A. Kastler. Quelques suggestions concernant la production optique et la detection optique d'une inegalite de population des niveaux de quantification spatiale des atomes. application à l'experience de Stern et gerlach et à la resonance magnetique. *J. Phys. Radium*, 11(6):255–265, June 1950. URL <http://dx.doi.org/10.1051/jphysrad:01950001106025500>. 29
- S. S. Kaushik, Z. I. Cleveland, G. P. Cofer, G. Metz, D. Beaver, J. Nouis, M. Kraft, W. Auffermann, J. Wolber, H. P. McAdams, and B. Driehuys. Diffusion-weighted hyperpolarized  $^{129}\text{Xe}$  mri in healthy volunteers and subjects with chronic obstructive pulmonary disease. *Magn. Reson. Med.*, 65(4):1154–1165, April 2011. ISSN 1522-2594. URL <http://dx.doi.org/10.1002/mrm.22697>. 2
- T. J. Killian. Thermionic phenomena caused by vapors of rubidium and potassium. *Phys. Rev.*, 27(5):578–587, May 1926. URL <http://link.aps.org/doi/10.1103/PhysRev.27.578>. 28
- W. D. Knight. Nuclear magnetic resonance shift in metals. *Phys. Rev.*, 76(8):1259–1260, October 1949. URL <http://link.aps.org/doi/10.1103/PhysRev.76.1259.2>. 1
- N. N. Kuzma, B. Patton, K. Raman, and W. Happer. Fast nuclear spin relaxation in hyperpolarized solid  $^{129}\text{Xe}$ . *Phys. Rev. Lett.*, 88(14):147602–, March 2002. URL <http://link.aps.org/doi/10.1103/PhysRevLett.88.147602>. 81, 82, 83
- C. Landon, P. Berthault, F. Vovelle, and H. Desvaux. Magnetization transfer from laser-polarized xenon to protons located in the hydrophobic cavity of the wheat nonspecific lipid transfer protein. *Protein Science*, 10(4):762–770, April 2001. ISSN 1469-896X. URL <http://dx.doi.org/10.1110/ps.47001>. 2

## BIBLIOGRAPHY

---

- B. Larson, O. Hausser, P. P. J. Delheij, D. M. Whittal, and D. Thiessen. Optical pumping of Rb in the presence of high-pressure  $^3\text{He}$  buffer gas. *Phys. Rev. A*, 44(5):3108–3118, September 1991. URL <http://link.aps.org/doi/10.1103/PhysRevA.44.3108>. 75
- P. C. Lauterbur. Image formation by induced local interactions: Examples employing nuclear magnetic resonance. *Nature*, 242(5394):190–191, March 1973. URL <http://dx.doi.org/10.1038/242190a0>. 2
- M. H. Levitt. *Spin Dynamics: Basics of Nuclear Magnetic Resonance*. Wiley & Sons, 2008. 5
- D. Levron, D. K. Walter, S. Appelt, R. J. Fitzgerald, D. Kahn, S. E. Korbly, K. L. Sauer, W. Happer, T. L. Earles, L. J. Mawst, D. Botez, M. Harvey, L. DiMarco, J. C. Connolly, H. E. Moller, X. J. Chen, G. P. Cofer, and G. A. Johnson. Magnetic resonance imaging of hyperpolarized  $^{129}\text{Xe}$  produced by spin exchange with diode-laser pumped Cs. *Appl. Phys. Lett.*, 73(18):2666–2668, November 1998. URL <http://dx.doi.org/10.1063/1.122547>. 70
- T. J. Lowery, S. Garcia, L. Chavez, E. J. Ruiz, T. Wu, T. Brotin, J. Dutasta, D. S. King, P. G. Schultz, A. Pines, and D. E. Wemmer. Optimization of xenon biosensors for detection of protein interactions. *ChemBioChem*, 7(1):65–73, January 2006. ISSN 1439-7633. URL <http://dx.doi.org/10.1002/cbic.200500327>. 2
- P. Mansfield and P. K. Grannell. Nmr 'diffraction' in solids? *Journal of Physics C: Solid State Physics*, 6(22):L422–, November 1973. ISSN 0022-3719. URL <http://stacks.iop.org/0022-3719/6/i=22/a=007>. 2
- M. L. Mazzanti, R. P. Walvick, X. Zhou, Y. Sun, N. Shah, J. Mansour, J. Gereige, and M. S. Albert. Distribution of hyperpolarized xenon in the brain following sensory stimulation: Preliminary mri findings. *PLoS ONE*, 6(7), July 2011. URL <http://dx.doi.org/10.1371/journal.pone.0021607>. 83
- I. A. Nelson, B. Chann, and T. G. Walker. Spin-exchange optical pumping using a frequency-narrowed high power diode laser. *Appl. Phys. Lett.*, 76(11):1356–1358, March 2000. URL <http://dx.doi.org/10.1063/1.126030>. 70

## BIBLIOGRAPHY

---

- A. Oros and N. J. Shah. Hyperpolarized xenon in nmr and mri. *Physics in Medicine and Biology*, 49(20):R105–, October 2004. ISSN 0031-9155. URL <http://stacks.iop.org/0031-9155/49/i=20/a=R01>. 26
- Ch. Ottinger, R. Scheps, G. W. York, and A. Gallagher. Broadening of the Rb resonance lines by the noble gases. *Phys. Rev. A*, 11(6):1815–1828, June 1975. URL <http://link.aps.org/doi/10.1103/PhysRevA.11.1815>. 71
- T. Pietraiss and H. C. Gaede. Optically polarized  $^{129}\text{Xe}$  in nmr spectroscopy. *Adv. Mater.*, 7(10):826–838, October 1995. ISSN 1521-4095. URL <http://dx.doi.org/10.1002/adma.19950071003>. 27
- W. G. Proctor and F. C. Yu. The dependence of a nuclear magnetic resonance frequency upon chemical compound. *Phys. Rev.*, 77(5):717–717, March 1950. URL <http://link.aps.org/doi/10.1103/PhysRev.77.717>. 1
- E. M. Purcell, H. C. Torrey, and R. V. Pound. Resonance absorption by nuclear magnetic moments in a solid. *Phys. Rev.*, 69(1-2):37–38, January 1946. URL <http://link.aps.org/doi/10.1103/PhysRev.69.37>. 1
- I. I. Rabi, J. R. Zacharias, S. Millman, and P. Kusch. A new method of measuring nuclear magnetic moment. *Phys. Rev.*, 53(4):318–318, February 1938. URL <http://link.aps.org/doi/10.1103/PhysRev.53.318>. 1
- M. V. Romalis, E. Miron, and G. D. Cates. Pressure broadening of Rb  $D_1$  and  $D_2$  lines by  $^3\text{He}$ ,  $^4\text{He}$ ,  $\text{N}_2$ , and  $\text{Xe}$ : Line cores and near wings. *Phys. Rev. A*, 56(6):4569–4578, December 1997. URL <http://link.aps.org/doi/10.1103/PhysRevA.56.4569>. 71
- I. C. Ruset, S. Ketel, and F. W. Hersman. Optical pumping system design for large production of hyperpolarized  $^{129}\text{Xe}$ . *Phys. Rev. Lett.*, 96(5):053002–, February 2006. URL <http://link.aps.org/doi/10.1103/PhysRevLett.96.053002>.
- U. Ruth, T. Hof, J. Schmidt, D. Fick, and H.J. Jansch. Production of nitrogen-free, hyperpo-

## BIBLIOGRAPHY

---

- larized  $^{129}\text{Xe}$  gas. *Applied Physics B: Lasers and Optics*, 68(1):93–97, January 1999. ISSN 0946-2171. URL <http://dx.doi.org/10.1007/s003400050592>. 3, 76, 81
- M. Schnurr. *Experimente zum Einfluss thermodynamischer Grossen auf die Spin-Hyperpolarisation von  $^{129}\text{Xe}$* . December 2011.
- L. Schroeder. Xenon for nmr biosensing - inert but alert. *Physica Medica*, (0):–, November 2011. ISSN 1120-1797. URL <http://www.sciencedirect.com/science/article/pii/S1120179711001384>. 2, 83
- L. Schroeder, T. J. Lowery, C. Hilty, D. E. Wemmer, and A. Pines. Molecular imaging using a targeted magnetic resonance hyperpolarized biosensor. *Science*, 314(5798):446–449, October 2006. URL <http://www.sciencemag.org/content/314/5798/446.abstract>. 2
- S. D. Swanson, M. S. Rosen, B. W. Agranoff, K. P. Coulter, R. C. Welsh, and T. E. Chupp. Brain mri with laser-polarized  $^{129}\text{Xe}$ . *Magn. Reson. Med.*, 38(5):695–698, November 1997. ISSN 1522-2594. URL <http://dx.doi.org/10.1002/mrm.1910380503>. 2
- M. E. Wagshul and T. E. Chupp. Laser optical pumping of high-density Rb in polarized  $^3\text{He}$  targets. *Phys. Rev. A*, 49(5):3854–3869, May 1994. URL <http://link.aps.org/doi/10.1103/PhysRevA.49.3854>. 75
- A. Wakai, K. Nakamura, J. Kershaw, and I. Kanno. In vivo mr spectroscopy of hyperpolarized xe-129 in rat brain. *International Congress Series*, 1265(0):139–143, August 2004. ISSN 0531-5131. URL <http://www.sciencedirect.com/science/article/pii/S0531513104009513>. 2
- T. G. Walker and W. Happer. Spin-exchange optical pumping of noble-gas nuclei. *Rev. Mod. Phys.*, 69(2):629–642, April 1997. URL <http://link.aps.org/doi/10.1103/RevModPhys.69.629>. 30
- D. K. Walter, W. M. Griffith, and W. Happer. Energy transport in high-density spin-exchange optical pumping cells. *Phys. Rev. Lett.*, 86(15):3264–3267, April 2001. URL <http://link.aps.org/doi/10.1103/PhysRevLett.86.3264>. 39, 64, 72, 78

## BIBLIOGRAPHY

---

- M. E. Weeks. The discovery of the elements. xiii. some spectroscopic discoveries. *J. Chem. Educ.*, 9(8):1413–, August 1932. ISSN 0021-9584. URL <http://dx.doi.org/10.1021/ed009p1413>. 28
- J. Wolber, A. Cherubini, M. O. Leach, and A. Bifone. Hyperpolarized  $^{129}\text{Xe}$  nmr as a probe for blood oxygenation. *Magn. Reson. Med.*, 43(4):491–496, April 2000. ISSN 1522-2594. URL [http://dx.doi.org/10.1002/\(SICI\)1522-2594\(200004\)43:4<491::AID-MRM1>3.0.CO;2-6](http://dx.doi.org/10.1002/(SICI)1522-2594(200004)43:4<491::AID-MRM1>3.0.CO;2-6). 2
- J. N. Zerger, M. J. Lim, K. P. Coulter, and T. E. Chupp. Polarization of  $^{129}\text{Xe}$  with high power external-cavity laser diode arrays. *Appl. Phys. Lett.*, 76(14):1798–1800, April 2000. URL <http://dx.doi.org/10.1063/1.126169>. 70
- X. Zhou, Y. Sun, M. Mazzanti, N. Henninger, J. Mansour, M. Fisher, and M. Albert. Mri of stroke using hyperpolarized  $^{129}\text{Xe}$ . *NMR Biomed.*, 24(2):170–175, February 2011. ISSN 1099-1492. URL <http://dx.doi.org/10.1002/nbm.1568>. 2
- H. Zhu, I. C. Ruset, and F. W. Hersman. Spectrally narrowed external-cavity high-power stack of laser diode arrays. *Opt. Lett.*, 30(11):1342–1344, June 2005. URL <http://ol.osa.org/abstract.cfm?URI=ol-30-11-1342>. 70
- A. L. Zook, B. B. Adhyaru, and C. R. Bowers. High capacity production of  $\approx 65\%$  spin polarized xenon-129 for nmr spectroscopy and imaging. *Journal of Magnetic Resonance*, 159(2):175–182, December 2002. ISSN 1090-7807. URL <http://www.sciencedirect.com/science/article/pii/S1090780702000307>. 3, 39, 76

# Acknowledgements

This dissertation would not have been possible without the guidance and the help of several individuals (and Institutions) who contributed and extended their valuable assistance in the preparation and completion of this study.

- First and foremost, my utmost gratitude to Prof. Dr. Peter Bachert my PhD advisor for the opportunity to join his research group for this work. With his enthusiasm, his inspiration, and his great efforts to explain things clearly and simply, he helped me to deeply understand fundamental physics of NMR and SEOP. Throughout my thesis - writing period, he provided encouragement, sound advice, good teaching, and lots of good ideas.
- I would like to thank Prof. Dirk Dubbers who undertook to act as my second advisor despite his many other academic and professional commitments.
- This dissertation would not have been possible unless Guido Antweiler, Matthias Schnurr and Johannes Windschuh. Working together they helped me in the completion of this research work. Talking with them I learned a lot of interesting things about customs and habits of german people.
- I am truly indebted and thankful to Mr. Stadler, Physikalisches Institut of the University of Heidelberg, for his cooperation and for the production of the several pumping cells used for this work... a "glass artist".
- I am obliged to many of my colleagues for providing a stimulating and fun environment in which to learn and grow. I am especially grateful to Benjamin Schmitt, Christian Matthies, Moritz Zaiß, Takako Kurimoto, Olga Ivchenko, Tobias Rentrop, Eugenia Rerich, Barbara Witulla, Andreas Korzowski, Volkert Roeloffs, Steffen Görke, Nicolas Behl and Christian David.

- The DKFZ and the International Max Planck Research School for quantum dynamics in physics, chemistry, and biology, for funding my fellowship and expenses associated with it.
- Un ringraziamento particolare ai miei più cari amici, Piero e Filippo, che nonostante la lontananza mi hanno sostenuto e confortato. Grazie di cuore! Le nostre lunghe chiacchierate hanno alleviato quel senso di solitudine e sconforto che alle volte, soprattutto nei primi anni, mi assaliva. Senza il vostro supporto, probabilmente, non sarei riuscito ad affrontare e completare questo ciclo di studio all' estero.
- E per ultimi, ma non meno importanti, un ringraziamento affettuoso a tutti i miei familiari. A Giorgia, che pure a chilometri di distanza, è riuscita a trasferirmi un po della sua forza e determinazione. Ai miei carissimi zii: Catia e Vittorio, Patrizia e Nicola, Mimma e Dino. Ai miei cuginetti: Valerio, Gianmarco e Claudia. Perché l' amore, l' unione ed il senso di appartenenza ad una famiglia come la nostra va oltre ogni distanza. E nonostante non facciate più parte della mia quotidianità, siete sempre nel mio cuore. Devo ringraziare tutti voi per essere diventato l' uomo che sono.